

Discrimination of individual Iron-bearing minerals with the Sentinel-2 Super-Spectral Imager

NAZIF UMAR

August, 2023

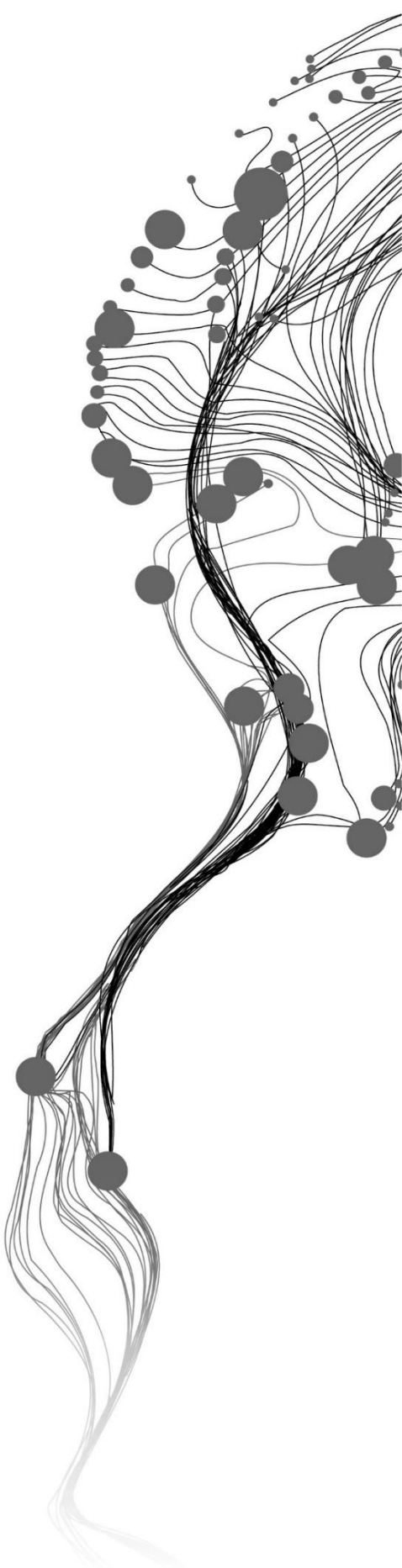
SUPERVISORS:

Dr. H. M. A van der Werff

Dr. A. Dijkstra

Advisor:

B. V. Portela



Discrimination of individual Iron-bearing minerals with the Sentinel-2 Super-Spectral Imager

NAZIF UMAR

Enschede, The Netherlands, August, 2023

Thesis submitted to the Faculty of Geo-Information Science and Earth Observation of the University of Twente in partial fulfillment of the requirements for the degree of Master of Science in Geo-Information Science and Earth Observation.

Specialization: Applied Remote Sensing

SUPERVISORS:

Dr. H. M. A van der Werff

Dr. A. Dijkstra

THESIS ASSESSMENT BOARD

Prof. dr. M. van der Meijde (Chair)

Dr. R.D Hewson (External Examiner)

DISCLAIMER

This document describes the work undertaken as part of a program of study at the Faculty of Geo-Information Science and Earth Observation of the University of Twente. All the views and opinions expressed therein remain the sole responsibility of the author and do not necessarily represent those of the faculty.

ABSTRACT

Iron-bearing minerals such as jarosite, goethite and hematite act as proxies, indicating the presence of underlying mineralization with high economic potential, especially in areas where valuable ore deposits may be concealed beneath the sediments. Consequently, mapping of these minerals using multispectral satellite imagery has been a subject of research for several decades. Geological Remote Sensing techniques, such as band ratio, are valuable in iron mineral mapping because they effectively emphasize the spectral signatures of specific minerals. Iron minerals exhibit distinct absorption features in the VNIR spectral range, making it crucial to have a multispectral sensor with high spectral resolution at the VNIR to identify and discriminate them.

Sentinel-2, a high resolution satellite sensor, with multiple narrow bands at the VNIR compared to the fewer bands of ASTER and Landsat 8 at the VNIR is employed for this study. Twenty-nine high-resolution spectra collected from the created synthetic minerals were resampled to Sentinel-2 resolution. Existing band ratios were tested to evaluate whether they discriminate between iron minerals or not. Subsequently, the shortcomings of the existing band ratios led to the development of novel band ratios.

Iron-bearing mineral distribution in a real-world setting was explored using novel band ratios. The distributions of hematite and goethite were determined using band ratios $(B4/B3)$ and $(B3/B2)$, respectively, with significant matching to a published hyperspectral map. However, discrepancies become evident in discriminating jarosite using the $(B5+B11)/B12$ ratio, potentially due to overwhelming absorption features from other minerals. The combination of the band ratios into a composite enhanced the discrimination.

The findings show the success of the proposed band ratios in identifying hematite and goethite minerals and highlights the significance of integrating band ratios as composite in mineral discrimination. In addition, this research has successfully produced high-quality spectra of iron minerals thereby adding to the existing spectral libraries, and can be used as reference for future studies. Finally, this study highlights the challenges related to interaction of iron minerals with minerals in real world, making discrimination difficult.

ACKNOWLEDGEMENTS

I begin by expressing my gratitude to God Almighty, for blessing me with health and motivation throughout this journey.

I am deeply grateful to my supervisors, Dr. H. M. A van der Werff and Dr. A. Dijkstra, for their unwavering support, constructive feedback, and invaluable guidance. They provided crucial recommendations that helped to shape this research.

I would like to thank B.V. Portela for his constructive feedback and guidance.

Special thanks goes to the DG NGS, Dr. Abdulrazaq A. Garba and dir. Mr Umar Bature for their support and understanding.

To my family, your unwavering faith in me and constant encouragement have been the courage of my journey. Your love and support kept me going, and this accomplishment is as much yours as it is mine.

I also wish to extend my gratitude to my classmates and to my friends; Wildan, Ahmed, and many others who have celebrated me, and provided support during challenging times.

To Ms. Dorothy, and Hassan thank you for the support and guidance. And to Stephen, thank you for all the comments and feedback.

Finally, I am grateful to the Netherlands Fellowship Programme for the scholarship to study in ITC Faculty at University of Twente.

TABLE OF CONTENTS

INTRODUCTION.....	1
1.1 Background	1
1.2 Previous Work	4
1.3 Statement of the problem	6
1.4 Objectives	7
2 DATA AND METHODOLOGY	8
2.1 Data.....	8
2.1.1 Materials for the Synthesis.....	8
2.2 Methods	9
2.2.1 Analysis of the USGS Spectral Library.....	9
2.2.2 Synthesis and Analytical Techniques	9
2.2.3 Characterization of the products (synthetic minerals)	11
2.2.4 Building spectral libraries.....	12
2.2.5 Band Ratio.....	13
3 RESULTS	17
3.1 Laboratory Experiment and Characterisation	17
3.1.1 Characterisation of the products	18
3.2 Spectroscopic analysis.....	20
3.2.1 Spectral Analysis of the synthetic minerals.....	20
3.2.2 Comparison with the USGS Spectral Library	21
3.2.3 Spectral Analysis of the Synthetic Iron minerals	25
3.3 Band Ratios	27
3.3.1 Multispectral Sensor Resampling and Comparison.....	27
3.3.2 Assessments of the Existing band ratios.....	28
3.4 Experimenting with new band ratios.....	39
3.5 Evaluating the Novel Band Ratios	45
3.5.1 Single-band Gray Image.....	45
3.5.2 False Color Composite (RGB) map.....	49
4 DISCUSSION	53
4.1 Spectral Features of Iron Minerals	53
4.1.1 Pure Iron Minerals and Mixtures.....	54
4.1.2 Influence of mixtures on iron mineral spectral features	55
4.2 Multispectral Analysis	56
4.2.1 Existing band ratio analysis	56
4.2.2 Novel band ratios experiment.....	56
4.2.3 Comparison of Sentinel-2 and Hyperspectral Output.....	58
5 CONCLUSION.....	60
5.1 Research questions	62
5.3 Recommendations.....	63

References.....	64
Appendices.....	67

LIST OF FIGURES

Figure 1 This Figure demonstrates the essential spectral distinctions between iron-bearing minerals, presenting the band positions of the relevant multispectral sensors (from this study).....	1
Figure 2 True and relative absorption band depth concept (modified after Crowley et al., 1989).....	13
Figure 3a Mineral map utilizing the 400 to 1300 nm electronic absorption band of the AVIRIS data, showing the spectrally dominant Iron-bearing minerals at Cuprite.	16
Figure 3b Mineral map of the 1300 to 2500 nm vibrational absorption wavelength region of the AVIRIS data, showing the spectrally dominant clays, micas, sulfates, and carbonates at Cuprite.....	16
Figure 4a Synthetic XRD pattern shows distinct peaks, with the most intense peak often observed around 17 and 29 degrees 2-theta and other smaller peaks at different angles.	18
Figure 4b Goethite XRD profile shows a strong diffraction peak around 21 and 37 degrees 2-theta and other smaller peaks at different angles.	19
Figure 4c Hematite XRD pattern characterized by several peaks. The most intense peak is usually observed around 33 and 36 degrees 2-theta, and other smaller peaks at different angles.	19
Figure 5 High-resolution reflectance spectra of iron minerals exhibiting distinct VNIR absorptions caused by crystal field and charge transfer processes (from this study).....	20
Figure 6 Powdered products of synthetic iron-bearing minerals (from current study).....	21
Figure 7a Mineral spectra from the USGS Spectral Library (Kokaly et al., 2017) against synthetic jarosite spectra (from the current study).....	23
Figure 7b Mineral spectra from the USGS Spectral Library (Kokaly et al., 2017) against synthetic hematite spectra (from the current study).....	23
Figure 7c Mineral spectra from the USGS Spectral Library (Kokaly et al., 2017) against synthetic hematite spectra (from the current study).....	24
Figure 8a Spectra of pure goethite, jarosite, and their mixtures. Each mixture exhibits combined characteristics.	25
Figure 8b Spectra of pure hematite and its mixture with calcite against spectra of calcite from the USGS spectral library. b). Picture showing different shades of hematite in varied concentrations.	26
Figure 9 Resampled spectra of jarosite, goethite, and hematite to ASTER, OLI, and Sentinel-2. Graphs are offset.	27
Figure 10a Resampled spectra of the minerals and the corresponding band's position denoted by small circles that were used in the ratio (B_{11}/B_8) against (B_4/B_3)	28
Figure 10b Scatterplots of (B_{11}/B_8) vs. (B_4/B_3) for the pure iron minerals with the supported triangular trend illustrating the relationship between pure iron minerals.	29
Figure 10c Supported triangular trend illustrates the relationship between iron minerals and their varying compositions.	29
Figure 10d Iron minerals mixtures with quartz show hematite assigned high scores, jarosite intermediate scores, and goethite low scores by B_4/B_3 . Goethite is assigned an indistinct score by B_{11}/B_8 , some scores of goethite overlap with both jarosite and h.	30
Figure 10e Depicts a linear relationship between hematite and jarosite by B_4/B_3 , with both ratios assigning distinct values to each; however, goethite appears to have indistinct scores by B_{11}/B_8	30
Figure 10f Scatterplots of (B_{11}/B_8) vs. (B_4/B_3) show iron minerals assigned distinct scores, with hematite mineral mixtures receiving a high score from both ratios, while goethite mixtures gaining an intermediate score from B_{11}/B_8 and a low score from B_4/B_3	31
Figure 11a Resampled spectra of the minerals and the corresponding band's position denoted by small circles that were used in the ratio $(B_4/B_2) \times (B_4+B_{11})/B_8$ against (B_4/B_3)	32
Figure 11b Scatterplot shows no preferred trend by the points of iron minerals composition.....	33
Figure 11c Scatterplot show iron minerals assigned indistinct scores by $(B_4/B_2) \times (B_4+B_{11})/B_8$, while (B_4/B_3) assigned distinct scores to the minerals.....	33
Figure 11d Scatterplot shows the iron minerals are assigned indistinct scores by $(B_4/B_2) \times (B_4+B_{11})/B_8$, whereas the (B_4/B_3) ratio assigned distinct scores to the minerals.	34
Figure 11e Scatterplots of $(B_4/B_2) \times (B_4+B_{11})/B_8$ vs (B_4/B_3) for the iron minerals show a nonlinear relationship, and the supported triangle trend does not work between the mixtures of iron minerals.	34
Figure 12a The resampled spectra of the minerals and the corresponding band's position, denoted by small circles, that were used in the ratio $(B_4/B_2) \times (B_4+B_{11})/B_8$ vs $(B_{12}/B_8) + (B_3/B_4)$	35

Figure 12b Scatterplot shows a linear trend by the points of pure iron minerals assigning each mineral a distinct score.....	36
Figure 12c Scatterplot show iron minerals assigned indistinct scores by $(B4/B2) \times (B4+B11)/B8$ vs $(B12/B8)+(B3/B4)$, no supported triangle trend for mineral composition.	36
Figure 12d Scatterplot shows the iron minerals are assigned indistinct scores by $(B4/B2) \times (B4+B11)/B8$ vs $(B12/B8)+(B3/B4)$. Trend follows composition, but the ratios assigned indistinct scores.	37
Figure 12e Scatterplots of $(B4/B2) \times (B4+B11)/B8$ vs. $(B12/B8)+(B3/B4)$ show a linear relationship, and the supported triangle trend does not work between the mixtures of iron minerals.	37
Figure 12f Scatterplots of all iron minerals with mixtures are assigned indistinct scores by $(B4/B2) \times (B4+B11)/B8$ vs $(B12/B8)+(B3/B4)$	38
Figure 13a The resampled spectra of the minerals and the corresponding band's position, denoted by small circles, that were used in the ratio $(B4/B2) \times (B4+B11)/B8$ vs $(B12/B8)+(B3/B4)$	40
Figure 13b Band ratios show a linear trend and correlation, uniquely scoring each pure iron mineral.....	41
Figure 35Figure 13c shows band ratios are correlated, assigning distinct scores to varied mineral compositions.	41
Figure 14a Resampled spectra of the minerals and the corresponding band's position denoted by small circles that were used in the ratio $(B3/B4)+(B7/B9)$ vs $(B5+B11)/B12$	42
Figure 14b Scatterplot shows a nonlinear trend with plots positioned in a triangular trend. Each mineral is assigned distinct scores.	43
Figure 14c Scatterplot shows iron minerals mixtures assigned indistinct scores by $(B3/B4) \times (B7/B9)$ vs $(B5+B11)/B12$, depicting a supported triangle trend for varied mineral composition.....	43
Figure 14d Scatterplot shows the iron minerals assigned distinct scores by $(B3/B4) \times (B7/B9)$ vs $(B5+B11)/B12$. The triangular trend depicts varied composition; however, the points move towards the center.....	44
Figure 15a Single-band gray image generated by the band ratio $(B4/B3)$ is shown here, with the highest value indicating the hematite distribution. Notably, hematite is highlighted in the central part of the map and to the east. 15b Mineral map utilizing t	46
Figure 16a. Single-band gray image generated by the band ratio $(B3/B2)$ highlighted mixtures of iron minerals distribution; however, the ratio discriminates goethite in the laboratory, predominantly in the southwest part of the image and some central part	47
Figure 17a Single-band gray image generated by the band ratio $(B5+B11)/B12$ highlights alteration zones, particularly in the west and east of the image. Alunite has the brightest pixels than kaolinite. 17b Mineral map of the 1300 to 2500 nm vibrational ab.....	48
Figure 18 RGB false color composite map generated by combining three band ratios $(B4/B3)$, $(B3/B2)$, and $(B5+B11)/B12$ shows the distribution of the iron-bearing minerals in the area. RGB: Red color denotes Hematite, Green is a mixture of iron minerals with.....	49
Figure 19a RGB false color composite map generated by combining three band ratios $(B4/B3)$, $(B3/B2)$, and $(B5+B11)/B12$ shows the distribution of the iron-bearing minerals in the area. RGB: The Red color denotes Hematite, Green is a mixture of iron minerals	50
Figure 20a. Single-band gray image generated by the band ratio $(B3/B4)+(B7/B9)$ highlighted mixtures of Goethite with other iron minerals distribution; the ratio discriminates goethite in the laboratory. Here it show it did not show clear distribution. Fi.....	51
Figure 21 RGB false color composite map generated by combining three band ratios $(B4/B3)$, $(B3/B4)+(B7/B9)$, and $(B5+B11)/B12$ shows the distribution of the iron-bearing minerals in the area. RGB: Red color denotes Hematite, Green is from $(B3/B4)+(B7/B9)$ an.....	52

LIST OF TABLES

Table 1 An overview of Sentinel-2 bands according to Copernicus-derived user requirements (modified after Drusch et al., 2012).Table 2.	2
Table 2 An overview of secondary iron-bearing mineral occurrence and distribution (modified after Bigham et al., 2018; Cogram, 2018; Schwertmann, 1958).....	4
Table 3 Existing band ratios from the literature, and the band numbers, as indicated in the table, are specific to each sensor (modified after Cudahy & Ramanaidou, 1997; Kalinowski & Oliver, 2004; Rockwell, 2013; van der Meer et al., 2014; van der Werff & van der Meer, 2016).....	7
Table 4 Chemical substances used for the synthesis.....	8
Table 5 The various spectrometers utilized in the USGS spectral library to measure spectrum (modified after Kokaly et al., 2017).....	9
Table 6 Samples description and identification	17
Table 7 Observed wavelength positions of absorption characteristics in iron-bearing minerals (findings from the current study).....	20
Table 8 Summary of USGS Spectra metadata of the iron minerals (modified after Kokaly et al., 2017). .	22
Table 9 Summary of the findings from the analysis of band ratios for discriminating between the iron minerals.	38
Table 10 Displays relationships between bands and spectral features of iron-bearing minerals.	39
Table 11 Summary of novel band ratios performances on discriminating the iron-bearing minerals	40

ABBREVIATIONS

ASD	-	Analytical Spectral Device
ASTER	-	Advanced Spaceborne Thermal Emission and Reflection Radiometer
EC	-	European Commission
ESA	-	European Space Agency
Gth	-	Goethite
GRS	-	Geological Remote Sensing
Hm	-	Hematite
Jsk	-	Jarosite
RS	-	Remote Sensing
TM	-	Thematic Mapper
MSS	-	Multispectral Scanner
FTIR	-	Fourier Transform Infra-Red
OLI	-	Operational Land Imager
S2	-	Sentinel-2
SSI	-	Super-spectral Imager
SWIR	-	Shortwave Infrared
USGS	-	United States Geological Survey
VNIR	-	Visible and Near-Infrared
XRD	-	X-ray Diffraction
VRE	-	Vegetation Red Edge
JSCPD	-	Joint Committee on Powder Diffraction Standards

Definitions

Iron-bearing minerals: refers to individual minerals bearing ferric or ferrous iron like Hematite, Goethite, Jarosite (also iron minerals)

Iron mineral groups: particularly of Fe⁺² and Fe⁺³ groups

INTRODUCTION

1.1 Background

Iron is one of the most abundant elements in Earth's crust, accounting for approximately 5.1% of its composition by weight. It is widely distributed and forms various rock-forming minerals, including iron oxides, sulfides, and silicates. Therefore, naturally occurring compounds that contain iron as their primary component are referred to as Iron-bearing minerals in this study. These minerals contribute to diverse rocks in the Earth's crust, including basalt, granite, gneiss, shale, and sandstone (Bigham et al., 2018). Furthermore, Iron-bearing minerals are strongly attracted to various metals, effectively capturing and retaining them within the soil matrix. This phenomenon plays a crucial role in the scavenging and concentration of ore-forming metals released during weathering processes and in the sequestration of potentially harmful elements in soils and sediments (Edwards & Atkinson, 1986). Consequently, their high affinity for metal binding is essential in geochemical processes and environmental studies because it influences the distribution and availability of metals in the Earth's crust and affects soil fertility and environmental quality (Bullock et al., 2021). In addition, studies have shown that surface iron-bearing minerals act as proxies, indicating the presence of underlying mineralization with high economic potential, especially in areas where valuable ore deposits may be concealed beneath barren sediments (Bigham et al., 2018; Butt & Zeegers 1992; Cogram, 2018). Moreover, the studies also demonstrate that each Iron-bearing mineral is associated with a specific chemical, geological and environmental process, all of which bear significant implications. Consequently, the identification and discrimination of these minerals have become crucial.

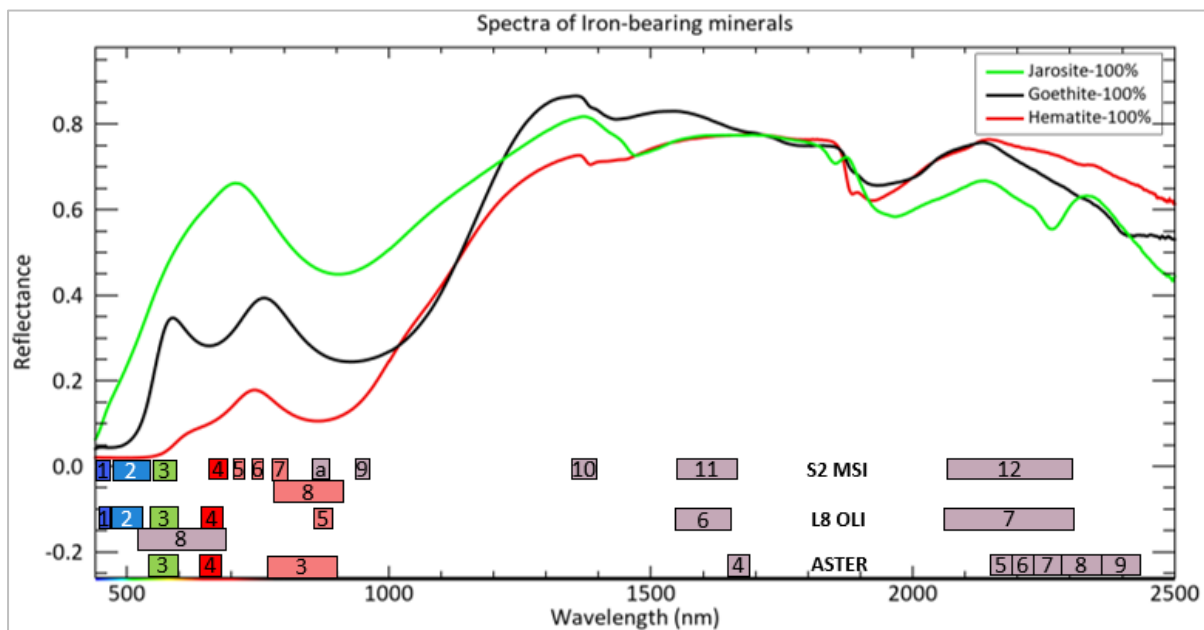


Figure 1 This Figure demonstrates the essential spectral distinctions between iron-bearing minerals, presenting the band positions of the relevant multispectral sensors (from this study).

However, conducting this activity in the field using rock sampling can be tedious and time-consuming and cannot be performed in extensive and inaccessible areas. Therefore, geological remote sensing (GRS) can offer fast tools for identifying these minerals, primarily using satellite sensors like the Sentinel-2 (Table 1) with high spectral resolution in the electromagnetic spectrum's visible near-infrared (VNIR) wavelength range. The GRS is based on the spectral analysis of minerals and rocks (Cooper et al., 2002; Cudahy & Ramanaidou, 1997; Hewson et al., 2001; Hunt, 2012; Kokaly et al., 2017; Salisbury et al., 1989; Swayze et

Discrimination of individual Iron-bearing minerals with the Sentinel-2 Super-Spectral Imager

al., 2014). GRS techniques, such as band ratio, are valuable in mineral mapping because they effectively emphasize the spectral signatures of specific minerals and minimize topography's influence. This technique enhances the detection of narrow variation in the spectral reflectance characteristics of rocks and minerals. Furthermore, this technique involves dividing the values of one spectral band by another and calculating the spectral reflectance ratio between the two bands (Crowley et al., 1989), thereby highlighting the spectral differences between specific minerals in the scene. For instance, iron-bearing minerals possess characteristic spectral absorption features at particular wavelength positions (Clark et al., 1993; Cudahy & Ramanaidou, 1997; Hunt, 2012; Kokaly et al., 2017; van der Meer et al., 2012). By performing band ratio on satellite data, researchers can create ratio images that enhance the contrast of these absorption features, aiding the mapping and identification of iron-bearing minerals in various geological formations. Several band ratios have been proposed for mapping iron mineral groups, as shown in Table 1. The band ratio approach has acquired recognition and has been applied in various studies, including those conducted by Goetz & Rowan (1981), Kalinowski & Oliver (2004), Rowan et al. (2003), and van der Meer et al. (2012).

Table 1 An overview of Sentinel-2 bands according to Copernicus-derived user requirements (modified after Drusch et al., 2012).

Band	Band ID	Band Name	Band center (nm)	FMWH (nm)	Spectral resolution (nm)	Spatial resolution (m)	Radiometric resolution (bits)
1	B1	Coastal Aerosol	443	442.5	20	60	12
2	B2	Blue	490	492.7	66	10	
3	B3	Green	560	559.2	36		
4	B4	Red	665	664.3	31		
5	B5	VRE	705	703.5	15	20	
6	B6	VRE	740	740.1	15		
7	B7	VRE	783	781.8	20	10	
8	B8	NIR	842	828.9	106	20	
8A	B8A	NIR	865	864.3	21	20	
9	B9	Water Vapor	945	944.5	20	60	
10	B10	Cirrus	1375	1372.9	31	20	
11	B11	SWIR	1610	1613.3	91		
12	B12	SWIR	2190	2202.9	175		

Spectral libraries like the USGS spectral library (Clark et al., 1993; Kokaly et al., 2017) are critical for hyperspectral and multispectral remote sensing analysis, containing spectroscopic measurements of field and laboratory samples (Zhou et al., 2017). These libraries offer an abundance of spectral data beneficial for remote sensing analysis; however, their practical application presents certain limitations.

One of these limitations is encountered when discriminating between related minerals because the spectra in these libraries are gathered from a wide array of sources, as observed in the metadata (Kokaly et al., 2017). These minerals often coexist with other minerals and impurities in varying proportions and compositions. However, The USGS library does not have comprehensive descriptions for all its samples, as indicated in the metadata (Kokaly et al., 2017). This limitation can impact the accuracy of information derived from a spectrum's composition. Therefore, the spectrum of hematite, for instance, could originate from a sample having a different set of impurities than those in goethite or jarosite. This heterogeneous nature of the spectral data introduces a level of variability that might affect the accuracy of mineral identification.

Furthermore, it is essential to note that different spectrometers were used to collect spectra in the USGS spectral library, and this may introduce variations when comparing the spectra of different minerals (Kokaly

et al., 2017). This is due to the inherent properties of the spectrometer, which include its sensitivity, resolution, and accuracy, among other technical specifications. The spectrometer essentially measures the light absorbed, reflected, or emitted across a certain range of wavelengths from a material (Dahm & Dahm, 2020). Therefore, different spectrometers, with varying levels of sensitivity and resolution, can yield slightly different spectral measurements for the same material. For example, if the spectrometer used in the USGS library has a higher resolution, it could detect minor features in the spectrum that a less sensitive instrument might miss. This could lead to perceived differences when comparing spectra. Similarly, the accuracy of the spectrometer in the detection and quantification of spectral features can impact the comparison results. In essence, the spectrometer's features and specifications can impact the comparison of spectra, potentially leading to discrepancies when interpreting the data.

Consequently, the complexity of this variability suggests a need for synthetic minerals in controlled, laboratory-based studies with known proportions, composition, and the same spectrometer. Such studies could analyze the impact of specific impurities on the spectral characteristics of each iron mineral in a controlled setting. This would highlight the impurities' effect on the minerals' spectral signatures and enhance the precision of mineral identification. However, it's important to note that using standardized, laboratory-based spectral libraries isn't without implications. One significant implication is the risk of incorrect identification (Zhou et al., 2017). Therefore, while standardized spectral libraries offer convenience, they present certain challenges, especially in mineral mapping, that need to be carefully considered.

Three iron-bearing minerals (jarosite, goethite, and hematite) were chosen for this research. Jarosite with a chemical formula of $\text{KFe}_3(\text{SO}_4)_2(\text{OH})_6$, known for its characteristic yellow-to-brownish-yellow color, also known as an iron-hydroxy sulfate mineral, and goethite with a chemical formula of $\text{FeO}(\text{OH})$, and a yellowish-brown color, and it is most thermodynamically stable. While, hematite with a chemical formula Fe_2O_3 , and a distinct color of reddish-brown to black appearance, it is a common iron-bearing mineral found in soils, sediments, and rocks known for its high thermodynamic stability (Bigham et al., 2018). The choice of jarosite, goethite, and hematite for the focus of this study was based on their abundance and distribution (Bigham et al., 2018; Schwertmann, 1958), their distinct spectral signatures (Cudahy & Ramanaidou, 1997), their coexistence, and their significance in both geology and environmental science (Cogram, 2018). The occurrence and distribution of the iron minerals are presented in Table 2.

Firstly, these minerals are very common, making them important for understanding the geology and geochemistry of the Earth's crust. Iron is one of the most abundant elements on Earth, and these three minerals are widespread iron-bearing minerals (Bigham et al., 2018; Schwertmann, 1958). Their abundance means that they play key roles in various geological and geochemical processes. Secondly, each of these minerals has a distinct spectral signature, which makes them particularly suitable for study using remote sensing techniques. The unique spectral features of these minerals make them identifiable and distinguishable in the data collected, thus enabling important conclusions about the geology and mineralogy of the areas under study to be drawn. Thirdly, these minerals are associated with specific chemical, geological, and environmental processes, each having its unique implications. For instance, jarosite is commonly found in oxidized zones of sulfide ore deposits, and it is associated with acidic, sulfate-rich environments, which are often the result of human activities like mining, serving as repositories for potentially hazardous elements (Cogram, 2018). On the other hand, goethite is the most stable iron oxide in ambient conditions and often forms as a result of the weathering of other, less stable iron minerals. Similarly, hematite is known for its stability and is an important mineral in banded iron formations, which are a significant source of iron ore (Bigham et al., 2018). In addition, jarosite has also been found on the surface of Mars (Farrand et al., 2009), which is a very oxidizing environment. The presence of jarosite on

Discrimination of individual Iron-bearing minerals with the Sentinel-2 Super-Spectral Imager

Mars suggests that there was once liquid water on the planet, as jarosite formation requires both water and oxidizing conditions.

Table 2 An overview of secondary iron-bearing mineral occurrence and distribution (modified after Bigham et al., 2018; Cogram, 2018; Schwertmann, 1958).

Iron minerals	Color	Environment of formation	Distribution
Jarosite $\text{KFe}_3(\text{SO}_4)_2(\text{OH})_6$	yellow-to-brownish-yellow	Highly oxidized and acidic environment (Acid mine drainage; Mars)	Localized, small-scale (also found on Martian surfaces)
Goethite $(\text{FeO}(\text{OH}))$	yellowish-brown	Low-temperature; Weathering environments (oxidizing): cool, moist conditions that involve higher terrain and rich biological material	Global (entire planet) to Continental (geographic region) to Landscape (particular area) to Stratigraphic (specific rock formation or layer)
Hematite (Fe_2O_3)	reddish-brown to black	Higher-temperature; Aerobic soil: prevalent in tropical, subtropical, dry, semi-arid, and Mediterranean regions, with higher concentrations and lower levels of organic matter content.	Continental to Landscape to Stratigraphic

Finally, the relevance of these minerals in exploration studies, particularly in relation to valuable ore deposits, made them an interesting choice. These minerals can act as proxies indicating the presence of underlying mineralization with high economic potential, especially in areas where valuable ore deposits may be concealed beneath barren sediments like the Cuprite area, Nevada, US (Swayze et al., 2014). Moreover, Kosk (2010) observed a significant occurrence of hematite, goethite, and jarosite in the supergene setting. They proposed that the process of mapping gossans in gold deposits can serve as proxies for exploration. Moreover, Swayze et al. (2014) proposed that the detection of fine-grained jarosite at specific locations in the Cuprite area, through electronic absorption, indicates the active oxidation of sulfide minerals near the surface. Therefore, by focusing on jarosite, goethite, and hematite, this study seeks to add to the previous work on mapping iron minerals with remote sensing data by employing Sentinel-2 sensors to discriminate between these minerals, thereby contributing to the development of more effective mineral exploration.

1.2 Previous Work

Iron-bearing mineral mapping using multispectral satellite imagery has been a subject of research for several decades (Crowley et al., 1989; Goetz and Rowan, 1981; van der Meer et al., 2014). However, Iron-bearing minerals exhibit distinct absorption features in the VNIR spectral range, making it crucial to have a high spectral resolution to identify and map mineral species accurately. Therefore, the development and utilization of satellite-based remote-sensing techniques for iron mineral mapping have evolved with advances in satellite technology. The advent of early satellite sensors, notably the Landsat series introduced in the 1970s, comprising Landsat 5 and 7, marked a significant milestone in geological remote sensing. These pioneering multispectral imaging instruments have opened new avenues for researchers to explore the potential of mapping iron minerals. By capturing data across multiple spectral bands, these satellites have facilitated initial investigations into identifying and characterizing iron-bearing minerals on the Earth's surface.

In 1981, the seminal work of Goetz & Rowan (1981) marked a groundbreaking milestone in geological remote sensing, particularly in iron mineral mapping. By leveraging the capabilities of Landsat Multispectral

Discrimination of individual Iron-bearing minerals with the Sentinel-2 Super-Spectral Imager

Scanner (MSS) satellites, they generated the first-ever maps of distinct iron mineral groups, including ferric iron oxides, ferrous iron oxides, and iron sulfates. This pioneering research demonstrated the feasibility of utilizing early satellite sensors to discriminate between groups of iron minerals and set the stage for subsequent advancements in the field.

Consequently, researchers have turned their attention to Landsat Thematic Mapper (TM), which offers a relatively improved spectral resolution compared to its predecessors. This advancement has allowed for more accurate and quantitative determination of iron content (Andrews Deller, 2006). Subsequently, TM has been used in several geological investigations (Sabins, 1999; Schetselaar et al., 2008; van der Meer et al., 2012). Notably, it has been employed to distinguish between ferric and ferrous oxide groups (using the band ratio B3/B1) and argillic and non-argillic materials (using the band ratio B5/B7) (Abrams, 2000; Abrams & Hook, 1995; Yamaguchi et al., 1998).

However, despite this progress, the spectral resolution of Landsat TM remains limited, preventing a clear distinction of various absorption features. Consequently, the full potential of detailed iron mineral identification and mapping is still limited. Despite its limitations, Landsat TM has paved the way for further research and acts as a stepping stone towards developing more advanced sensors capable of resolving finer spectral features for comprehensive geological remote sensing analyses.

As satellite sensor technology advanced and new cutting-edge sensors, such as the Advanced Spaceborne Thermal Emission and Reflection Radiometer (ASTER), were deployed, researchers were granted access to unprecedented high-resolution multispectral data. ASTER is an Earth-observing instrument launched onboard the National Aeronautics and Space Administration's (NASA) Terra satellite in December 1999. This sensor offers a notable improvement in spatial and spectral resolution, especially in the shortwave infrared (SWIR) bands, surpassing the capabilities of earlier sensors (Figure 1), as highlighted in the studies by Hewson et al. (2001) and Mars & Rowan (2010). It has a high spatial resolution, with VNIR and SWIR sensors providing a 15-meter pixel size and a TIR sensor with a 90-meter pixel size.

Consequently, these technological breakthroughs present a transformative opportunity for the geological remote-sensing community, particularly in mineral mapping, effectively utilizing various ASTER band ratios to create comprehensive maps of surface mineral distributions, further refining our understanding of geological remote sensing applications. Despite the numerous advantages of ASTER, one significant constraint lies in the low spectral resolution of VNIR, which restricts its capability to accurately map iron minerals with diagnostic features predominantly present in the VNIR wavelength range of the electromagnetic spectrum.

Furthermore, the launch of Landsat 8 Operational Land Imaging (OLI) in February 2013 marked a significant milestone in GRS. Developed and launched by NASA as part of the Landsat program, OLI's improved capabilities, equipped with a high spectral resolution in the VNIR wavelength range of the electromagnetic spectrum, made it valuable for upgrading iron minerals map. Consequently, researchers have utilized OLI for iron mineral mapping, as demonstrated in the studies conducted by Ducart et al. (2016) and van der Werff & van der Meer (2016). However, as demonstrated (Figure 1), the spectral bands of these sensors were not finely tuned enough to resolve the narrow spectral variation between the individual iron-bearing minerals; jarosite, goethite, and hematite.

Subsequently, the continuous advancement of satellite sensor technology presents researchers with exciting opportunities with the launch of the Sentinel-2 Super Spectral Imager (SSI). Its enhanced spectral and spatial capabilities and frequent revisit times have captured the attention of researchers exploring its potential for geological studies. Sentinel-2 is part of the Copernicus project, a joint effort between the European Space Agency (ESA) and European Commission (EC). The ESA created a set of next-generation Earth observation missions for the Global Monitoring for the Environment and Security Program.

Discrimination of individual Iron-bearing minerals with the Sentinel-2 Super-Spectral Imager

Sentinel-2 was deployed with two satellites in 2015 and 2017, with a short revisit time at the equator (every five days) in polar orbit when both satellites fly concurrently. It has a large field of view (290 km). In addition, the sensor is equipped with a high spatial resolution with a 13-band set spanning the VNIR through the SWIR wavelength regions (Table 1) (Drusch et al., 2012). This mission provides data with enhanced spectral, spatial, and temporal resolutions in the VNIR wavelength region compared with Landsat 8 and ASTER and can be used in various GRS applications (van der Meer et al., 2012). However, in this study, bands 1, 9, and 10 were excluded from the analysis considering two primary factors: spatial resolution and design purpose. Specifically, these bands possess low spatial resolution, which could potentially limit the accuracy of the mineral discrimination results. Moreover, the primary functions of these bands are not favorable to the investigation. For instance, Band 1 has been primarily designed to detect aerosol scattering and cloud cover, while Band 9 is mainly used for aerosol retrieval and Band 10 is for cloud detection (Drusch et al., 2012).

Over the years, some researchers have conducted research utilizing the Sentinel-2 in the field of GRS (Mielke et al., 2014; Transon et al., 2018; van der Meer et al., 2014). However, its application in this field remains quite limited. This can be attributed to the fact that the primary mission of the satellite is environmental monitoring, as underlined by van der Meer et al. (2014). Interestingly, these studies have demonstrated the feasibility and potential of using Sentinel-2 for geological investigations, paving the way for further research and application in this field. For example, in a study by Mielke et al. (2014), various contemporary and next-generation satellite sensors were assessed for their efficacy in mapping iron feature depth. By evaluating the strengths and limitations of different satellite sensors, their research employed a complex band-ratio approach, leveraging multiple narrow VNIR bands of Sentinel-2 to assess the depth of the iron-bearing features. The result was the relative depth of the iron feature, which revealed the presence of iron in large amounts and could be accounted for by the ASTER band ratios (Hewson et al., 2001). Their research findings revealed that Sentinel-2 was better equipped and outperformed other multispectral sensors in accurately measuring iron feature depth.

Furthermore, ongoing research on the potential of Sentinel-2 in geological research has led to the emergence of innovative and novel discoveries. For instance, a recent study by van der Werff & van der Meer (2015) focused on exploring the VNIR bands of Sentinel-2, employing three band ratios to map the mineralogy related to a hydrothermal alteration regime, demonstrating the valuable applications of Sentinel-2 data in characterizing hydrothermal mineral assemblages. However, this work continues on that and goes a step further than the existing work by discriminating between different iron minerals. Therefore, this study aims to explore the potential of the relatively narrow VNIR bands of Sentinel-2 as well as the two bands in the SWIR, which cover the specific wavelength range that iron-bearing minerals exhibit diagnostic features. Moreover, it is essential to acknowledge the availability of multispectral sensors, such as SPOT, GeoEye, WorldView, and other high-resolution satellite sensors that offer significant advantages over their predecessors regarding spectral and spatial resolution and specific view geometries. However, these higher-resolution sensors come at a cost, limiting access to researchers and organizations with budget constraints.

1.3 Statement of the problem

Previous research has focused on using the features of wavelength position and depth of maximum absorption at 900 nm to map iron mineral groups (van der Werff & van der Meer, 2015). However, this study expands the scope by considering other diagnostic features observed at wavelength ranges, such as the red, blue, and green wavelengths range. This study goes a step further, from recognizing groups of iron minerals to discriminating individual minerals, thereby addressing the gap.

Discrimination of individual Iron-bearing minerals with the Sentinel-2 Super-Spectral Imager

Table 3 Existing band ratios from the literature, and the band numbers, as indicated in the table, are specific to each sensor (modified after Cudahy & Ramanaidou, 1997; Kalinowski & Oliver, 2004; Rockwell, 2013; van der Meer et al., 2014; van der Werff & van der Meer, 2016).

Sensor	Fe ³⁺ oxides				Fe ²⁺ oxides			
ASTER	B2/B1	-	B4/B3	-	-	B5/B3 + B1/B2		B5/B4
Landsat 5&7	-	B3/B1	B5/B4	$B3/B1 \times (B3+B5)/B4$	-	B7/B4 + B2/B3	$(B2+B5)/(B3+B4)$	-
Landsat 8 OLI	B4/B3	B4/B2	B6/B5	$B4/B2 \times (B4+B6)/B5$	$B4+B6/B5$	B7/B5 + B3/B4	$(B3+B6)/(B4+B5)$	B7/B6
Sentinel- 2	B4/B3	B4/B2	B11/ B8	$B4/B2 \times (B4+B11)/B8$	$(B4+B11)/B8$	B12/B8 + B3/B4	$(B3+B11)/(B4+B8)$	B12/ B11

1.4 Objectives

The primary objective of this study was to discriminate between specific iron-bearing minerals using Sentinel-2's VNIR bands.

Sub-objectives and Research Questions

- 1) To analyze the diagnostic features of pure iron-bearing minerals using spectroscopy to evaluate the applicability of spectral features from the USGS spectral library.
 - a) Do pure samples reconfirm what we know from the USGS library regarding the two mineral groups (Fe⁺² and Fe⁺³)?
 - b) How much can be depended on the USGS spectral library for pure minerals?
- 2) To assess the visibility of diagnostic spectral features of iron-bearing minerals in controlled mixtures related to their naturally occurring forms.
 - a) Can the diagnostic spectral features of iron-bearing minerals be distinguished in mixtures?
 - b) How do the spectral features of pure iron-bearing minerals and their mixtures compare?
- 3) To investigate the existing band ratios proposed for Sentinel-2 and other sensors to identify the specific iron-bearing minerals and mixtures that can be identified using these ratios.
 - a) Can the band ratios suggested for other sensors be used in Sentinel-2?
 - b) Which iron-bearing minerals can be identified using the existing Sentinel-2 band ratio methods?
 - c) Which iron-bearing minerals have not been discriminated against using the existing Sentinel-2 band ratios from the published literature?
- 5) To modify or create new band ratios that can be used to discriminate against specific iron-bearing minerals that cannot be achieved using existing band ratios.
 - a) Which iron-bearing minerals have not been discriminated against using the existing Sentinel-2 band ratios from the published literature?
- 6) To evaluate whether the Sentinel-2 band ratios can identify specific iron-bearing minerals by comparing them to the hyperspectral analysis of Cuprite, Nevada.
 - a) Which iron-bearing minerals are discriminated against using high-resolution methods, such as hyperspectral data, and which ones were found with multispectral data?
 - b) How does Sentinel-2's output compare to the hyperspectral output that has been published?

2 DATA AND METHODOLOGY

2.1 Data

This section provides a description of the datasets and methods that were used in this study. The first set of data used was the USGS Spectral Library; Then the second was chemical substances (acid, base, etc.), solutions, and reagents (Table 4). In addition, sterilizing agents were also used in cleaning, such as Nitric acid, Hydrogen peroxide, Ethanol, and Ultra-pure water (de-ionized). These were used in the preparation and synthesis of about 29 samples of pure iron-bearing minerals (Jarosite, Goethite, and Hematite) and their respective mixtures (e.g., with Calcite and Quartz). The mixtures were carried out in such a way that it reflects a natural concentration in varying proportions, as shown in Table 6. The Geoscience Laboratory at ITC, University of Twente, was used for all the laboratory work, from sample preparation to analysis.

2.1.1 Materials for the Synthesis

Furthermore, Hyperspectral data of the synthetic minerals and the USGS Spectral Library were used to analyze the diagnostic features of the iron-bearing mineral, whereas Multispectral data of the Sentinel-2 imagery was employed for band ratio and validation.

Table 4 Chemical substances used for the synthesis

	Name of chemical	Chemical formula	Quantity used	Provider
1	Ferric nitrate	$\text{Fe}(\text{NO}_3)_3 \cdot 9\text{H}_2\text{O}$	50 g	Merck KGaA
2	Ferric chloride	$\text{FeCl}_3 \cdot 6\text{H}_2\text{O}$	50 g	Merck KGaA
3	Ammonia	NH_3 (liquid)	-	Merck KGaA
4	Ferric sulfate hydrate	$(\text{Fe}_2(\text{SO}_4)_3 \cdot n\text{H}_2\text{O})$	-	Sigma Aldrich
5	Sodium hydroxide	NaOH	-	Sigma Aldrich
6	Potassium hydroxide	KOH	-	J.T. Baker Chemicals B.V.
7	Ammonium hydroxide	NH_4OH	-	J.T. Baker Chemicals B.V.
8	Calcite	CaCO_3	3.75 g	Boom B.V. Meppel
9	Quartz	SiO_2	3.75 g	Boom B.V. Meppel
10	Nitric acid	HNO_3	-	J.T. Baker Chemicals B.V.
11	Hydrogen peroxide	H_2O_2	-	J.T. Baker Chemicals B.V.
12	Ethanol	$\text{C}_2\text{H}_6\text{O}$	50 mL	-
13	Ultra-pure water (de-ionized)	H_2O	500 mL	-

2.2 Methods

In this section, the methodology employed to achieve the experiments and analysis is discussed. The first part discusses the analysis of the USGS Spectral Library, followed by the synthesis of the minerals in the second part. The third part involves the analytical techniques, and the fourth discusses the spectroscopical analysis.

2.2.1 Analysis of the USGS Spectral Library

Reflectance spectra of numerous minerals and rocks are available in the USGS Spectral Library, and these spectra can be used to distinguish between different minerals and categorize them according to their spectral characteristics. However, this study focused on contrasting and comparing various iron minerals by first employing hyperspectral data and then resampling to multispectral data. Thus, the applicability of the USGS Spectral Library for this study is crucial, and the following steps were taken:

i. Spectral Features of Iron Minerals were reviewed

The spectral characteristics of iron minerals were reviewed, particularly their absorption features in the VNIR range of the electromagnetic spectrum.

ii. Familiarization with the USGS Spectral Library

Understanding the contents of the USGS Spectral Library was the first step that was conducted in this study. The library's contents were examined to gain insight into the available spectrums for iron minerals. The relevant iron minerals (Jarosite, Goethite, and Hematite) and associated minerals (Quartz and Calcite) were identified, and data on their spectral properties were acquired.

iii. Comparison of spectral signatures

The spectral signatures of several iron minerals in the USGS Spectral Library were compared (Figure 7a-b). This is aimed at providing information on the consistency or not of the spectral features when in association or mixture with various minerals. The shape, position, and depth of the deepest feature and the strength and position of the spectral peaks were given particular consideration. These characteristics set one iron mineral apart from another.

Table 5 The various spectrometers utilized in the USGS spectral library to measure spectrum (modified after Kokaly et al., 2017)

Spectrometer	Wavelength range (nm)	Wavelength range, (cm ⁻¹)	Bandpass description
Beckman	200–3000	50,000–3,333	Standard setting
ASDFR	350–2500	28,571–4,000	full range Standard resolution, average band passes of 5, 12, and 11 nm
ASDHR			High-resolution model, average band passes of 5, 9, and 9 nm
ASDNG			Next Generation model, average band passes of 5, 6, and 6 nm
AVIRIS	370–2500	27,027–4,000	Approximately 10 nm across the wavelength range of the sensor
Nicolet FTIR	1120–21600	8,928–46	4 cm ⁻¹ across the range

2.2.2 Synthesis and Analytical Techniques

The synthetic processes used to create iron-bearing minerals and mixtures will be covered in this section. An illustration of the synthesis is shown in Appendix 1-2. Following that, the analytical techniques will be described. Among these techniques are XRD and ASD analysis, as well as sample preparation and setup.

Finally, as the final approach for this study, multispectral analysis will be discussed. The methodology will be followed in a systematic order, beginning with sample preparation (sample selection, preparation, and synthesis), then sample analysis (XRD and ASD spectral analysis), and ultimately multispectral data processing.

Synthesis of K-Jarosite end-member

The Jarosite synthesis was adapted from the work of (Driscoll & Leinz, 2005). To produce K-Jarosite, ferric sulfate hydrate ($\text{Fe}_2(\text{SO}_4)_3 \cdot n\text{H}_2\text{O}$) (provided by Sigma Aldrich) and potassium hydroxide (KOH) (provided by J.T. Baker Chemicals B.V.) were used. An illustration is shown in Appendix 1-2.

1. In 100 mL ultrapure water, 17.02 g ferric sulfate hydrate ($\text{Fe}_2(\text{SO}_4)_3 \cdot n\text{H}_2\text{O}$) and 5.60 g potassium hydroxide (KOH) were dissolved.
2. Then, the solution was prepared in a covered glass beaker and set on a 95°C stirring hot plate (Appendix 1-2).
3. For 4 hours, a moderate boil was kept going. The solution was then taken off the stirring plate and left to settle (Appendix 1-2).
4. The liquid phase was decanted off once the sediment had settled, and the precipitate was thoroughly washed in de-ionized water twice.
5. The solid product was dried for 24 hours in a 110°C drying oven.
6. About 9 g of K-jarosite was obtained after drying and collecting the material.

Synthesis of Na-Jarosite end-member

The synthesis of Na-Jarosite involves using ferric sulfate hydrate ($\text{Fe}_2(\text{SO}_4)_3 \cdot n\text{H}_2\text{O}$) (provided by Sigma Aldrich) and sodium hydroxide (NaOH) (provided by Sigma Aldrich) was used (Driscoll & Leinz, 2005).

1. First, in a glass beaker with 250 mL of ultrapure water, dissolve 17.02 g of ($\text{Fe}_2(\text{SO}_4)_3 \cdot n\text{H}_2\text{O}$) and 3.99 g of NaOH.
2. On a stirring plate, the solution was put to a moderate boil and left undisturbed for 4 hours (Appendix 1-2).
3. Similar to the previous synthesis procedures, the solution was removed from heat, drained, rinsed with 100 mL of de-ionized water, and dried at 100°C overnight.
4. The dried product weighed 20.7 g.

Synthesis of Goethite

Goethite is an iron oxyhydroxide with $\text{FeO}(\text{OH})$ chemical formula. The formation of goethite is indicated by the oxidation state change of Fe^{2+} (ferrous) to Fe^{3+} (ferric) iron, allowing goethite to exist at the Earth's surface. It was synthesized through a precipitation method that involved the use of an analytical grade ferric nitrate ($\text{Fe}(\text{NO}_3)_3 \cdot 9\text{H}_2\text{O}$) (from Merck KGaA) and Potassium Hydroxide (KOH) (from J.T.Baker Chemicals B.V.). The work of (Jaiswal et al., 2013) was adopted in the synthesis of goethite.

1. In a 1 L sterilized beaker, 50.0 g of analytical grade $\text{Fe}(\text{NO}_3)_3 \cdot 9\text{H}_2\text{O}$ was dissolved in 0.5 L of de-ionized water.
2. For 24 hours, the solution was hydrated at a pH of 1.6 and stirred constantly using a magnetic stirrer.

Discrimination of individual Iron-bearing minerals with the Sentinel-2 Super-Spectral Imager

3. Then, 2.5 M KOH solution was added drop by drop until the solution reached a pH of 12.
4. The thick suspension was aged in a thermostatic oven at 60 °C for ten days.
5. Finally, the goethite paste was dried in an oven at 60°C.
6. The product was ground to powder, and
7. 11.80 g of goethite was produced.

Synthesis of Hematite

As demonstrated, the Hematite synthesis was adapted from the work of Sankadiya et al. (2016). The synthesis of hematite was carried out by simple precipitation. A stoichiometric amount of $\text{FeCl}_3 \cdot 6\text{H}_2\text{O}$ (provided by Merck KGaA) and liquid NH_3 (provided by Merck KGaA) were used.

1. A stoichiometric amount of $\text{FeCl}_3 \cdot 6\text{H}_2\text{O}$ powder was added to 100 mL of de-ionized/ultra-pure water to form a solution.
2. Then, 12g of NaOH in 100 mL water was added drop by drop to the solution under constant stirring.
3. At pH = 8, Fe_2O_3 gradually precipitated out.
4. The precipitate was then filtered and washed several times to remove the excess base (Appendix 1-2)
5. After that, it was dried at ambient conditions for 12 hours.
6. The product was then calcinated in a Muffle furnace at 3000C and 4000C for 24 hours (Appendix 1-2).
7. The product was ground, and a reddish brown was obtained,
8. Weighed 53.74 g of hematite

2.2.3 Characterization of the products (synthetic minerals)

X-ray diffraction (XRD) spectra were utilized to characterize the synthesized products. The concept is that a crystalline material's atomic and molecular structure may be determined by scattering an incoming X-ray beam in different directions specified by the crystalline structure. This was achieved by the products being first prepared by powdering them.

1. Powdering of the product

Powdered product was achieved by grinding the iron mineral products (Jarosite, Goethite, Jarosite) with a mortar and pestle to prepare it for XRD and ASD analyses.

This was achieved by placing the samples horizontally on the goniometer of the D2 PHASER diffractometer. Thereafter, the X-ray tube (rays source) sends rays on the sample, and a detector counts the number of X-rays scattered by the sample. The diffracted X-rays from the crystal planes in the powdered phases at different diffraction angles show peaks with variable intensities. Each phase or mineral's diffraction pattern is determined by its crystal structure, crystallite size, and lattice strain. These were captured on a 2θ scale in the wide-angle region from 60 to 800 using a $\text{CuK}\alpha 1$ radiation wavelength of 1.54 Å on a 30 kV/10 mA D2 PHASER diffractometer. The data was collected after 12 cycles (repeat) within 45 minutes to have a very good counting of statistics and subsequently comparing the resultant diffraction pattern to Joint Committee on Powder Diffraction Standards (JCPD) database. The JCPD database is an

ideal tool for determining the characteristics of various crystalline substances, and it also acts as a reference for comparison and validation.

2. Preparation of mixtures of Iron-Bearing Minerals

This procedure was conducted by mixing the various minerals in different proportions. Weighed using weighing balance. Firstly, the weighed minerals were mixed using a spatula in an aluminum foil. Afterward, more mixing was done using a pestle and mortar by gently grinding the clumps till they became wholly mixed and even. The samples were stored in a well-labeled aluminum foil and nylon sample bag.

Calcite was mixed with the iron-bearing minerals in different proportions, and quartz (provided by Boom B.V. Meppel) was also mixed in different proportions with the iron-bearing minerals (Table 6).

2.2.4 Building spectral libraries

Spectral Analysis of the Synthetic Iron Minerals

An ASD Fieldspec Full Range Spectrometer was used to measure high-resolution laboratory reflectance over the wavelength range of 350 to 2500 nm, with a halogen lamp for illumination and a Spectralon panel as a white reference. The ASD spectrometer has a spectral resolution of 5 nm from 350 to 1000 nm and an 11 nm resolution from 1000 to 2500 m. A total of twenty-nine (29) spectra for each synthetic mineral were acquired for this study. The following procedure was used to collect data. It is important to note that the spectra were measured in two different sessions.

1. The powdered iron minerals were placed on a flat glass holder, and the top was leveled.
2. Fieldspec was used to collect the spectra.
3. The spectral measurements were carried out using RS3 software which is wirelessly connected to the instrument,
4. The measurements were repeated five times, and the average was obtained.
5. Further processing of the data, such as splice correction that fixes the spectral discontinuity caused by the use of three detectors located at 1000 nm and 1800 nm, was carried out with the aid of ViewSpecPro software.
6. The spectra were then exported in ASCII format and
7. The ENVI program was used to examine and analyze the various spectra.
8. The data were exported to Excel for further analysis.

Resampling of high-resolution spectra to Sentinel-2

High-resolution spectra of twenty-nine (29) iron mineral samples (listed in Table 6) were resampled to eleven (11) bands of Sentinel-2 (excluding bands 1 and 10) (Figure 9). Landsat 8 and ASTER were also resampled to evaluate how well they perform at distinguishing various iron minerals compared to Sentinel-2 (Figure 9). The resampling procedure was conducted in ENVI Software utilizing the response function of the Sentinel-2 bands. In the process of resampling the hyperspectral spectra to align with the multi-spectral spectral resolution, the response function was used. This technique was essential to ensure the compatibility of the hyperspectral data with the spectral response of the multi-spectral sensors, thereby allowing for more accurate comparison and analysis of the data. In addition, it gives a better approximation of the original spectral features while accounting for the broader band width of the multi-spectral sensors. This approach helps maintain the important spectral information and provides a better comparison between the different data sets. It helps to minimize the effects of spectral distortion and spectral smoothing that could occur during the resampling process.

2.2.5 Band Ratio

This section discusses the technique that explores the opportunity that various iron minerals present distinctive spectral features, including unique absorption and reflection features along specific wavelength regions. Consequently, this method involves employing specific band ratios to take advantage of these variations and successfully distinguish between different iron minerals. Based on the unique characteristics of the iron minerals' absorption, the best band combinations are chosen. A lot of thought went into avoiding spectrum overlap or confounding effects from other combinations. After Resampling was carried out successfully, a spectral variation approach in the various bands of Sentinel-2 was employed to distinguish the individual iron-bearing minerals.

The following band ratio techniques were used.

a) Simple band ratio

For example, in band a/band b, the reflectance values in band A are divided by the values in band b for each pixel. The resulting value will be high if the reflectance in band A is significantly higher than in band b and low if the reflectance in band a is lower than or similar to band b.

b) Band-ratio combination (summation)

Combining the two band ratios by summing them provides a composite value that incorporates information from the spectral ranges of the bands involved.

c) Relative absorption band-depth technique

The Relative absorption band depth approach (Figure 2) involves dividing the sum of the two highest-reflectance spectral bands in the spectral wavelength range, which may or may not be in sequence, by the deepest absorption feature (Crowley et al., 1989).

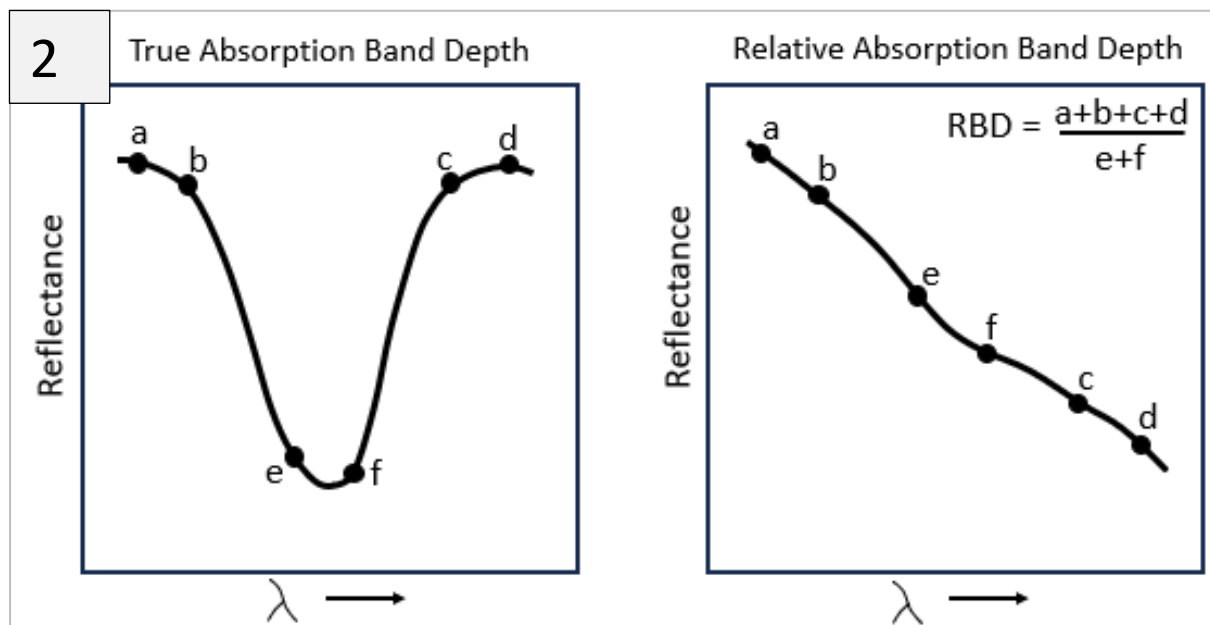


Figure 2 True and relative absorption band depth concept (modified after Crowley et al., 1989).

The distribution and relationship between the band ratios for different iron-bearing minerals were observed by visualization and analysis of the scatter plot. A 'supported triangular trend' technique was employed to aid in identifying trends, patterns, or clusters among the iron-bearing minerals based on their band ratios. This technique provides valuable insights into the spectral characteristics and distinguishing features of different minerals, which are crucial for mineral identification and discrimination.

The 'supported triangular trend' in this context refers to a specific distribution pattern of mineral data points associated with three main classes of iron minerals that occupy distinct vertices of a triangle. This

Discrimination of individual Iron-bearing minerals with the Sentinel-2 Super-Spectral Imager

triangular distribution can provide a clear graphical representation of the relationships and distinctions between the minerals. The position of each point on the plot represents the specific combination of band ratios for a given mineral. Thus, each mineral is represented by a point on the plot, where the x-axis corresponds to the band ratio B_x/B_y , and the y-axis corresponds to the band ratio B_a/B_b . This makes it possible to analyze the associations among the minerals using the available band ratios, as well as the performance of the ratios to distinguish the different iron-bearing minerals.

Assessments of the Existing band ratios

This technique begins with testing each band ratio in the laboratory to examine their capability to distinguish between iron minerals. One key metric used in this assessment is the distinguishable score. In essence, this score is a numerical representation that differentiates one mineral from another based on the specific band ratio. The higher the distinguishable score, the greater the difference between minerals as per the band ratio in question. This was conducted on twenty-nine (29) synthetic iron mineral samples (Table 6) ranging from pure iron minerals (jarosite, goethite, and hematite) to iron mineral mixtures and mixes with other minerals (quartz and calcite).

To achieve this, five steps were followed systematically to observe the relationship between these minerals, their mixtures with each other, and with other minerals, and to determine which of these band ratios distinguishes between the iron minerals.

1. First step: test band ratios on pure iron minerals and examine their performance
2. Second step: test band ratios on mixtures of iron minerals with each
3. Third step: test band ratios on iron minerals with mixtures of quartz
4. Fourth step: test band ratios on iron minerals with mixtures of calcite
5. Fifth step: test band ratios on iron minerals with mixtures of both Quartz and Calcite

Experimenting with new band ratios

The results of the analysis of the existing band ratios were used to demonstrate the iron mineral that can be distinguished by the band ratios. This was achieved by following the steps described below:

1. Step 1: Compute the band ratios for each of the Sentinel-2 bands (excluding bands 1 and 10): compute the band ratios of each band with all the other bands.
2. Step 2: Identify and select the band ratio that identifies a specific iron mineral (jarosite, goethite, hematite); that is the ratio that assigns the highest score to a specific iron mineral.
3. Step 3: Experiment with the ratios of pure iron minerals using a scatterplot.
4. Step 4: Experiment with the ratios of iron minerals with mixtures of each other.
5. Step 5: Experiment with the ratios of iron minerals with mixtures of quartz.
6. Step 6: Experiment with the ratios of iron minerals with mixtures of calcite.
7. Step 7: Experiment with the ratios of iron minerals with mixtures of quartz and calcite.

Evaluation of the New Band Ratios

The evaluation involves a detailed comparison of the novel band ratios with published reference data in a real-world geological context from the Cuprite area (shown in Figures 3a and b). The accuracy or lack thereof of matching with reference data, the ability to identify specific minerals, and how applicable it is to real-world geological settings define success or failure. Two types of reference data from the Cuprite area were used: 1). A mineral map using the 400 to 1300 nm electronic absorption band of the AVIRIS data, reflecting the spectrally dominant iron-bearing minerals, and 2). A mineral map covering the 1300 to 2500 nm vibrational absorption wavelength region of the AVIRIS data shows other spectrally dominant minerals such as clays, micas, sulfates, and carbonates. Successful discrimination between the iron minerals in the generated S2 imagery compared to the reference maps indicates that the ratios work. Therefore, the performance of these ratios in a real world geological setting like a Cuprite area was analyzed to ensure practical applicability beyond a controlled laboratory setting.

The google earth engine platform was used to evaluate the capability of the novel band ratios in discriminating iron-bearing minerals on Sentinel-2 imagery covering the Cuprite mining district in Nevada, USA. Sentinel-2A Level-1A surface reflection image collection from January 2019 to January 2020 was used in this study. This dataset, which is 7.5 km by 7.2 km in dimensions, is cloud-free and covers the Cuprite region. The Sentinel-2A data includes ten VNIR and three SWIR bands. The specifications and characteristics of these bands, including their respective spectral ranges and resolutions, are outlined in Table 1.

The Cuprite region was chosen because of the distinct geological and climatic features that make it a particularly fitting site for this research. Firstly, the Cuprite area falls under the arid to semi-arid climate category. This climatic condition leads to limited vegetation cover, reducing the spectral interference from vegetation, which often complicates iron-bearing minerals remote sensing studies. Secondly, the region is well-known for its mineral diversity, particularly the iron-bearing minerals of interest: goethite, hematite, and jarosite. The rich presence of these minerals, owing to the area's significant geological activity, provides ample data for examination. Furthermore, the Cuprite area has been serving as an excellent test site for remote sensing applications in geology for years (Mars & Rowan, 2010; Rowan et al., 2003; Swayze et al., 2014). This is due to its exposed surface mineralogy and the well-documented studies available for validation (Swayze et al., 2014).

Discrimination of individual Iron-bearing minerals with the Sentinel-2 Super-Spectral Imager

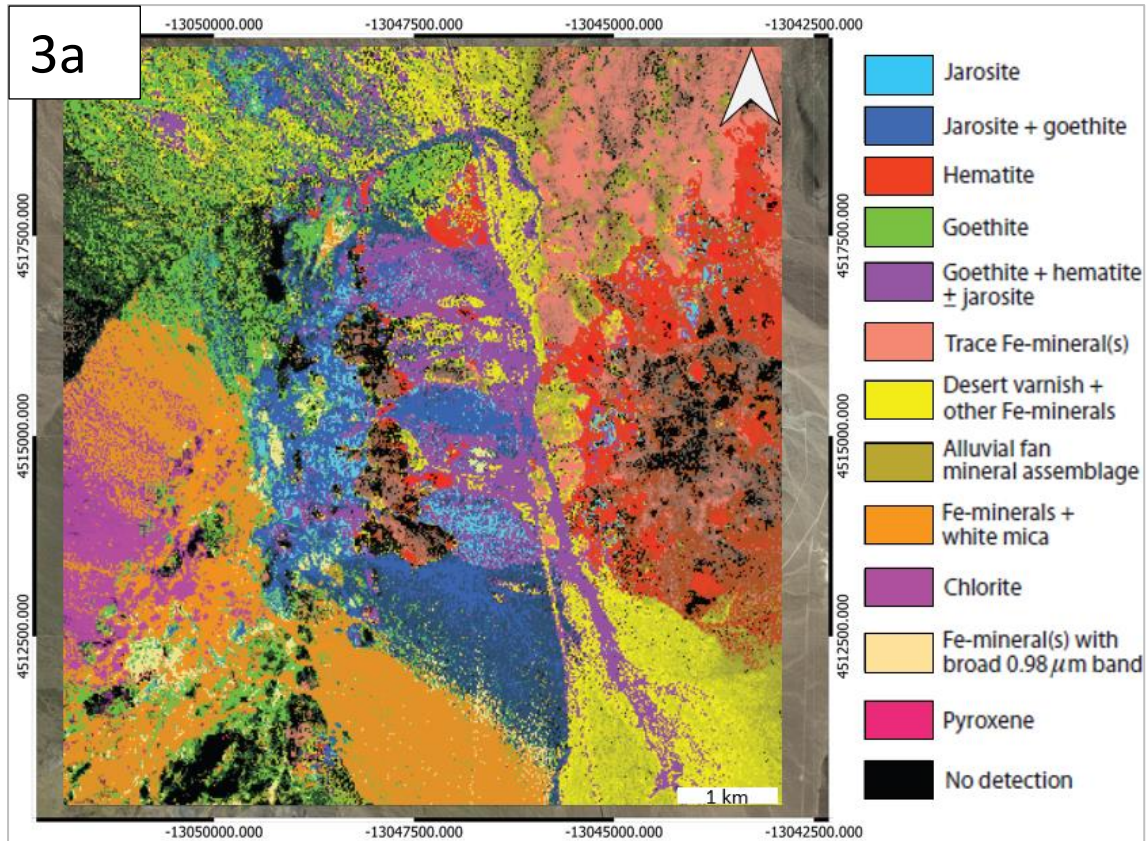


Figure 3a Mineral map utilizing the 400 to 1300 nm electronic absorption band of the AVIRIS data, showing the spectrally dominant Iron-bearing minerals at Cuprite.

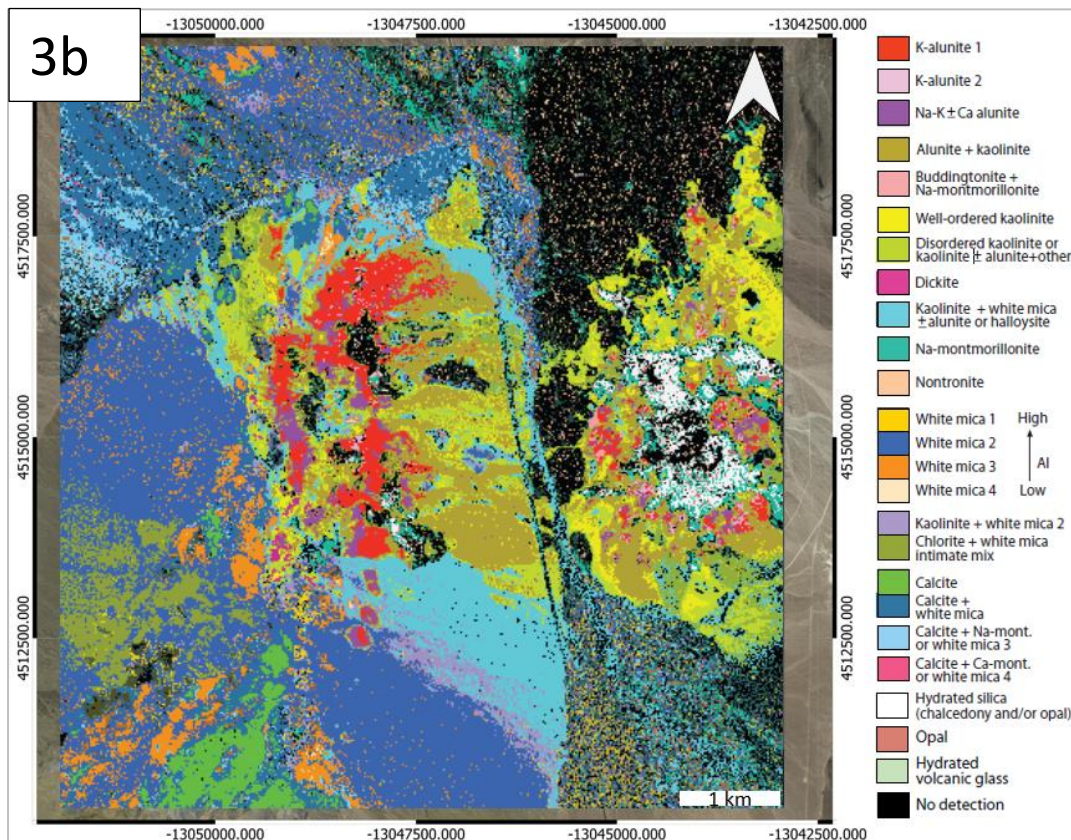


Figure 3b Mineral map of the 1300 to 2500 nm vibrational absorption wavelength region of the AVIRIS data, showing the spectrally dominant clays, micas, sulfates, and carbonates at Cuprite.

3 RESULTS

In this section, the results of mapping iron minerals with the new band ratios for eventual evaluation are presented, paving the way for their subsequent evaluation. The section is divided into five distinct subsections. The initial subsection presents the findings derived from the laboratory experiment and subsequent characterization efforts. The second subsection shows the spectroscopic analysis conducted on synthetic iron minerals. The third subsection assesses the relevance and applicability of the USGS Library in the context of this study. The fourth subsection is dedicated to the analysis of the existing band ratios, illustrating their strengths and potential limitations. Lastly, the fifth subsection presents the novel band ratios that have emerged as a result of this study, revealing their potential implications and capability in discriminating iron minerals.

3.1 Laboratory Experiment and Characterisation

In the laboratory synthesis of the minerals, a systematic method was employed for assigning identification to the samples based on their composition and proportions. This classification is delineated in Table 6. For instance, the ID "Gth-010" was attributed to 100% pure goethite, containing no mixtures of other minerals. Conversely, the ID "Gth75Q25" designates a compound consisting of 75% goethite and 25% quartz. Likewise, the ID "Gth50Q50" signifies an equal proportion of goethite and quartz, with each constituent making up 50% of the mixture. The ID "Gth25Q75" represents a mixture of 25% goethite and 75% quartz. This identification system was applied uniformly across all mineral samples and mixtures, ensuring a coherent representation of the constituents within the synthesized products, thereby providing an equitable basis for comparison.

Table 6 Samples description and identification

	Sample ID	Description
1	Gth-010	100% Goethite
2	Hm-100	100% Hematite
3	Jsk-100	100% K-Jarosite
4	JsNa-100	100% Na-Jarosite
5	Gth75Q25	Goethite 75%; Quartz 25%
6	Gth50Q50	Goethite 50%; Quartz 50%
7	Gth25Q75	Goethite 25%; Quartz 75%
8	Gth75CaCO25	Goethite 75%; Calcite 25%
9	Gth50CaCO50	Goethite 50%; Calcite 50%
10	Gth25CaCO75	Goethite 25%; Calcite 75%
11	Gth75Jsk25	Goethite 75%; K-Jarosite 25%
12	Gth50Jsk75	Goethite 50%; K-Jarosite 50%
13	Gth25Jsk75	Goethite 25%; K-Jarosite 75%
14	Hm75Q25	Hematite 75%; Quartz 25%
15	Hm50Q50	Hematite 50%; Quartz 50%
16	Hm25Q75	Hematite 25%; Quartz 75%

17	Hm75CaCO25	Hematite 50%; Calcite 50%
18	Hm50CaCO50	Hematite 50%; Calcite 50%
19	Hm25CaCO75	Hematite 25%; Calcite 75%
20	Hm75Gth25	Hematite 75%; Goethite 25%
21	Hm25Gth75	Hematite 25%; Goethite 75%
22	Hm75Jsk25	Hematite 75%; K-Jarosite 25%
23	Hm50Jsk25	Hematite 50%; K-Jarosite 50%
24	Hm25Jsk75	Hematite 25%; K-Jarosite 75%
25	Hm50JsNa50	Hematite 50%; Na-Jarosite 50%
26	Jsk75Q25	K-Jarosite 75%; Quartz 25%
27	Jsk50Q50	K-Jarosite 50%; Quartz 50%
28	Jsk50CaCO50	K-Jarosite 50%; Calcite 50%
29	Jsk25CaCO75	K-Jarosite 25%; Calcite 75%

3.1.1 Characterisation of the products

In this section, results from the X-Ray Diffraction (XRD) analysis conducted on the minerals jarosite, goethite, and hematite are illustrated. The peak patterns obtained were compared to the profiles published in the Joint Committee on Powder Diffraction Standards (JCPDS) database for the respective iron-bearing minerals. This validates the reliability of the synthesized minerals used in the research. Full details of the XRD analysis, including specific peak positions and how they relate to their crystal system, will be presented in the discussion chapter of this study, as illustrated in Figure 4a - c below.

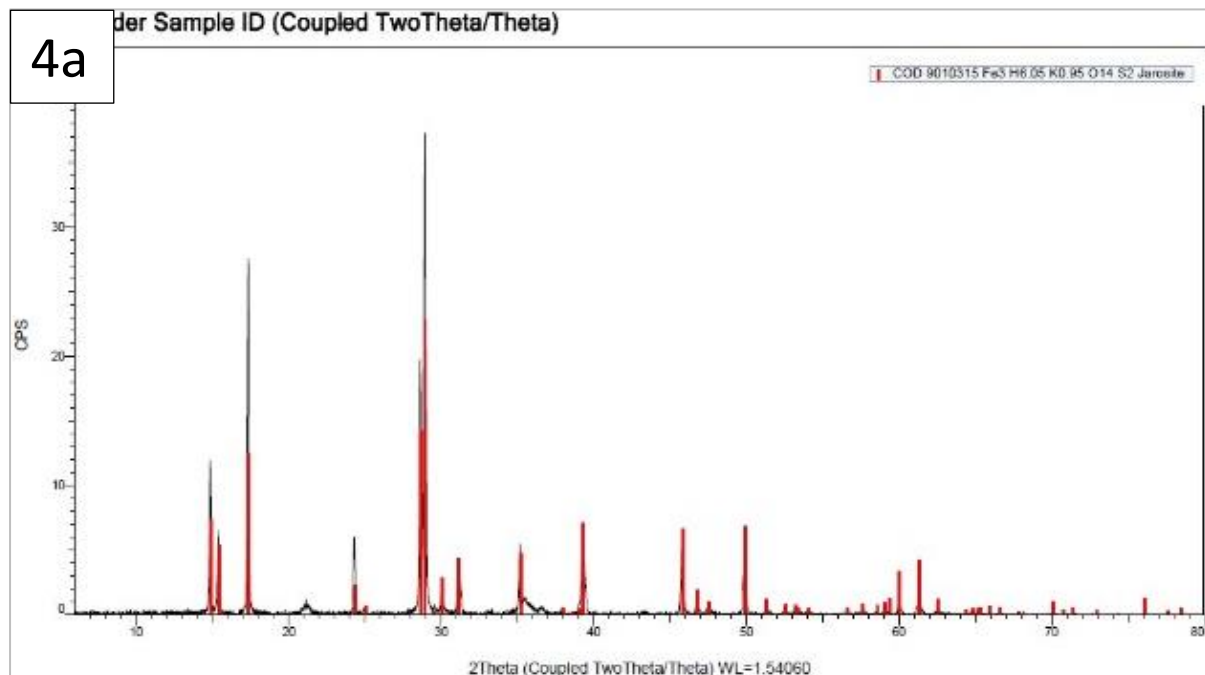


Figure 4a Synthetic XRD pattern shows distinct peaks, with the most intense peak often observed around 17 and 29 degrees 2-theta and other smaller peaks at different angles.

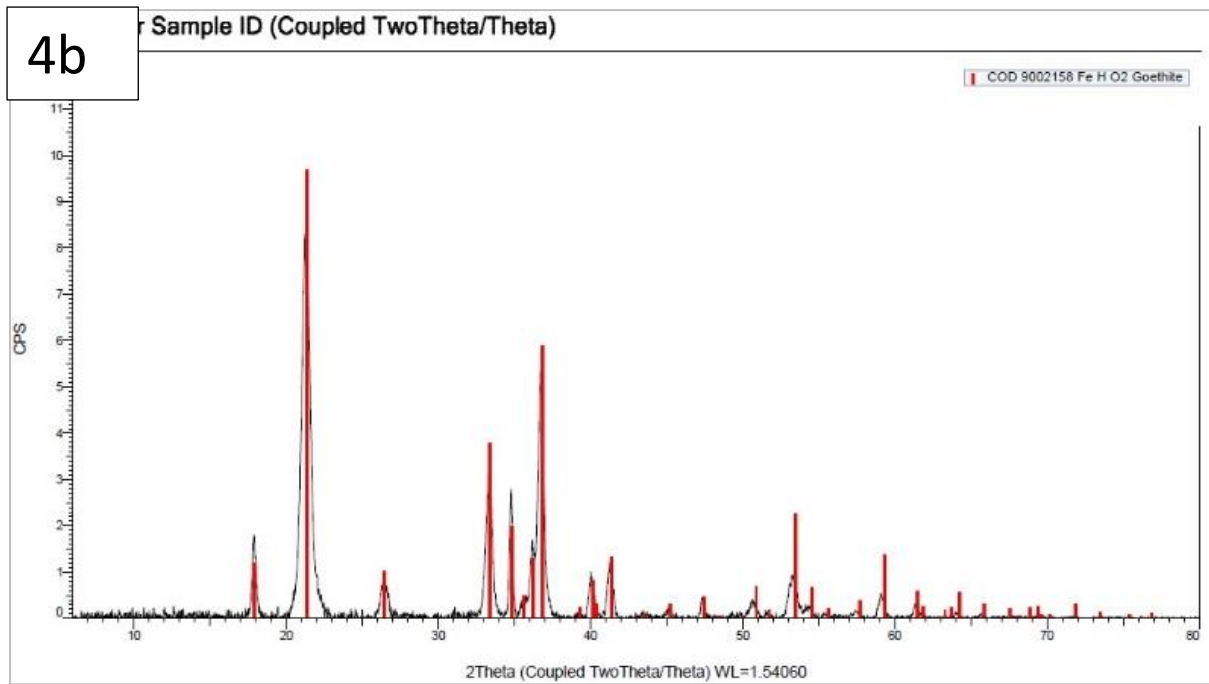


Figure 4b Goethite XRD profile shows a strong diffraction peak around 21 and 37 degrees 2-theta and other smaller peaks at different angles.

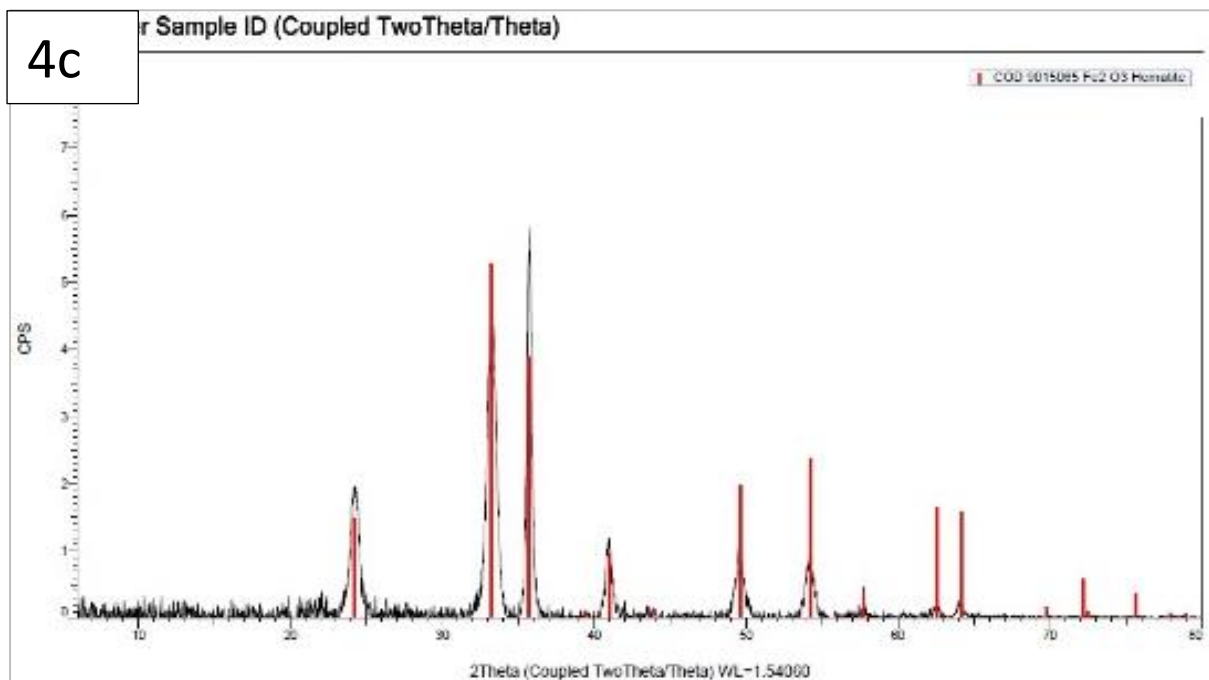


Figure 4c Hematite XRD pattern characterized by several peaks. The most intense peak is usually observed around 33 and 36 degrees 2-theta, and other smaller peaks at different angles.

3.2 Spectroscopic analysis

Firstly, the observation of the products’ different shades of color as they relate to the spectral features is analyzed. Then the second part is a comparison of the spectra with the USGS Spectral Library as it relates to the study (Figure 5). This section concludes with spectral analysis of the products in different proportions and compositions, demonstrating the relationship between mixtures (gangue) and spectral features.

3.2.1 Spectral Analysis of the synthetic minerals

The synthetic minerals exhibit absorptions caused by electronic processes involving crystal field and charge transfer absorption in the VNIR (380 - 1000 nm) electromagnetic spectrum (Figure 5). In addition, jarosite absorbs in the SWIR due to the Fe-OH bond. Spectra collected in the lab revealed that hematite absorbs at 520 and 867 nm, goethite at 659 and 929 nm, and jarosite at 906 nm, characteristic of the crystal field absorptions. An absorption characteristic resulting from charge transfers can also be observed at 436 nm, 474 nm, and 520 nm for jarosite, goethite, and hematite, respectively (Table 7).

Table 7 Observed wavelength positions of absorption characteristics in iron-bearing minerals (findings from the current study).

	VNIR			SWIR
	Charge transfer absorptions	Crystal field absorptions		Fe-OH Absorptions
		Second deepest feature	Deepest feature	
Jarosite 100%	436	-	906	2267
Goethite 100%	474	659	929	-
Hematite 100 %	520	660	867	-

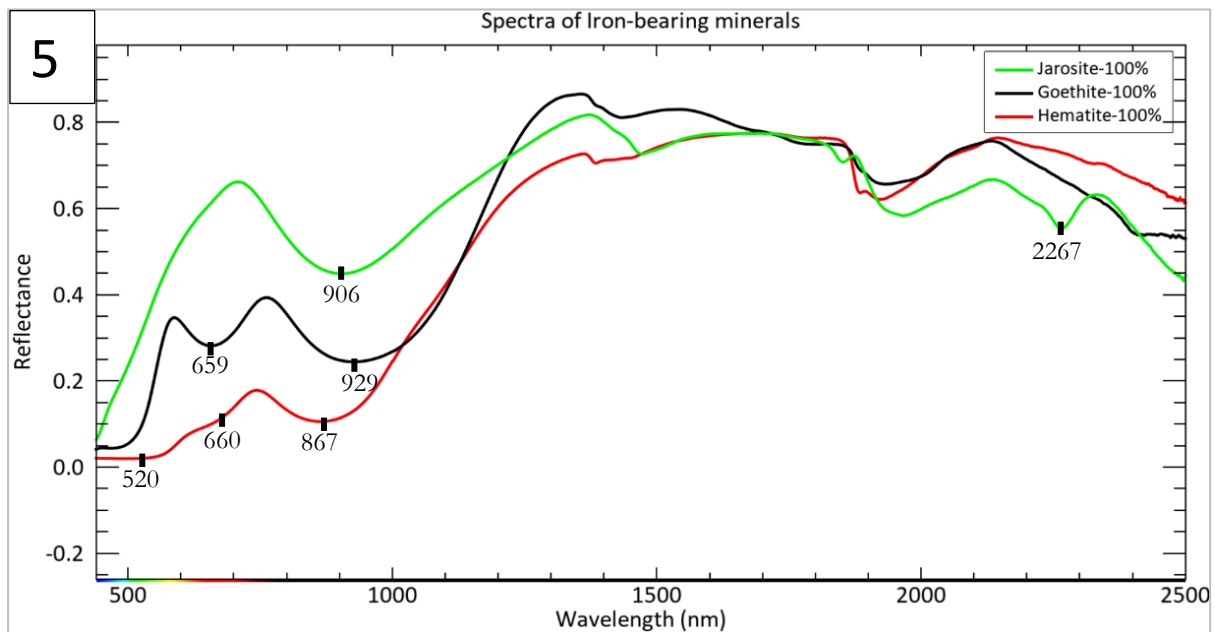


Figure 5 High-resolution reflectance spectra of iron minerals exhibiting distinct VNIR absorptions caused by crystal field and charge transfer processes (from this study).

Figure 6 shows photography of different shades of colors of the synthetic minerals (iron-bearing minerals). The colors observed range from pale yellow (jarosite) and brown (goethite) to deep red (hematite). The pale yellow jarosite absorbs the blue light, while the goethite appears brown, with absorption also in the blue wavelength region. In contrast, hematite displays a deep red color and strongly absorbs the blue and green wavelength regions of the spectrum (Figure 5).



Figure 6 Powdered products of synthetic iron-bearing minerals (from current study).

3.2.2 Comparison with the USGS Spectral Library

The analysis and evaluation of the USGS Spectral Library show that the spectra of the specific iron minerals are available in different proportions and mixtures (Table 8, Figure 7a - c). A comparison of produced iron-bearing minerals and available spectra from the USGS library is illustrated in Figure 7a - c. The compositions of hematite spectra range from quartz, mica, and kaolinite, while the quantities vary from 2% to unspecified. The spectra of jarosite from the USGS Library show the broad feature around 900 nm and 2250 nm, just like the synthetic mineral (Figure 7c). However, some spectra exhibit shallow depth, weak shoulders, and additional features like Goethite0.02+Quartz_GDS240_BECKa_AREF, Chlor+Goethite_CU93-4B_Phyl_BECKa, and Hematite_HS45.3_ASDFRb. These differences coincide with the information shown in Table 9, where variety in composition and spectrometer were tabulated from the metadata. Furthermore, the spectrum of Jarosite_GDS98_K_90C_Syn_NIC4a does not have features in the VNIR coinciding with the spectrometer specification. Also, Jarosite_WS368_(Pb)_BECKc spectrum exhibits weak iron features (Figure 7c). Similarly, the spectra of goethite and hematite from the USGS Library and synthetic mineral exhibit features around 900 nm, although some exhibit deep feature diagnostic of the minerals while others appear shallow.

Discrimination of individual Iron-bearing minerals with the Sentinel-2 Super-Spectral Imager

Table 8 Summary of USGS Spectra metadata of the iron minerals (modified after Kokaly et al., 2017).

Iron mineral Spectra ID (USGS)		Spectrometer	Mixtures (Gangue)				
			Quartz (wt %)	Calcite (wt %)	Mica (wt %)	Feldspar (wt %)	Other mixtures wt%
Jarosite	Jarosite_GDS636_K_Penalt325um_ASDNGa	ASD	-	-	-	-	No impurity
	Jarosite_GDS98_K_90C_Syn_NIC4a	Nicolet	-	-	-	-	No impurity Synthetic
	Jarosite_WS368_(Pb)_BECKc	Beckman	-	-	-	-	Cerussite, alunite, lead
	Jarosite_on_Qtzite_BR93-34A2_BECKa	Beckman	Yes (unspecified)	-	Muscovite	-	-
Goethite	Goethite.02+Quartz GDS240 BECKa AREF	Beckman	98	-	-	-	-
	Goethite_Phyllite CU91-236A	ASD	Yes (unspecified)	Yes	Muscovite, Biotite	Plagioclase	Other impurities
	Goethite MPCMA2-B FineGradjBECKb AREF	Beckman	Yes (unspecified)	Yes	Muscovite	Microcline,	-
	Chlor+Goethite_CU93-4B_Phyl_BECKa	Beckman	-	-	Muscovite	-	Chlorite, Magnetite
Hematite	Hematite.02+Quartz.98_GDS76_BECKa	Beckman	Yes (unspecified)	-	Muscovite	Yes (unspecified)	Quartzite, Kaolinite,
	Hematite_GDS69.g_lt10um_NIC4dcc	Nicolet	Yes (unspecified)	-	-	-	Maghemite
	Hematite_FE2602_BECKkb	Beckman	-	-	-	-	Pyroxene, Feldspar
	Hematite_HS45.3 ASDFRb	ASD	Yes (unspecified)	-	-	-	Maghemite

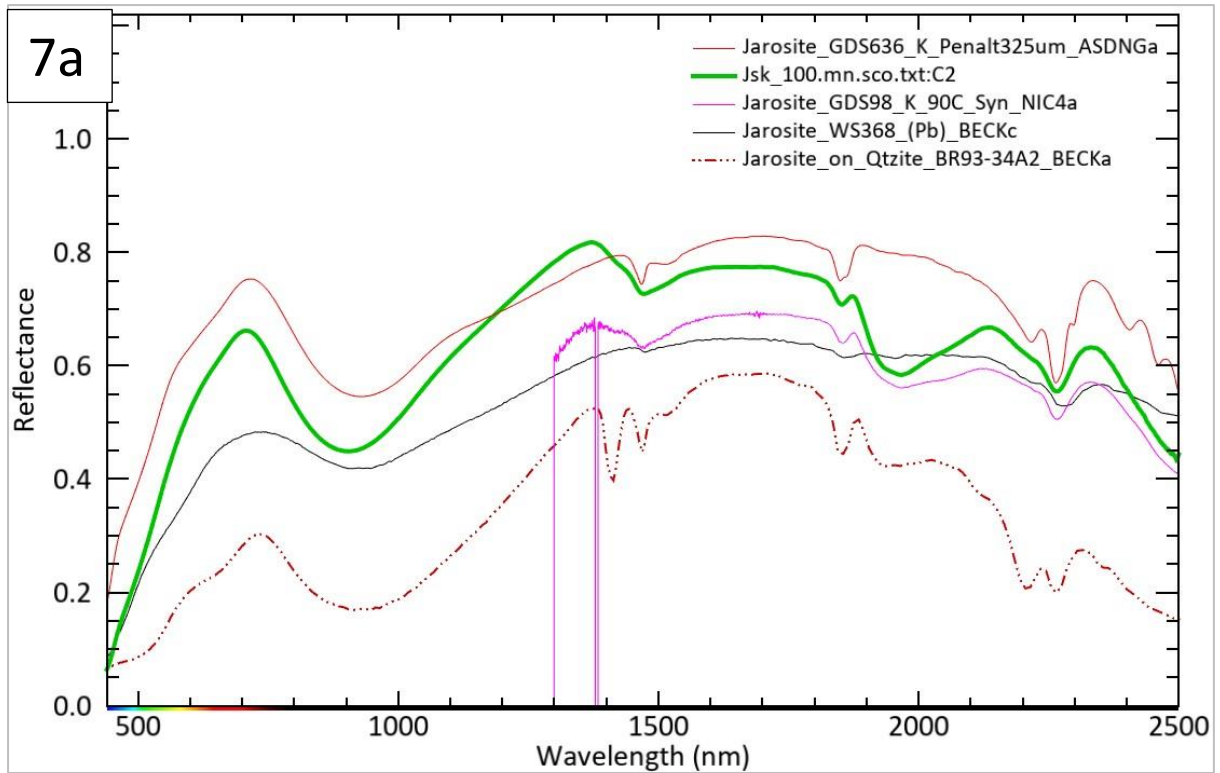


Figure 7a Mineral spectra from the USGS Spectral Library (Kokaly et al., 2017) against synthetic jarosite spectra (from the current study).

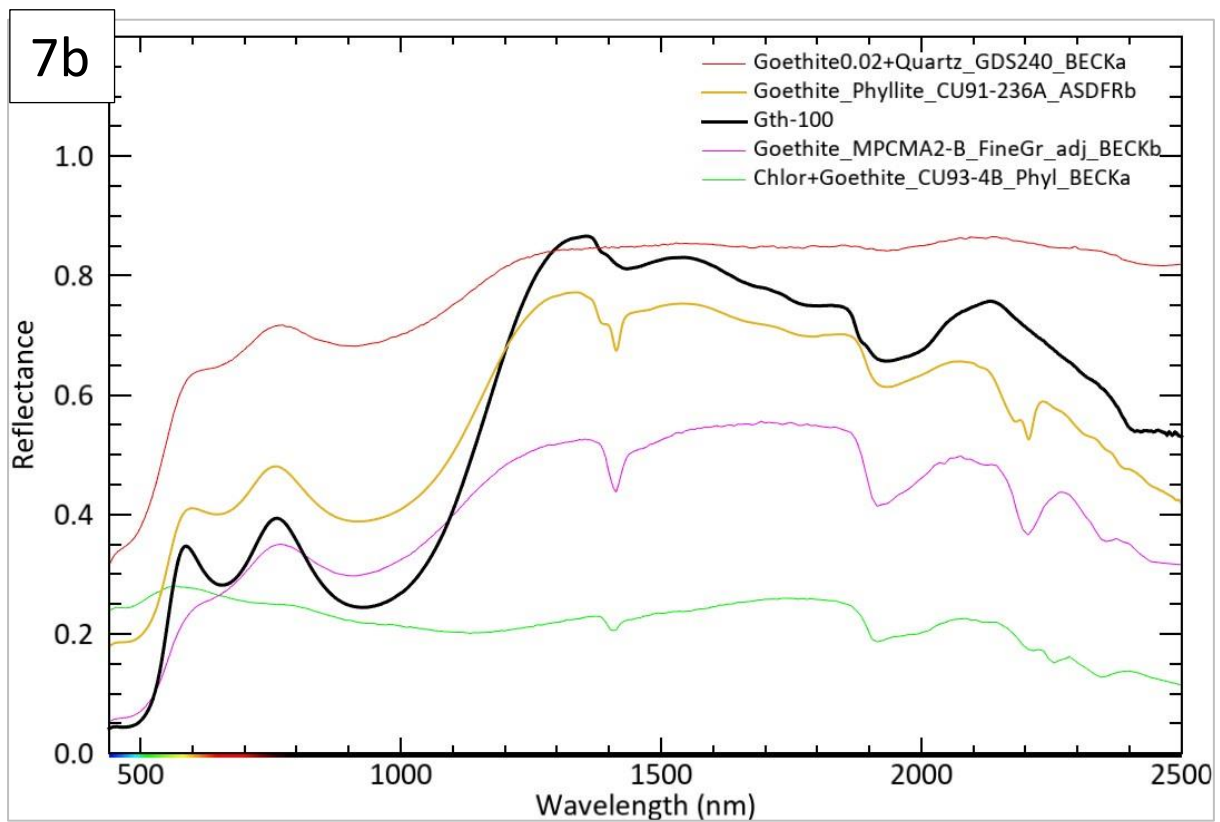


Figure 7b Mineral spectra from the USGS Spectral Library (Kokaly et al., 2017) against synthetic hematite spectra (from the current study).

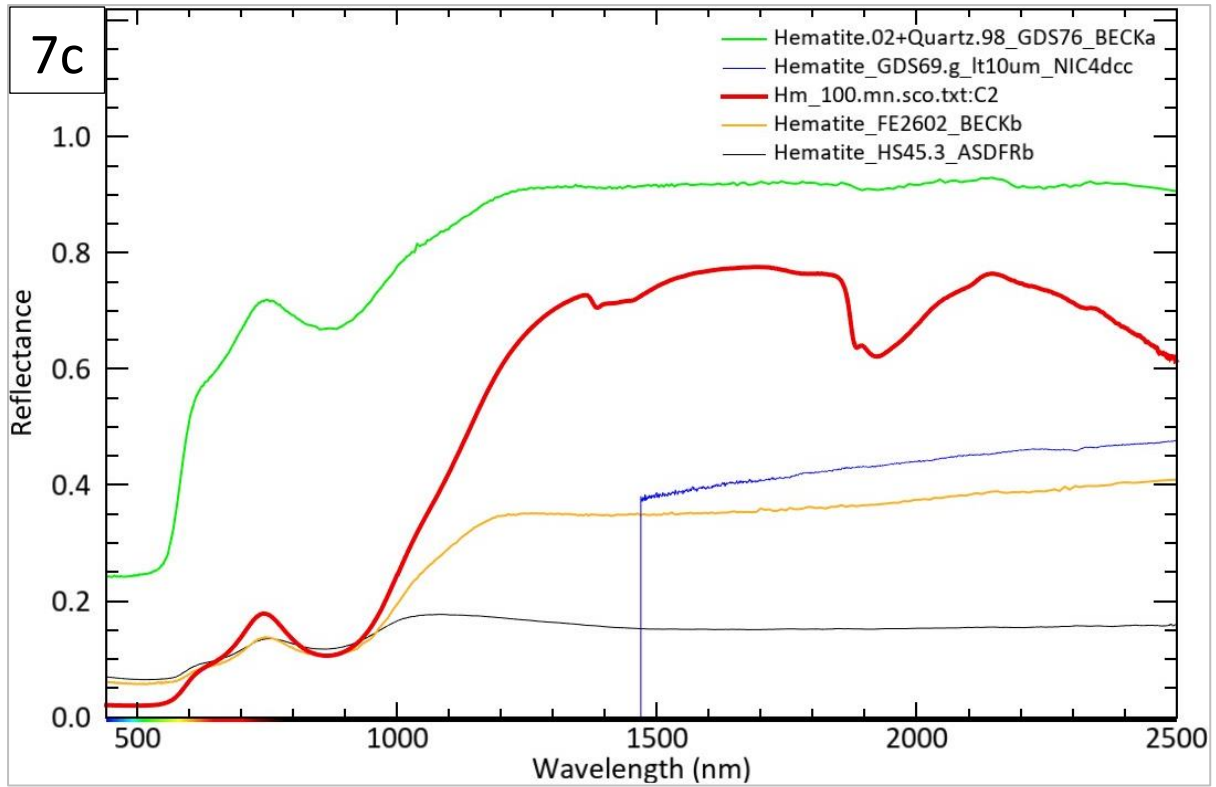


Figure 7c Mineral spectra from the USGS Spectral Library (Kokaly et al., 2017) against synthetic hematite spectra (from the current study).

3.2.3 Spectral Analysis of the Synthetic Iron minerals

As the concentration of the synthetic iron mineral increases or decreases, the intensity and hue of the color vary, as shown in Figure 6. In addition, absorption features become narrower with less intensity as the concentration varies. Consequently, analysis of a mixture of goethite and jarosite spectra combines individual spectral features, which results in a new, more complex spectral signature. The spectra of the mixtures exhibit a combination of absorption and reflection bands from both minerals. More also, the shades of color go from brown to pale yellow as the concentration varies (Figure 6). Furthermore, 25% hematite with a lighter shade of brown exhibits narrower features around 500 nm compared to 100% hematite with deep red color and possesses a broader and more intense feature (Figure 6).

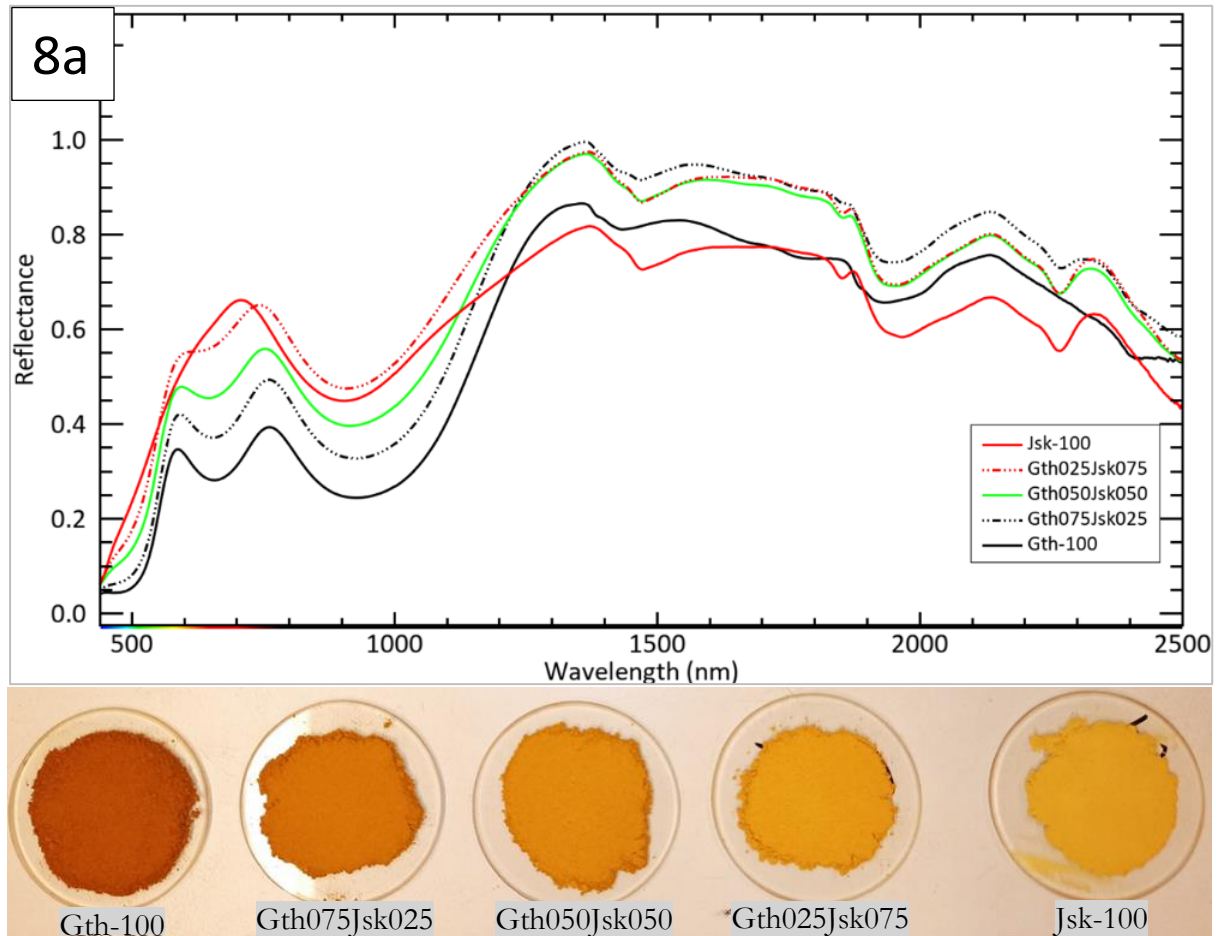


Figure 8a Spectra of pure goethite, jarosite, and their mixtures. Each mixture exhibits combined characteristics.

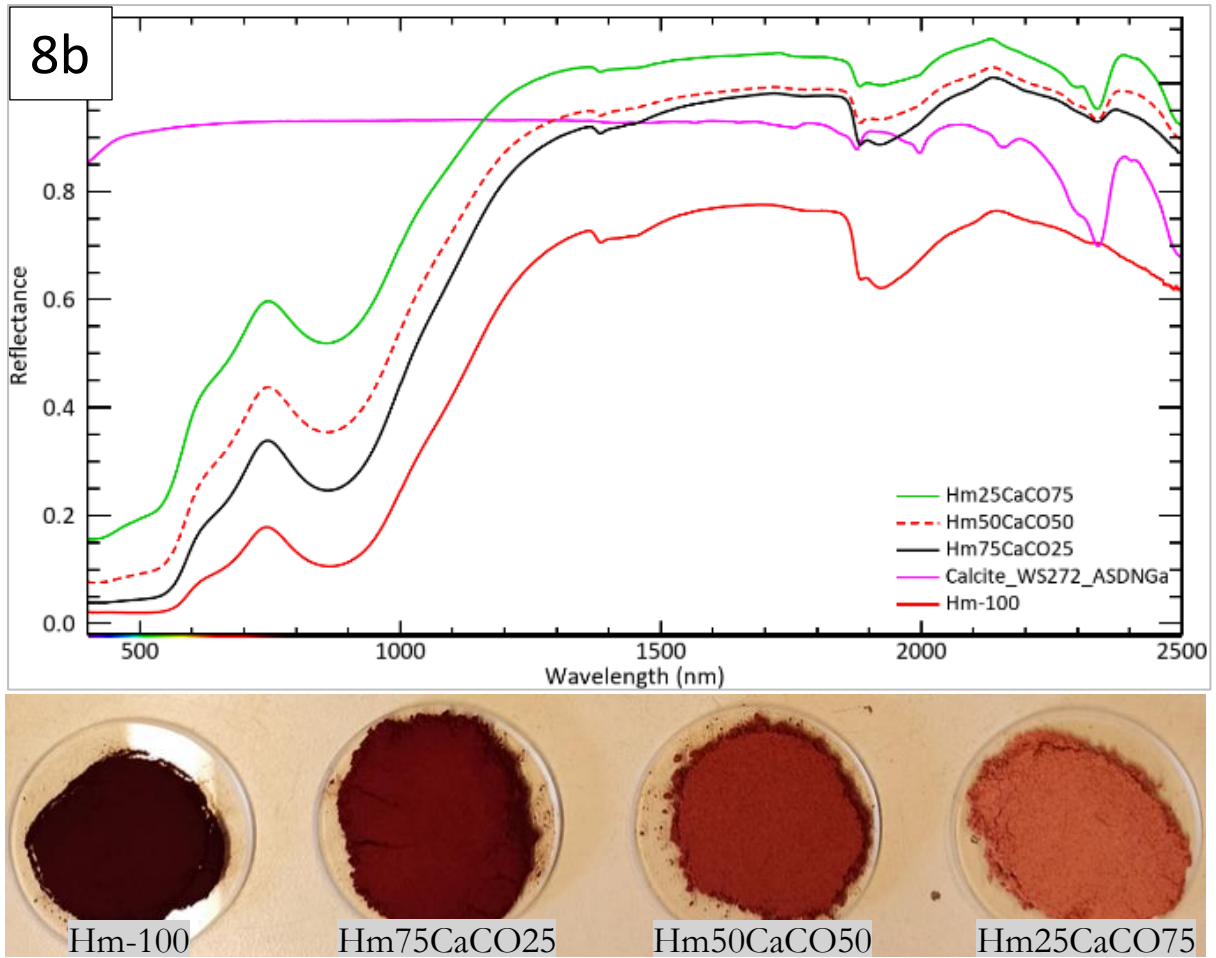


Figure 8b Spectra of pure hematite and its mixture with calcite against spectra of calcite from the USGS spectral library. b). Picture showing different shades of hematite in varied concentrations.

3.3 Band Ratios

3.3.1 Multispectral Sensor Resampling and Comparison

The outcomes from the process of resampling spectra to match the resolutions of multispectral sensors - namely Sentinel-2, Landsat 8, and ASTER is presented in this section. This step was carried out with the intention of facilitating more effective comparisons and supporting subsequent band ratio experiments. The subsequent Figure 9 provides a comparison of high-resolution spectra obtained from synthetic iron minerals, as recorded by the ASD, with their resampled equivalent in Sentinel-2, Landsat 8, and ASTER. To aid in visual clarity, the plotted spectra have been offset. Starting from the bottom, the ASD spectra for synthetic minerals are illustrated in black. The resampled Sentinel-2 spectra are depicted in green, while red represents resampled OLI spectra. At the top, are the resampled ASTER spectra. Each spectral plot is marked with small dots that denote the bands of the corresponding sensors. Due to the ASD's extensive band range, its spectra display a smoother curve.

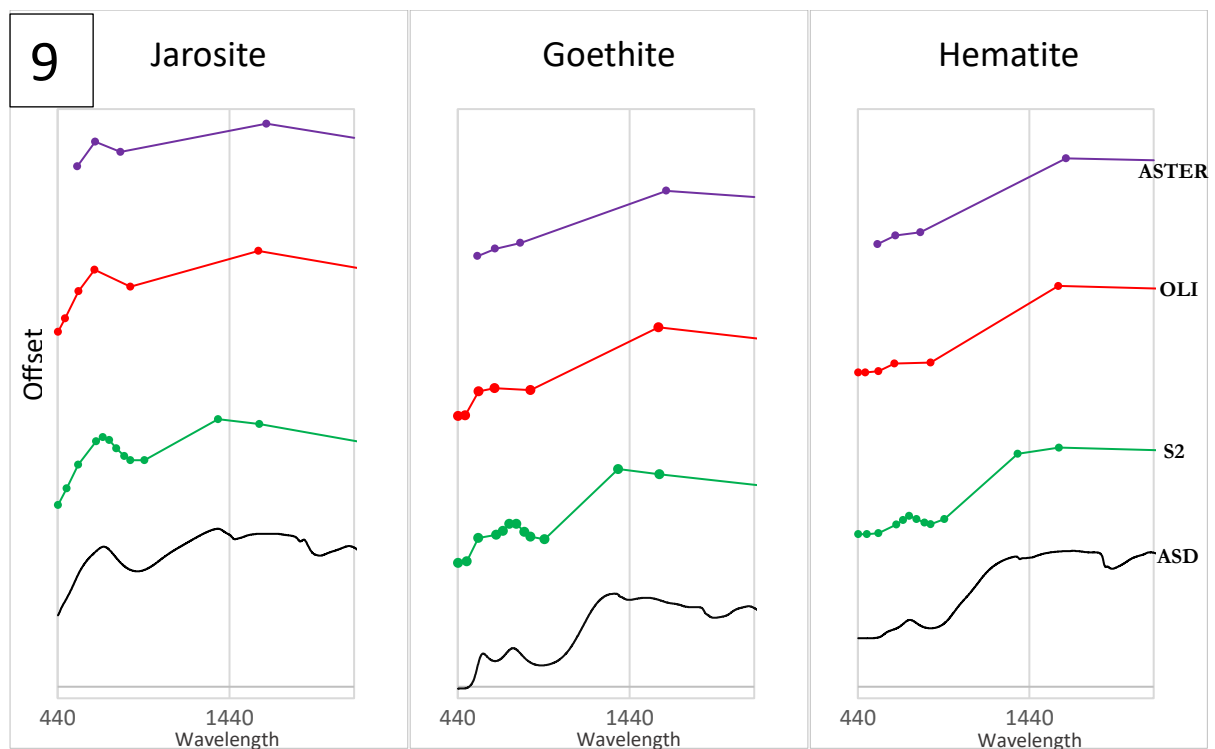


Figure 9 Resampled spectra of jarosite, goethite, and hematite to ASTER, OLI, and Sentinel-2. Graphs are offset.

3.3.2 Assessments of the Existing band ratios

This section focuses on the evaluation of various band ratios cited in the literature, specifically B4/B3; B4/B2; B11/B8; $(B4/B2) \times (B4+B11)/B8$; $(B4+B11)/B8a$; $(B12/B8) + (B3/B4)$; $(B3+B11)/(B4+B8)$; $(B4+B11)/B8a$ (Table 3). From the analysis, it was found that the B4/B3 ratio yielded a distinguishable score that effectively separated hematite from jarosite and goethite. This outcome is illustrated in Figures 10-12, and the corresponding analysis is summarized in Table 9. Subsequently, based on these results, three band ratios from the existing set were chosen to further investigate their proficiency in distinguishing between the iron minerals. Moreover, the analysis of other band ratios has also been performed and is included in the Appendix 1-2 for a comprehensive reference.

Scatterplot of (B11/B8) vs (B4/B3)

This section tested the existing band ratios (B11/B8) against (B4/B3). Figure 10a shows the resampled spectra of the minerals and the corresponding band positions, denoted by small circles, that were used in the ratios. The band ratios were first explored using scatterplots of pure iron minerals, and the relationship showed a nonlinear distribution. The experiment was continued with mixtures of iron minerals, followed by Quartz and Calcite mixtures. Also, using a supported triangular trend, Figure 10b illustrates the relationship between iron minerals and their varying compositions. The result shows that the iron minerals were assigned distinct scores, with hematite mixtures receiving a high score from both ratios, while goethite mixtures gaining an intermediate score from B11/B8 and a low score from B4/B3, and jarosite mixtures receiving lower and intermediate scores from B11/B8 and B4/B3, respectively.

Furthermore, the observation from the results shows that B4/B3 assigned distinct scores to hematite than goethite and jarosite, whereas B11/B8 appears to assign a different score to the minerals when tested on pure minerals, as illustrated in Figure 15b. However, as mixing begins with other minerals, it mixes the scores and does not discriminate between the minerals, as shown in Figures 10c - 10f.

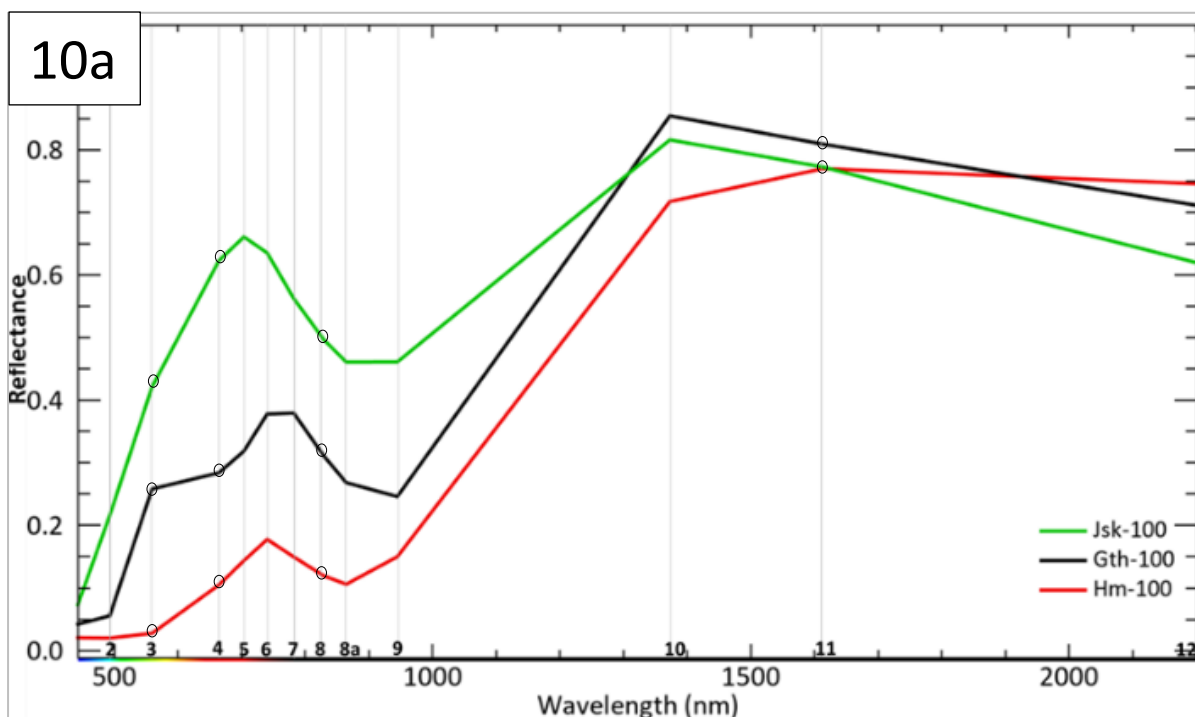


Figure 10a Resampled spectra of the minerals and the corresponding band's position denoted by small circles that were used in the ratio (B11/B8) against (B4/B3).

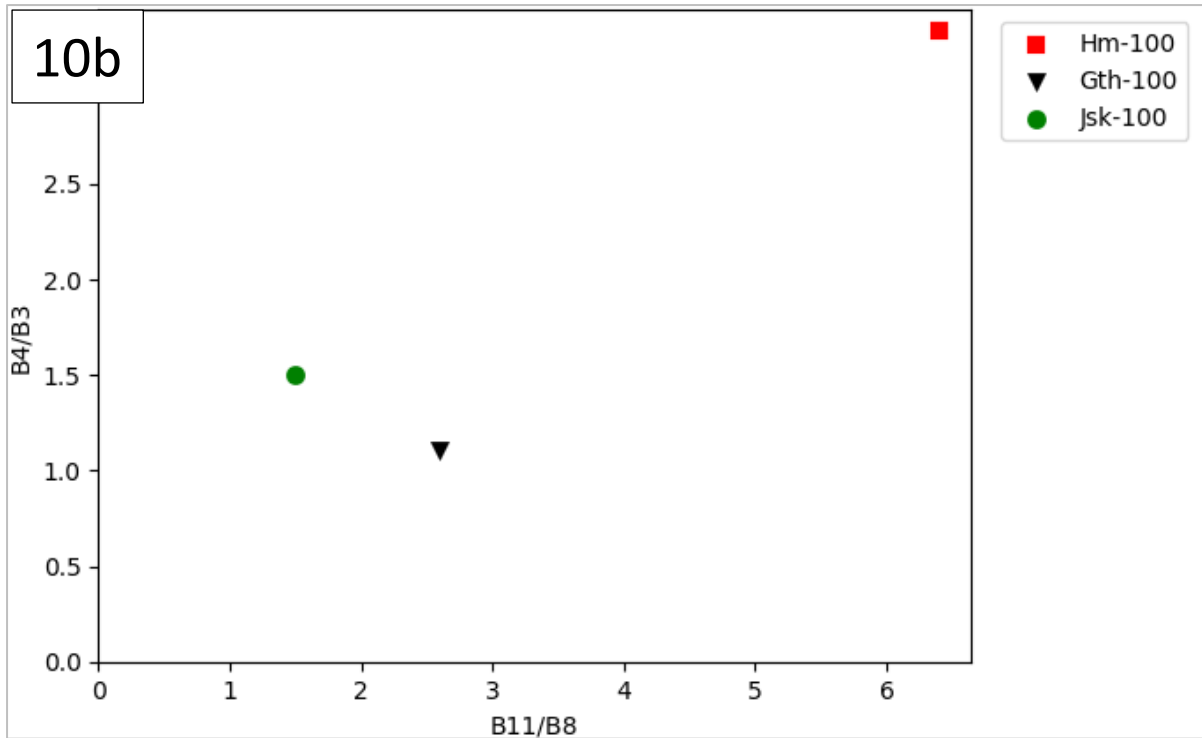


Figure 10b Scatterplots of (B_{11}/B_8) vs. (B_4/B_3) for the pure iron minerals with the supported triangular trend illustrating the relationship between pure iron minerals.

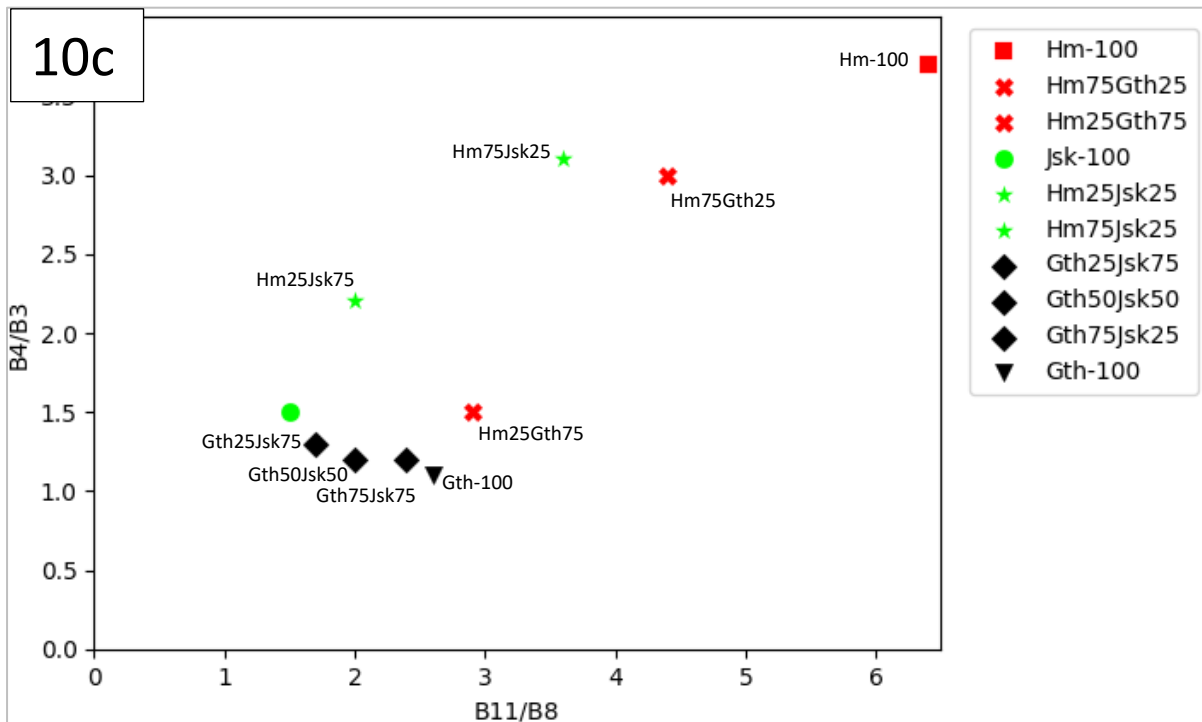


Figure 10c Supported triangular trend illustrates the relationship between iron minerals and their varying compositions.

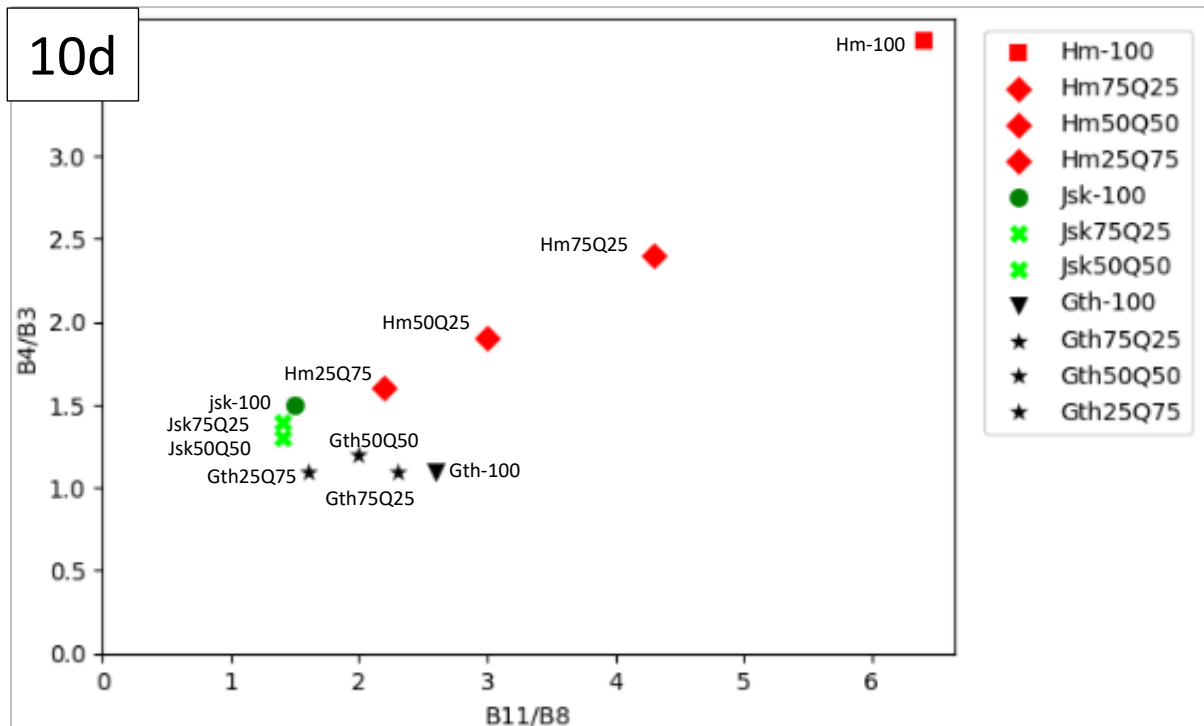


Figure 10d Iron minerals mixtures with quartz show hematite assigned high scores, jarosite intermediate scores, and goethite low scores by B4/B3. Goethite is assigned an indistinct score by B11/B8, some scores of goethite overlap with both jarosite and h

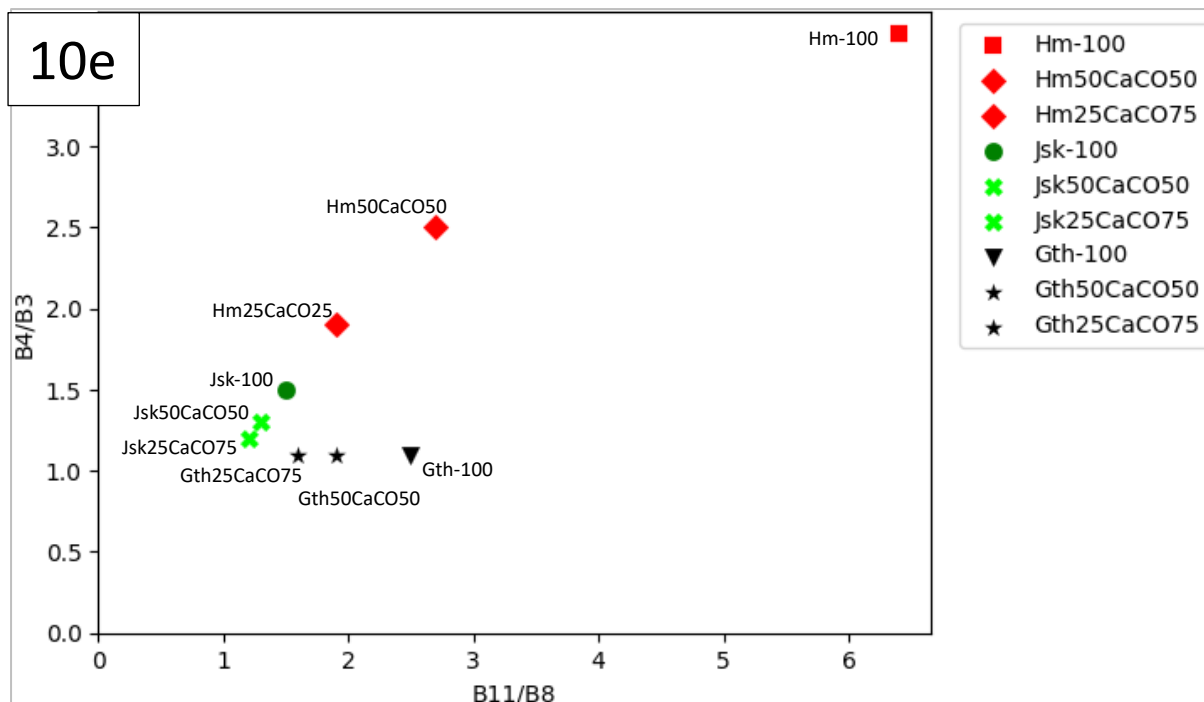


Figure 10e Depicts a linear relationship between hematite and jarosite by B4/B3, with both ratios assigning distinct values to each; however, goethite appears to have indistinct scores by B11/B8.

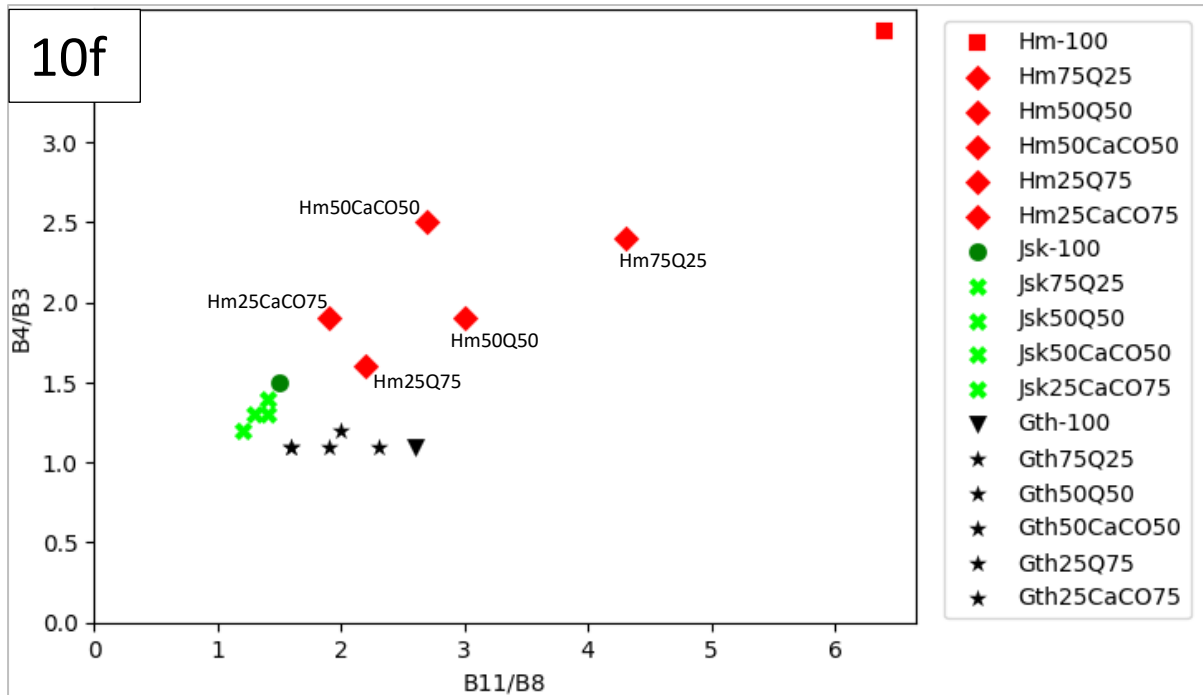


Figure 10e Scatterplots of (B11/B8) vs. (B4/B3) show iron minerals assigned distinct scores, with hematite mineral mixtures receiving a high score from both ratios, while goethite mixtures gaining an intermediate score from B11/B8 and a low score from (B

Scatterplot of $(B4/B2) \times (B4+B11)/B8$ vs $(B4/B3)$

This band ratio was first investigated for pure iron minerals, and the relationship suggested a nonlinear distribution. Mixtures of iron minerals were then tested, followed by mixtures of quartz and calcite. In Figure 11a, the resampled mineral spectra are illustrated with the specific band positions used in the ratio $(B4/B2) \times (B4+B11)/B8$ against $(B4/B3)$, marked by small circles. The scatterplot shown in Figure 11b does not reveal any discernible trend for the iron mineral compositions. Moreover, Figure 11c presents a scatterplot where iron minerals are indistinctly scored by the $(B4/B2) \times (B4+B11)/B8$ ratio, while a distinct differentiation is made by the $(B4/B3)$ ratio. Similarly, Figure 11d supports the previous observation with the $(B4/B3)$ ratio distinctly scoring the minerals in contrast to the $(B4/B2) \times (B4+B11)/B8$ ratio. Conclusively, Figure 11e displays a scatterplot for the iron minerals that highlights a nonlinear relationship between the two ratios. Additionally, the typical supported triangular trend is found ineffective for these specific iron mineral mixtures.

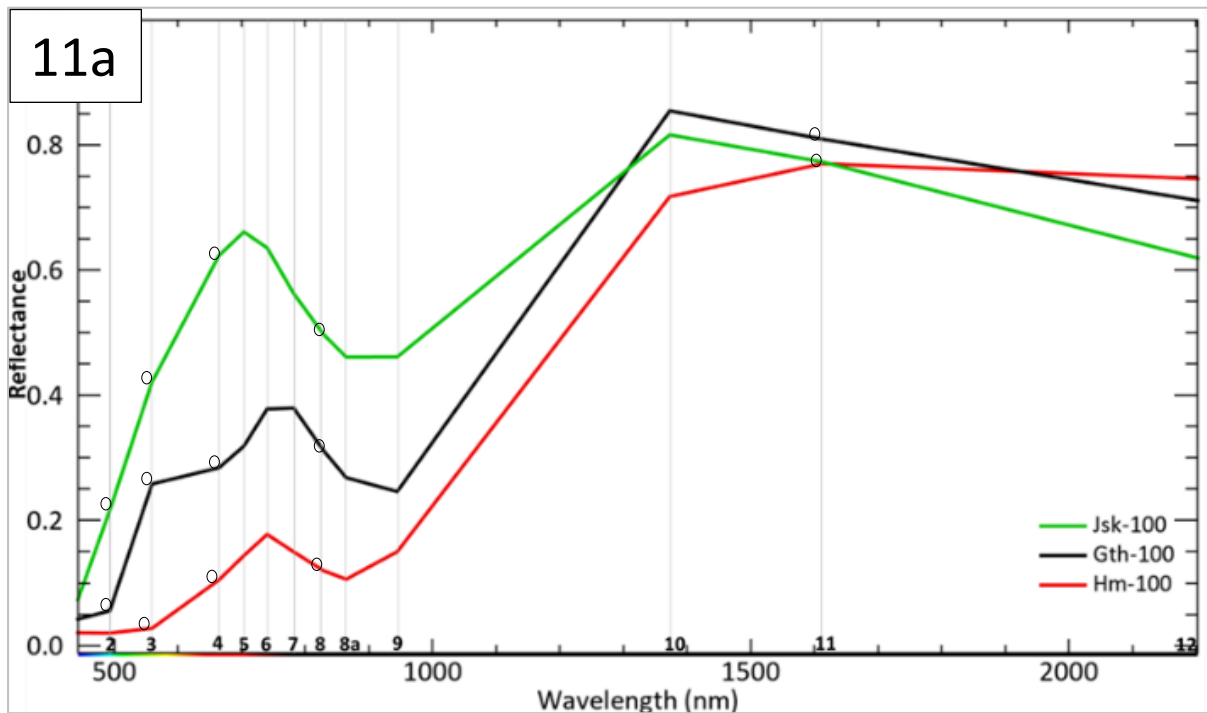


Figure 11a Resampled spectra of the minerals and the corresponding band's position denoted by small circles that were used in the ratio $(B4/B2) \times (B4+B11)/B8$ against $(B4/B3)$.

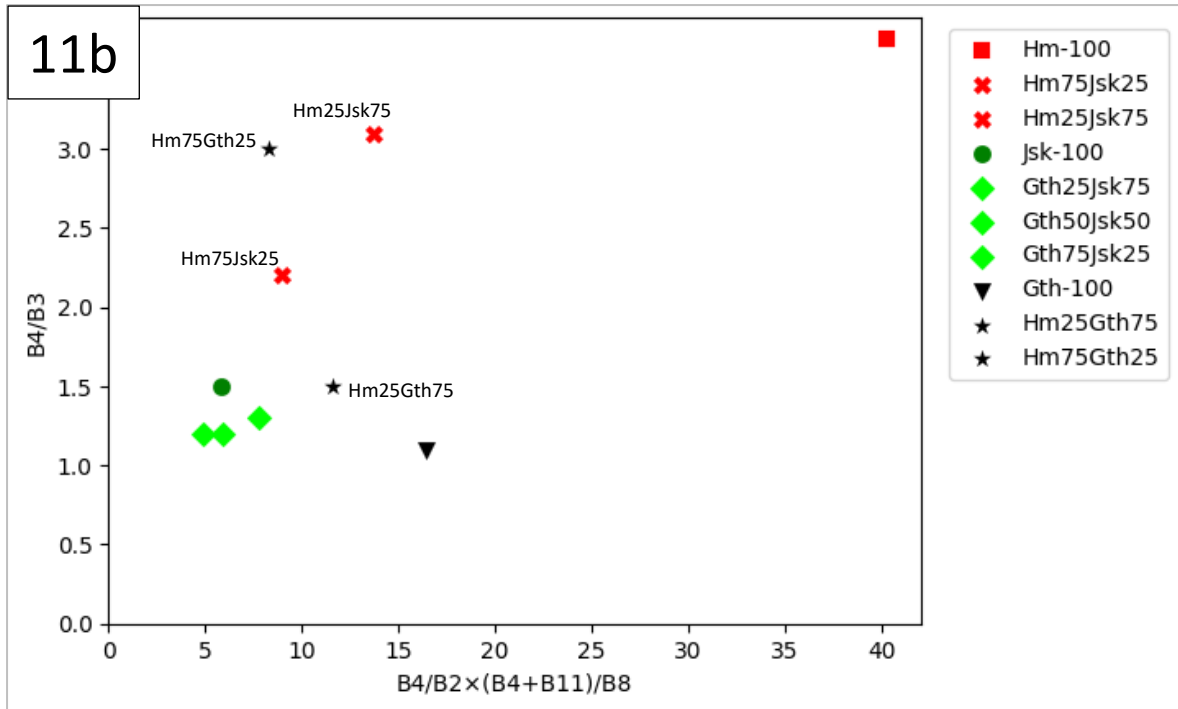


Figure 11b Scatterplot shows no preferred trend by the points of iron minerals composition.

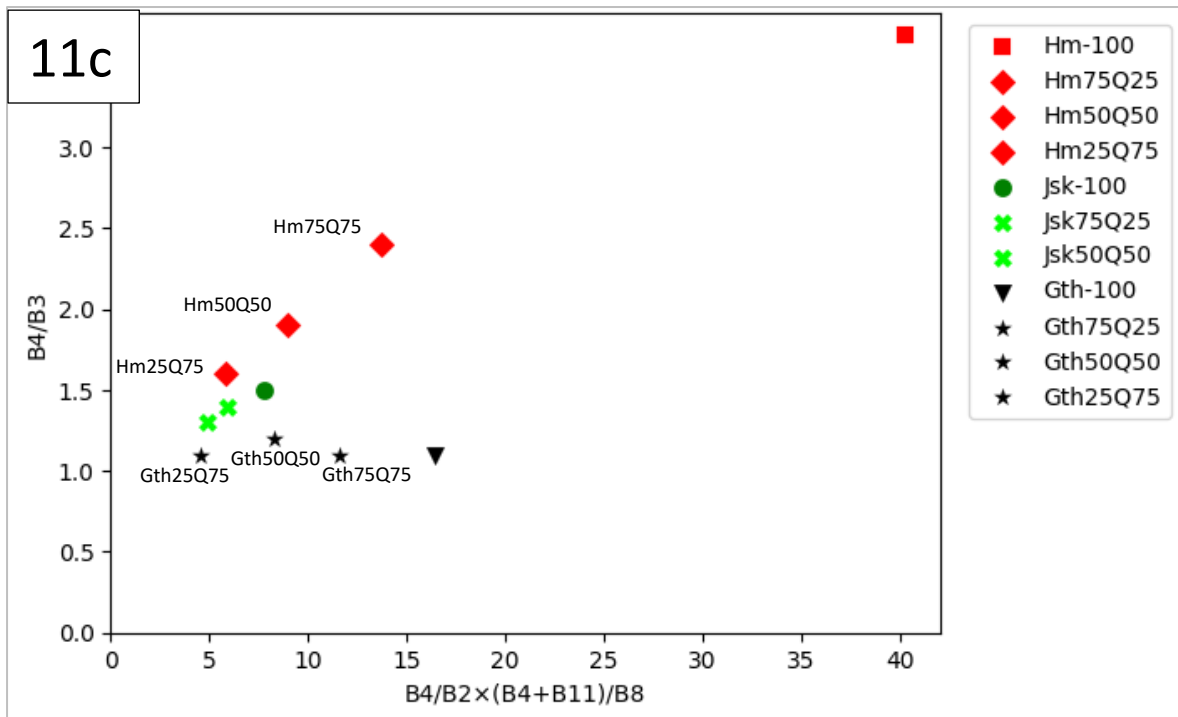


Figure 11c Scatterplot show iron minerals assigned indistinct scores by $(B4/B2) \times (B4+B11)/B8$, while $(B4/B3)$ assigned distinct scores to the minerals.

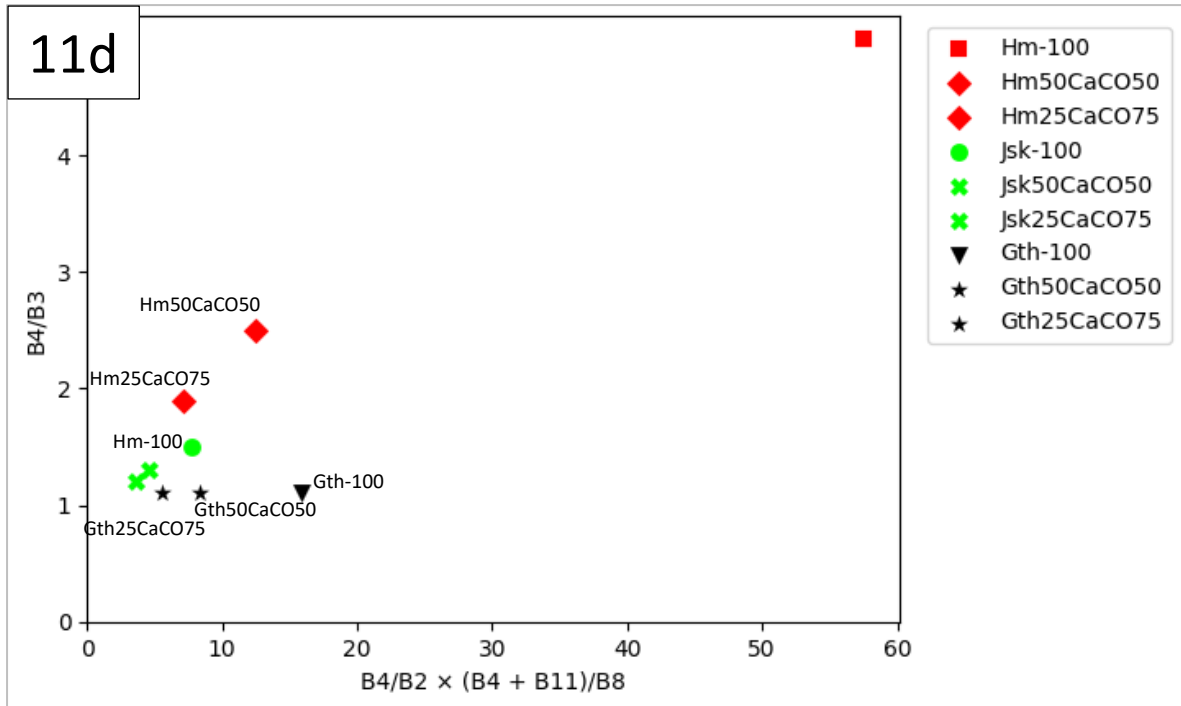


Figure 11d Scatterplot shows the iron minerals are assigned indistinct scores by $(B4/B2) \times (B4+B11)/B8$, whereas the $(B4/B3)$ ratio assigned distinct scores to the minerals.

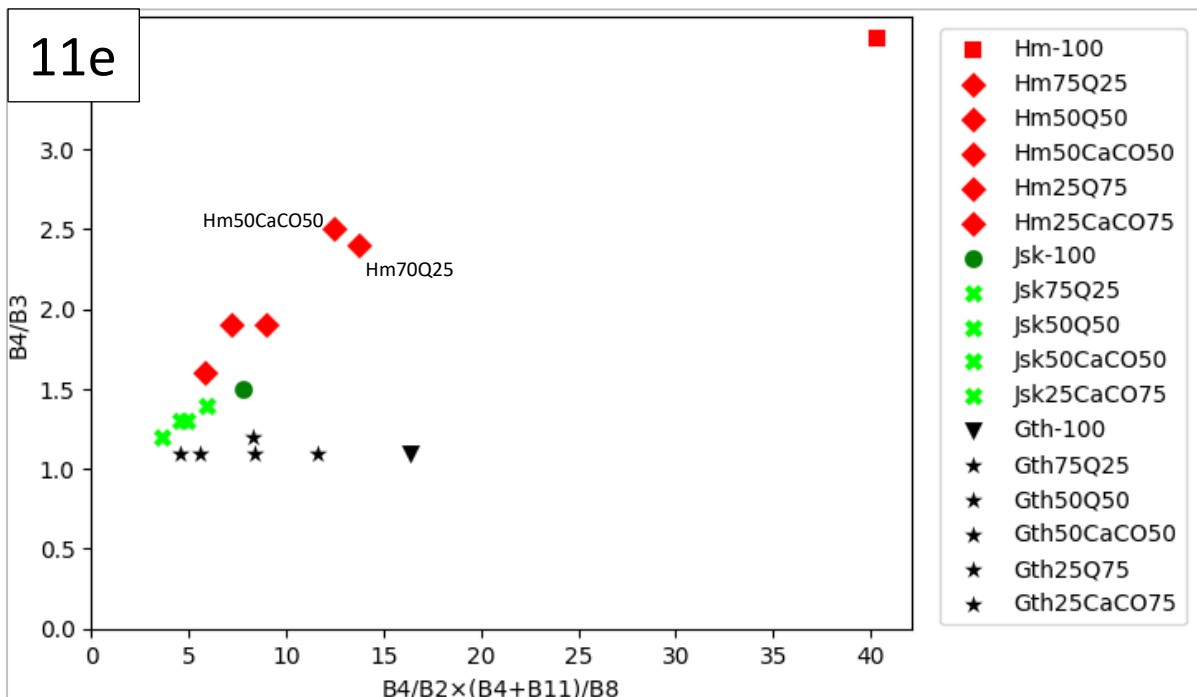


Figure 11e Scatterplots of $(B4/B2) \times (B4+B11)/B8$ vs $(B4/B3)$ for the iron minerals show a nonlinear relationship, and the supported triangle trend does not work between the mixtures of iron minerals.

Scatterplot of $(B4/B2) \times (B4+B11)/B8$ vs $(B12/B8) + (B3/B4)$

This section presents the result from evaluating the band ratios $(B4/B2) \times (B4+B11)/B8$ and $(B12/B8) + (B3/B4)$. Figure 12b displays a scatterplot with a linear trend, uniquely scoring each pure iron mineral. In contrast, Figure 12c scatterplot reveals ambiguous scores assigned by the ratios, and a clear triangular trend for mineral composition is absent. Furthermore, Figure 12d shows the scatterplot suggests a trend aligned with mineral composition, yet the ratios assigned indistinct scores to the minerals. Figure 12e scatterplot shows a linear correlation, but the mixtures of iron minerals are assigned indistinct scores. Lastly, Figure 12f illustrates scatterplots for all iron mineral mixtures, and they, too, assigned indistinct scores when evaluated by the ratios.

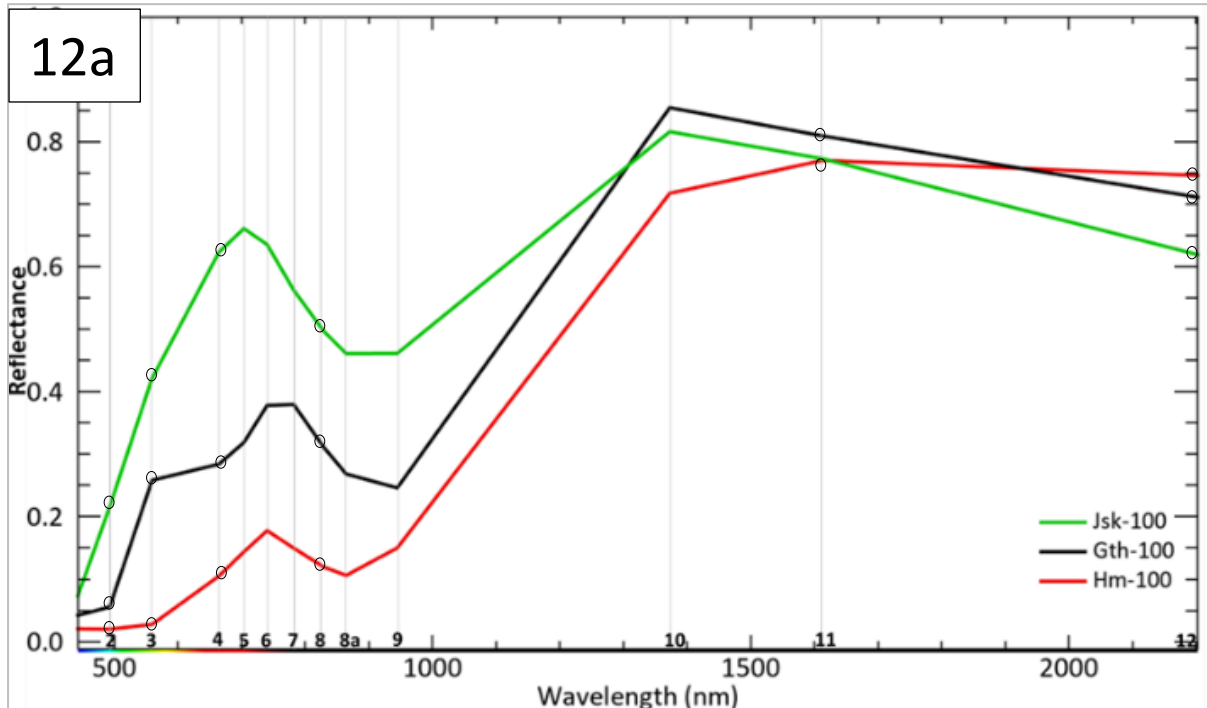


Figure 12a The resampled spectra of the minerals and the corresponding band's position, denoted by small circles, that were used in the ratio $(B4/B2) \times (B4+B11)/B8$ vs $(B12/B8) + (B3/B4)$.

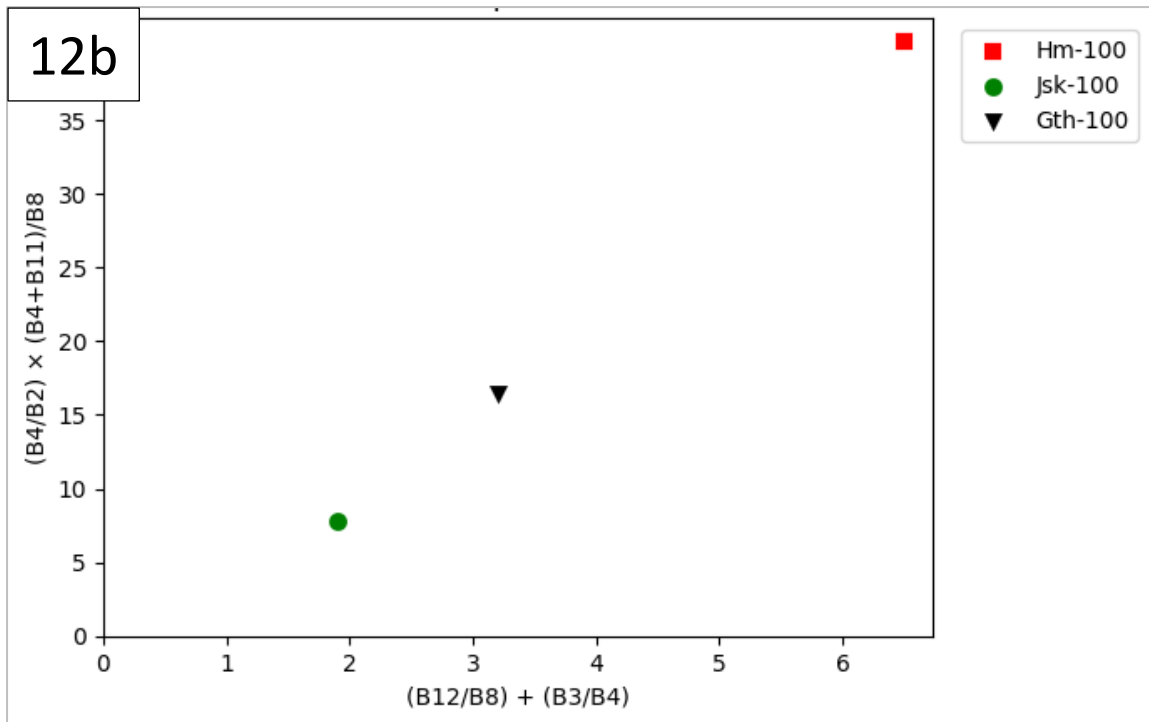


Figure 12b Scatterplot shows a linear trend by the points of pure iron minerals assigning each mineral a distinct score.

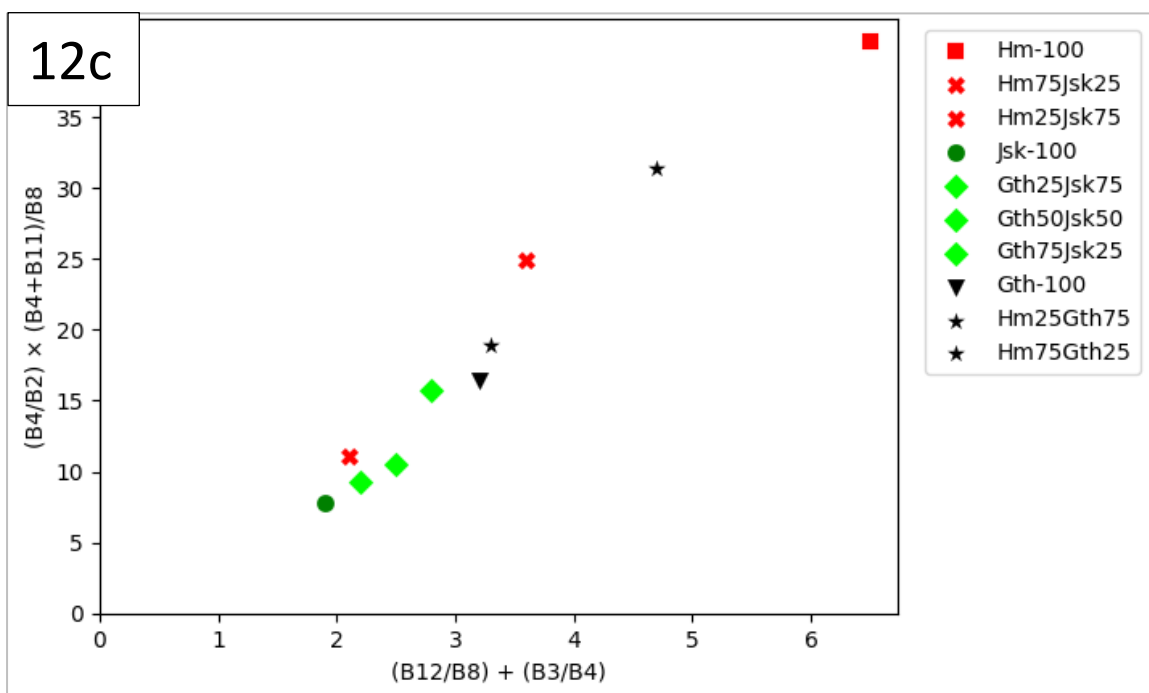


Figure 12c Scatterplot show iron minerals assigned indistinct scores by $(B4/B2) \times (B4+B11)/B8$ vs $(B12/B8) + (B3/B4)$, no supported triangle trend for mineral composition.

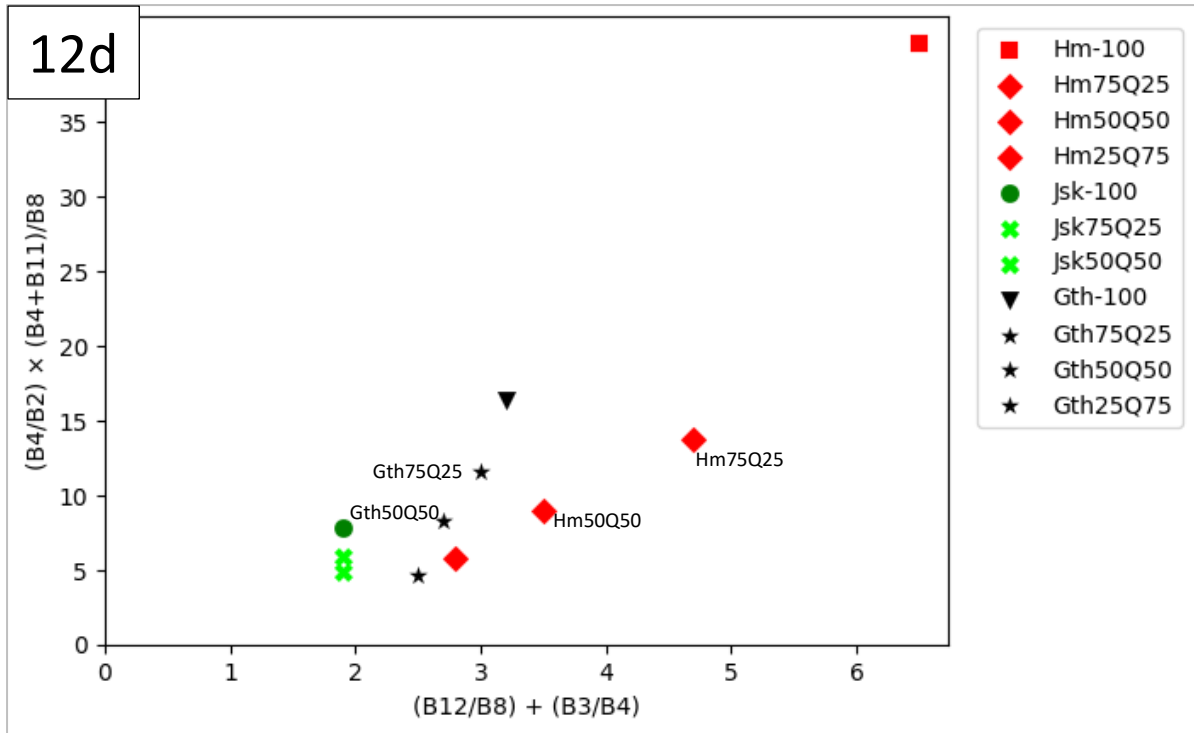


Figure 12d Scatterplot shows the iron minerals are assigned indistinct scores by $(B4/B2) \times (B4+B11)/B8$ vs $(B12/B8) + (B3/B4)$. Trend follows composition, but the ratios assigned indistinct scores.

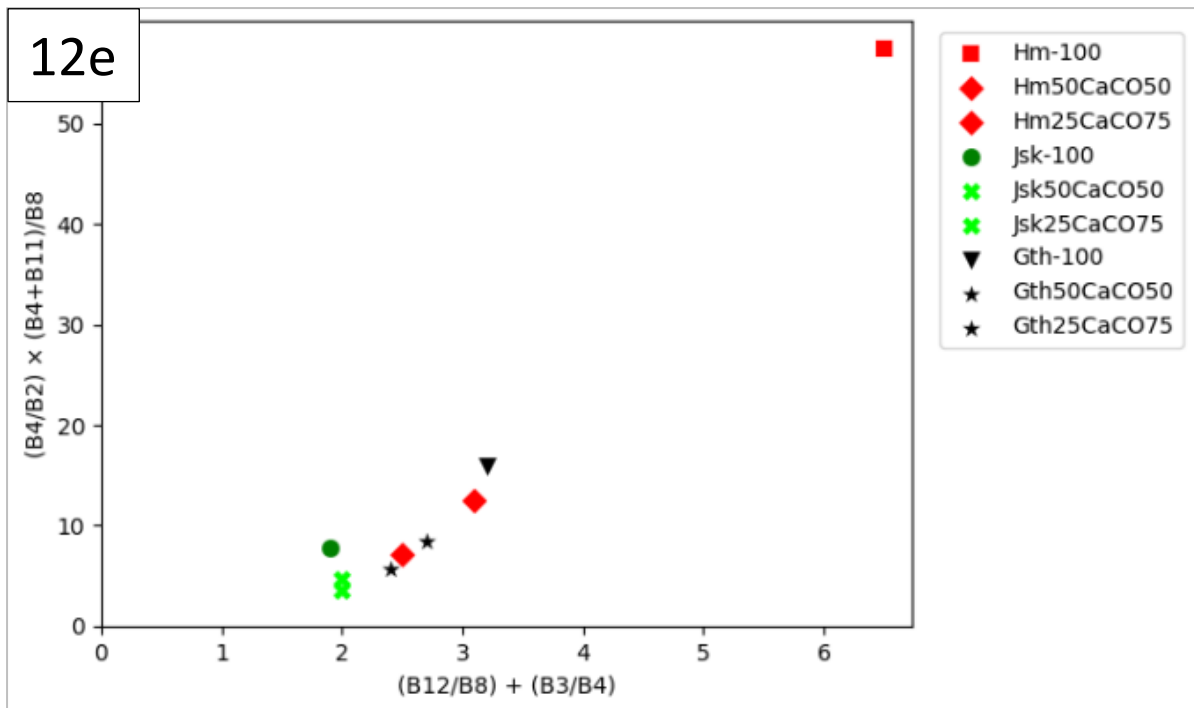


Figure 12e Scatterplots of $(B4/B2) \times (B4+B11)/B8$ vs $(B12/B8) + (B3/B4)$ show a linear relationship, and the supported triangle trend does not work between the mixtures of iron minerals.

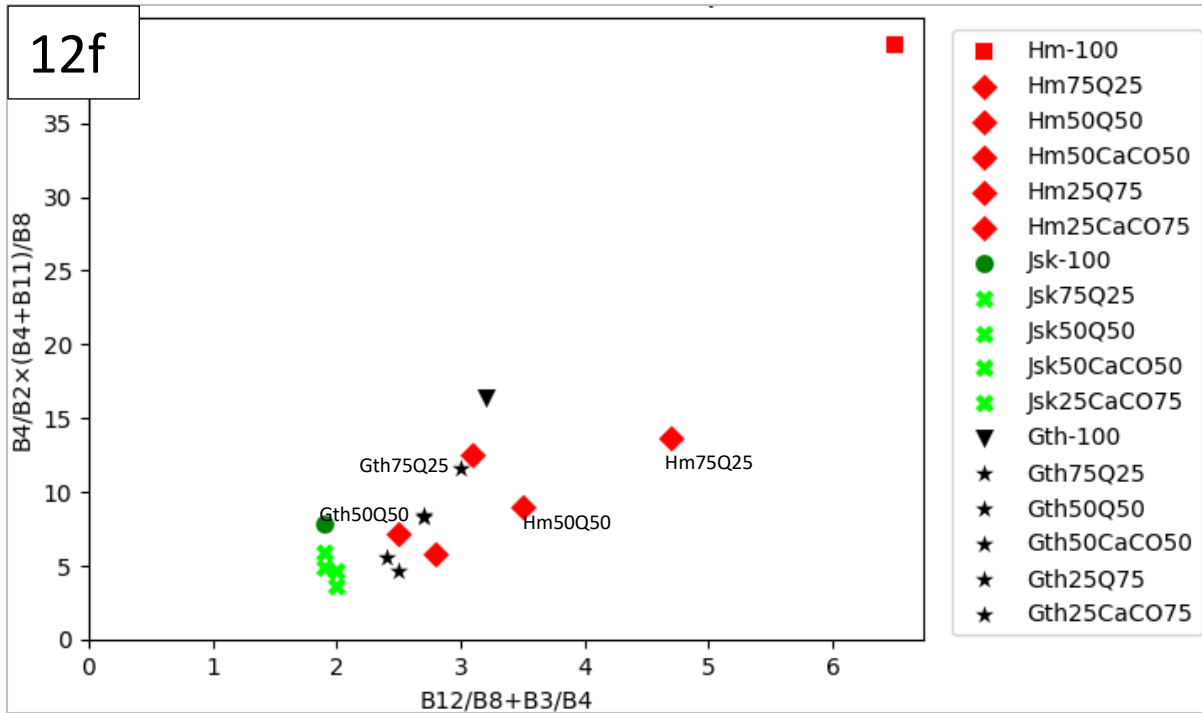


Figure 12f Scatterplots of all iron minerals with mixtures are assigned indistinct scores by $(B4/B2) \times (B4+B11)/B8$ vs $(B12/B8) + (B3/B4)$.

This assessment was conducted on all the existing band ratios, and the outcome shows that only $(B4/B3)$ adequately assigned distinct scores, thereby discriminating between the minerals. This is summarized in Table 9 below, and the analysis is available in Appendix.

Table 9 Summary of the findings from the analysis of band ratios for discriminating between the iron minerals.

	Existing band ratios plot against each other		Performance on Fe-minerals
1	B11/B8	B4/B2	indistinguishable
2	B11/B8	B4/B3	Distinguishes hematite
3	B11/B8	B12/B11	indistinguishable
4	B11/B8	$(B4+B11)/B8a$	indistinguishable
5	$(B3+11)/(B4+B8)$	$(B4+B11)/B8a$	indistinguishable
6	$(B12/B8) + (B3/B4)$	$(B4+B11)/B8a$	indistinguishable
7	$(B12/B8) + (B3/B4)$	$(B4/B2) \times (B4+B11)/B8$	indistinguishable
8	B4/B2	B4/B3	indistinguishable
9	$(B4/B2) \times (B4+B11)/B8$	B4/B2	indistinguishable
10	$(B4/B2) \times (B4+B11)/B8$	B4/B3	indistinguishable
11	$(B4/B2) \times (B4+B11)/B8$	B11/B8	indistinguishable

3.4 Experimenting with new band ratios

This section shows the results of experimenting with new band ratios that can assign distinct scores to the minerals. This is a result of the outcome from the results of the analysis of the existing band ratios in Table 3 from section 3.3.4, which demonstrates that only hematite was assigned distinct scores by the (B4/B3) band ratio. In contrast, jarosite and goethite minerals appeared to have indistinct scores, as illustrated in Figure 10f. Therefore, further analysis of the band ratio is required to distinguish the other iron minerals. Firstly, Table 10 shows the result from the examination of the relationships between S2 bands and spectral features of iron minerals. Consequently, the analysis shown in Table 10 guided the choice of band ratios that were experimented on the iron minerals. Furthermore, in this study, a scoring system was employed to evaluate the new band ratios in discriminating specific iron minerals. The scoring ranged from High (indicating distinctively high scores in comparison to the other minerals), Intermediate (distinctively in-between scores), and Low (distinctively low scores).

Table 10 Displays relationships between bands and spectral features of iron-bearing minerals.

Relationship between bands and spectral features			
Bands	Jarosite	Goethite	Hematite
B2	Absorption	Absorption	Absorption
B3	Absorption	Peak	Absorption
B4	Peak	Absorption	Absorption
B5	Peak	Absorption	Absorption
B6	Peak	Peak	Peak
B7	Absorption	Peak	Shallow absorption
B8	Absorption	Absorption	Absorption
B8A	Absorption	Absorption	Absorption
B9	Absorption	Absorption	Shallow absorption
B11	Peak	Peak	Peak
B12	Absorption	Peak	Peak

Table 11 provides a summarized overview of the experimental results obtained from the newly developed band ratios. As these are summarized results, detailed discussions and further elaborations related to the experiments will be presented in Figures 13-15 in the subsequent sections of the study. The objective of this summary shown in Table 11 below is to provide an initial understanding of the results and interpretation of the experiments. Various techniques, including simple band ratio, the combination of band ratios, and the relative absorption band depth approach, have been utilized in this study. For the simple band ratio technique using the (B3/B2) band ratio, it was experimented for differentiating goethite, utilizing data from Table 10. The results showed goethite receiving distinct scores, while jarosite and hematite were assigned low scores (as shown in Figure 13). Moreover, the ratio (B3/B4) was tested, but its performance was inadequate in terms of assigning distinct scores to the minerals (as shown in Figure 13). Similar performances were encountered with (B7/B9), which assigned indistinct scores to the minerals. Nevertheless, when these two ratios were combined to form (B3/B4)+(B7/B9), the ability to assign distinct scores to the minerals improved, as shown in Figure 13.

Subsequently, the (B5/B12) ratio was investigated for its potential to identify jarosite and differentiate between the minerals. However, this ratio did not perform well (as shown in the Appendix 1-2). To overcome this, the (B5+B11)/B12 band ratio was derived using the Relative Absorption Band Depth approach as illustrated by Figure 2, section 2.3.4) to enhance the discrimination between the minerals and identification of jarosite. The scatterplot depicted in Figure 14 shows that this ratio successfully assigned distinct scores to the minerals. Therefore, using the band ratio (B5+B11)/B12, jarosite received a high

Discrimination of individual Iron-bearing minerals with the Sentinel-2 Super-Spectral Imager

score, goethite an intermediate score, and hematite a low score. This analysis presents promising results for the novel band ratios in identifying and discriminating iron-bearing minerals. Detailed analyses and discussions of these results will be elaborated upon in the figures in the following sections.

Table 11 Summary of novel band ratios performances on discriminating the iron-bearing minerals

Techniques and performance of the band ratio						
Technique		Simple Band Ratio		Band Ratios Combination		Relative Absorption Band Depth
Band ratio		B3/B2	B5/B12	(B3/B2)+(B7/B9)	(B3/B4)+(B7/B9)	(B5+B11)/B12
Band ratio scores	High	Jarosite	Jarosite	Goethite	Goethite	Jarosite
	Intermediate	Goethite	Goethite	Jarosite	Jarosite	Goethite
	Low	Hematite	Hematite	Hematite	Hematite	Hematite

Scatterplots of (B3/B2) vs (B3/B2)+(B7/B9)

This section shows the result from the experiment conducted for the band ratio (B3/B2) vs (B3/B2)+(B7/B9). The result showed a linear trend and correlation, uniquely scoring each pure iron mineral. Goethite received distinct high scores, while jarosite intermediate and hematite were assigned low scores. However, some points appeared to overlap when the mixtures were added (Figure 13c), especially between jarosite and hematite. These band ratios are correlated, assigning distinct scores to varied mineral compositions. The correlation is a direct relationship, meaning that as (B3/B2) changes, (B3/B2)+(B7/B9) changes; therefore, there is a consistent change in the band ratios.

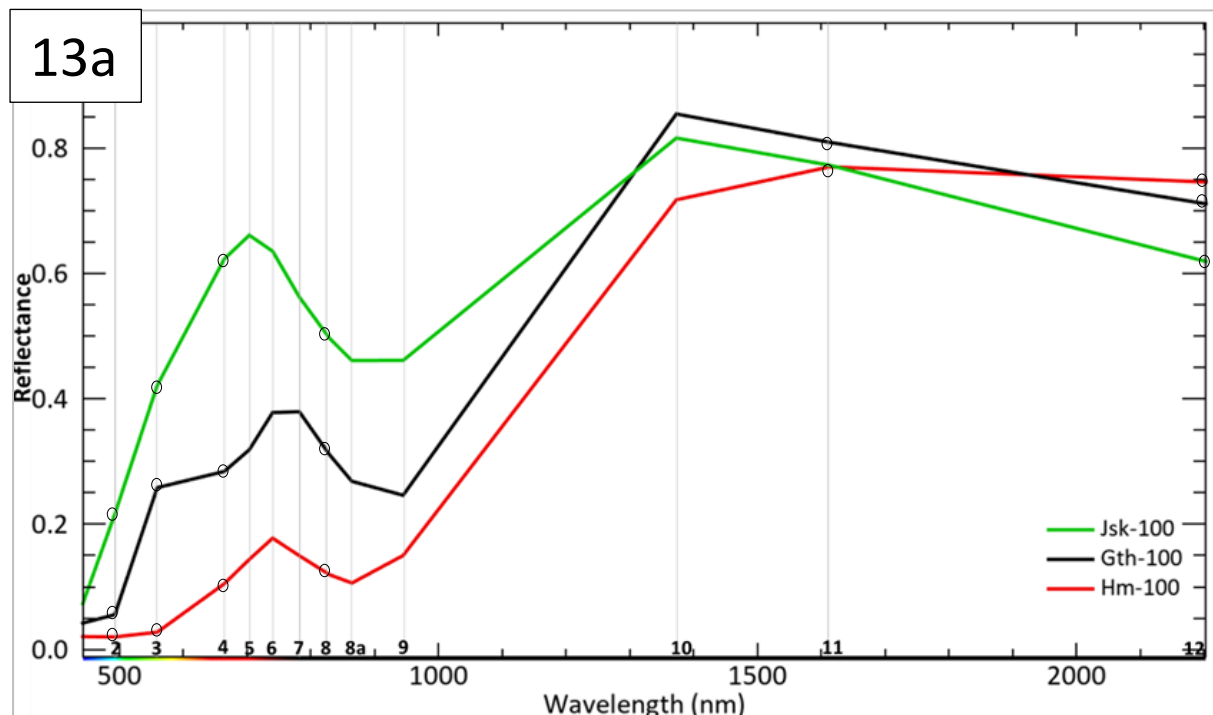


Figure 13a The resampled spectra of the minerals and the corresponding band's position, denoted by small circles, that were used in the ratio $(B4/B2) \times (B4+B11)/B8$ vs $(B12/B8) + (B3/B4)$.

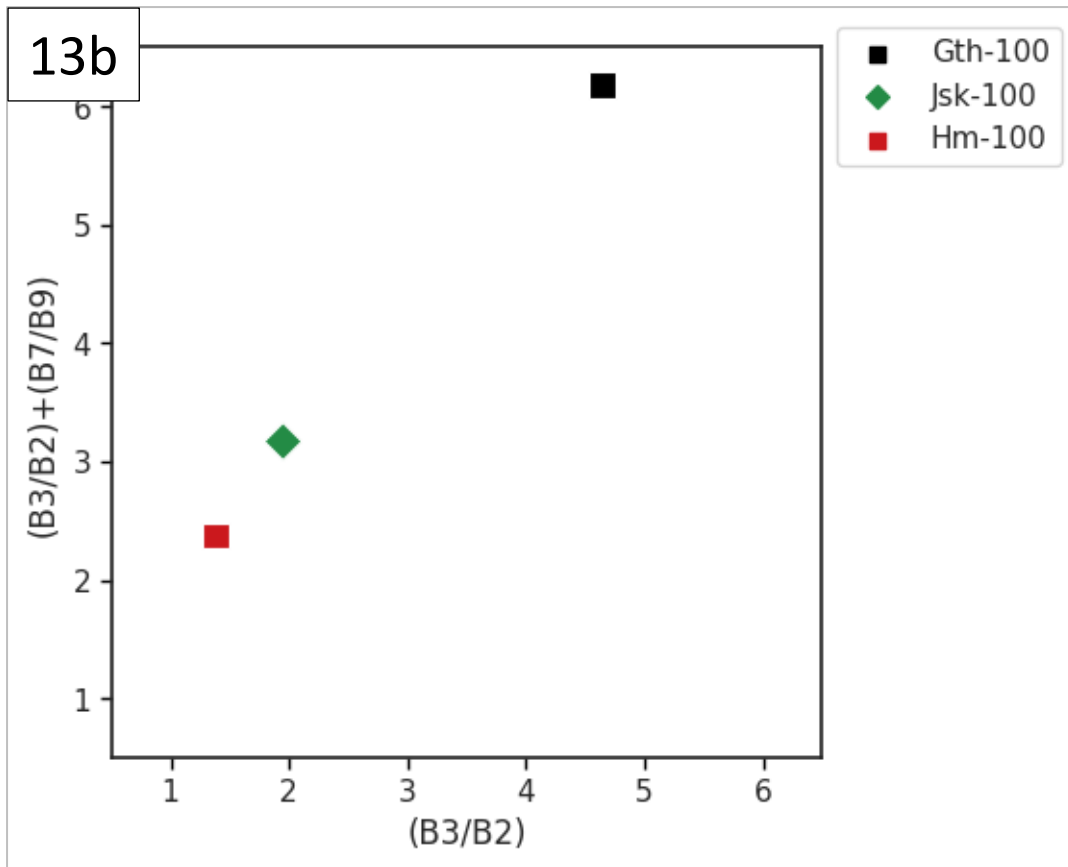


Figure 13b Band ratios show a linear trend and correlation, uniquely scoring each pure iron mineral.

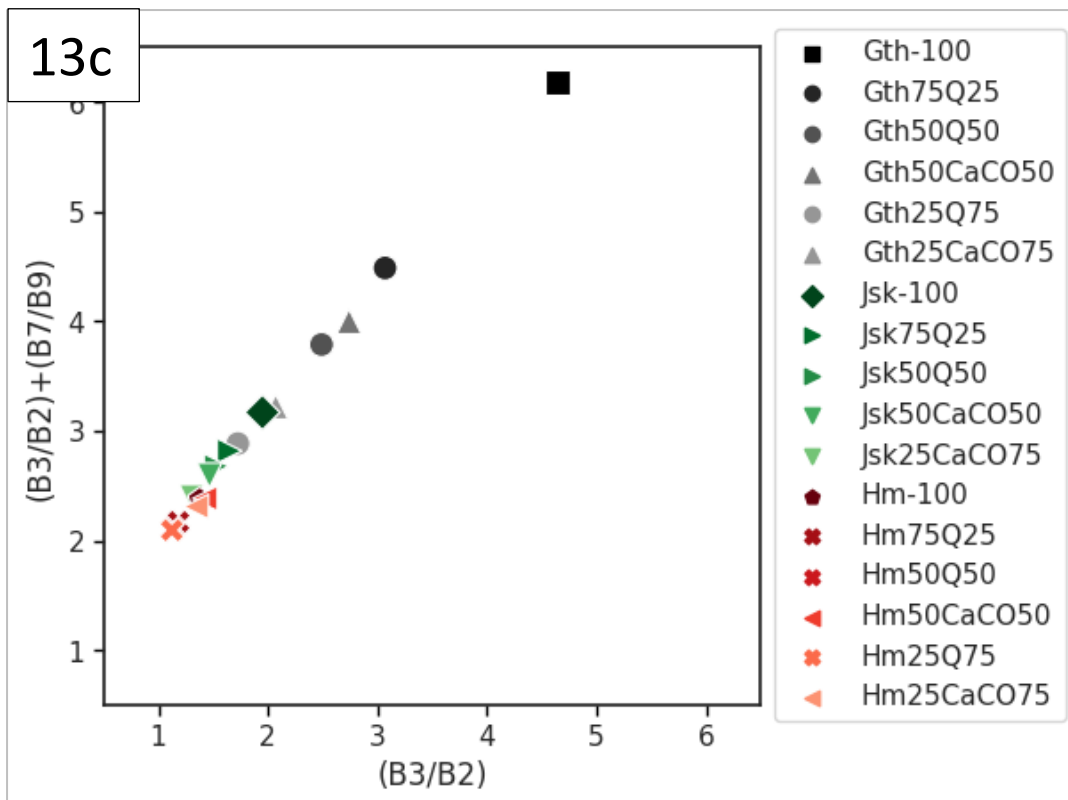


Figure 13c shows band ratios are correlated, assigning distinct scores to varied mineral compositions.

Scatterplots of $(B3/B4)+(B7/B9)$ vs $(B5+B11)/B12$

This section presents the result from experimenting with the band ratios $(B3/B4)+(B7/B9)$ vs. $(B5+B11)/B12$ aimed at discriminating goethite and jarosite, respectively. The results showed jarosite receiving distinct high scores, while goethite and hematite were assigned intermediate and low scores by $(B5+B11)/B12$ ratio, respectively as shown in Figure 14; in contrast, $(B3/B4)+(B7/B9)$ assigned goethite distinct high scores, jarosite intermediate and hematite low scores.

The observation from the scatterplots shows a clear supported triangle trend supporting varied mineral composition. A general nonlinear trend with the plots positioned in a triangular trend for the pure minerals is illustrated in Figure 14b. On the other hand, Figure 14c shows each mineral mixture appears to follow a linear trend, where the less iron mineral composition moves towards a central point, and higher amounts of iron minerals in the mixtures are closer to the pure iron mineral plot. Consequently, the band ratios appear to be correlated; as one band ratio changes, the other band ratio change. In some cases, the correlation is either positive or negative. For example, in Figure 14d, mixtures of hematite+jarosite and of hematite+goethite exhibit a positive correlation by the ratios, while for the mixtures of goethite+jarosite, a negative correlation is observed, one ratio increase, and the other decrease.

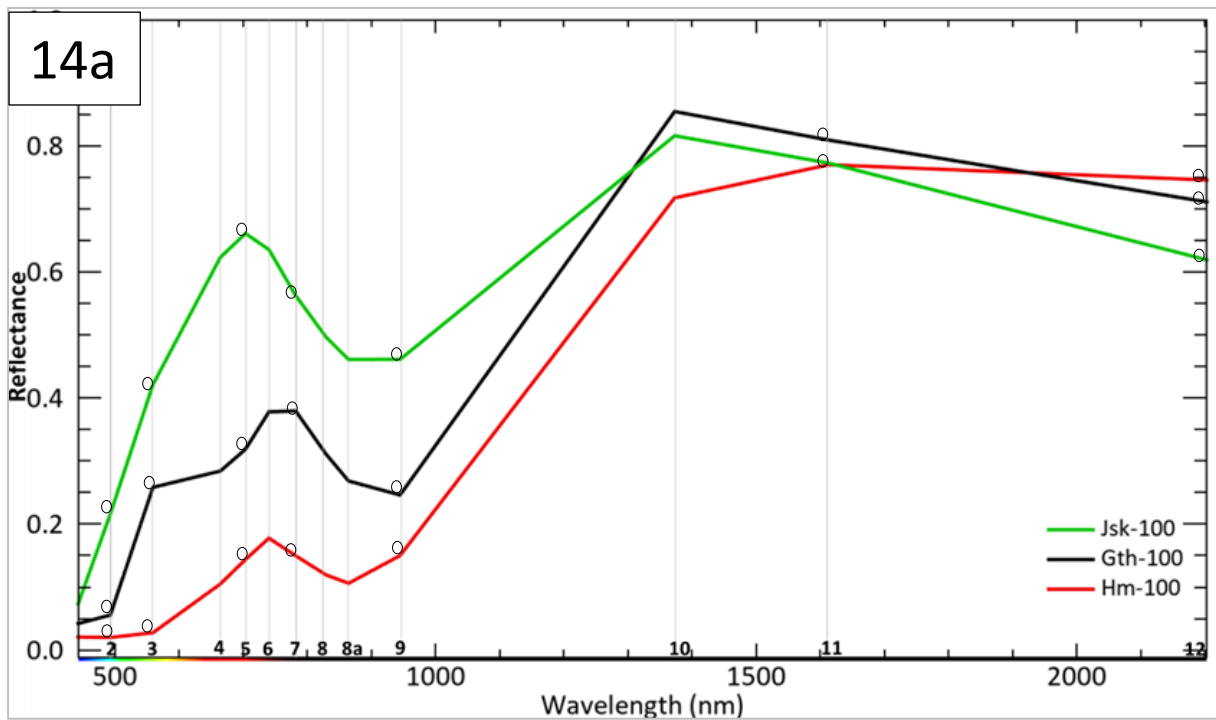


Figure 14a Resampled spectra of the minerals and the corresponding band's position denoted by small circles that were used in the ratio $(B3/B4)+(B7/B9)$ vs $(B5+B11)/B12$.

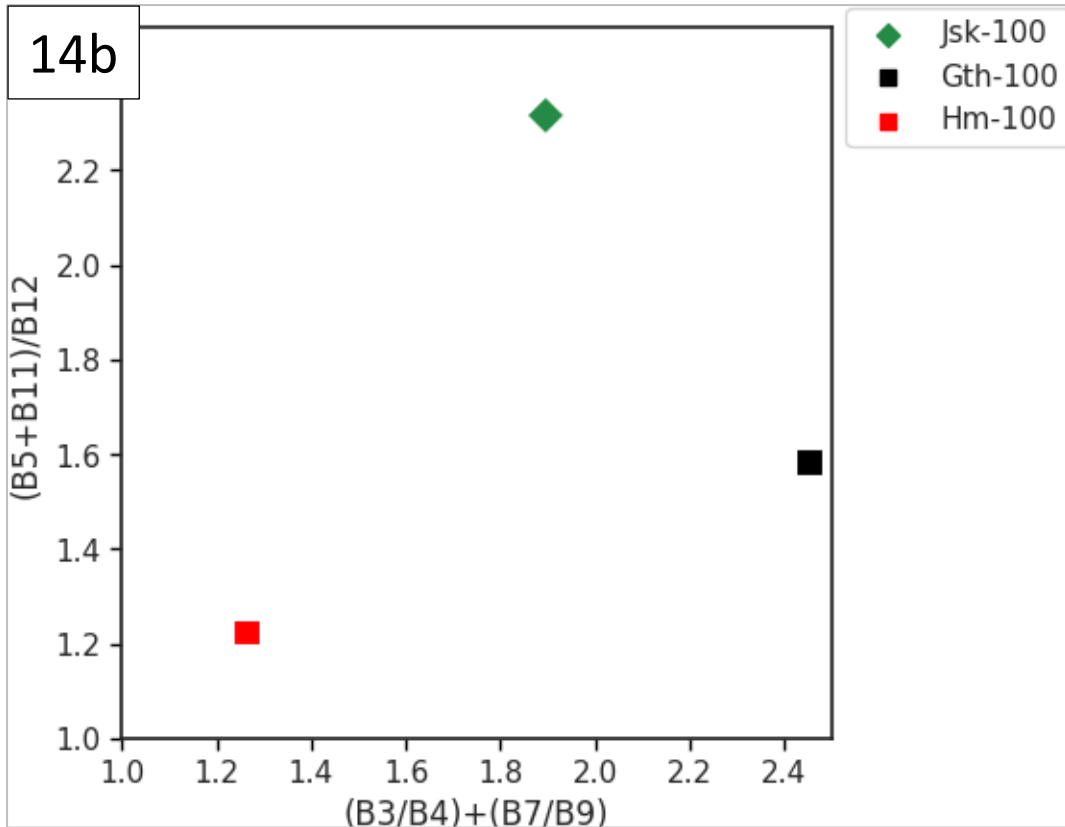


Figure 14b Scatterplot shows a nonlinear trend with plots positioned in a triangular trend. Each mineral is assigned distinct scores.

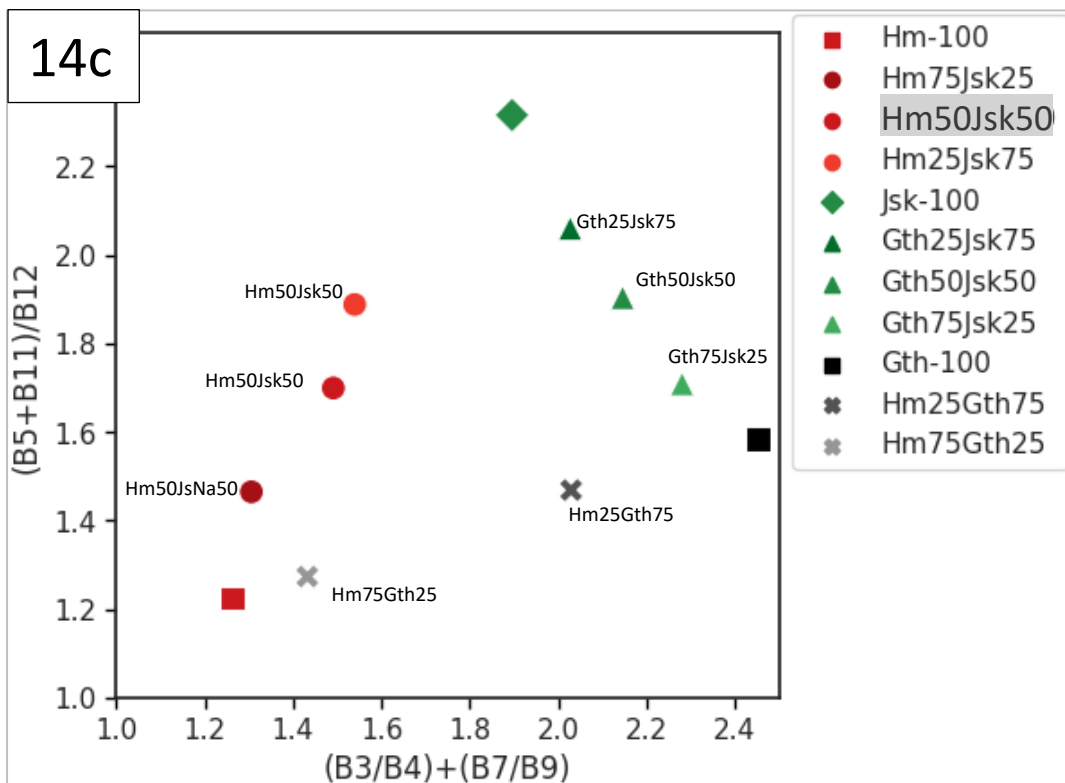


Figure 14c Scatterplot shows iron minerals mixtures assigned indistinct scores by $(B3/B4) \times (B7/B9)$ vs $(B5+B11)/B12$, depicting a supported triangle trend for varied mineral composition.

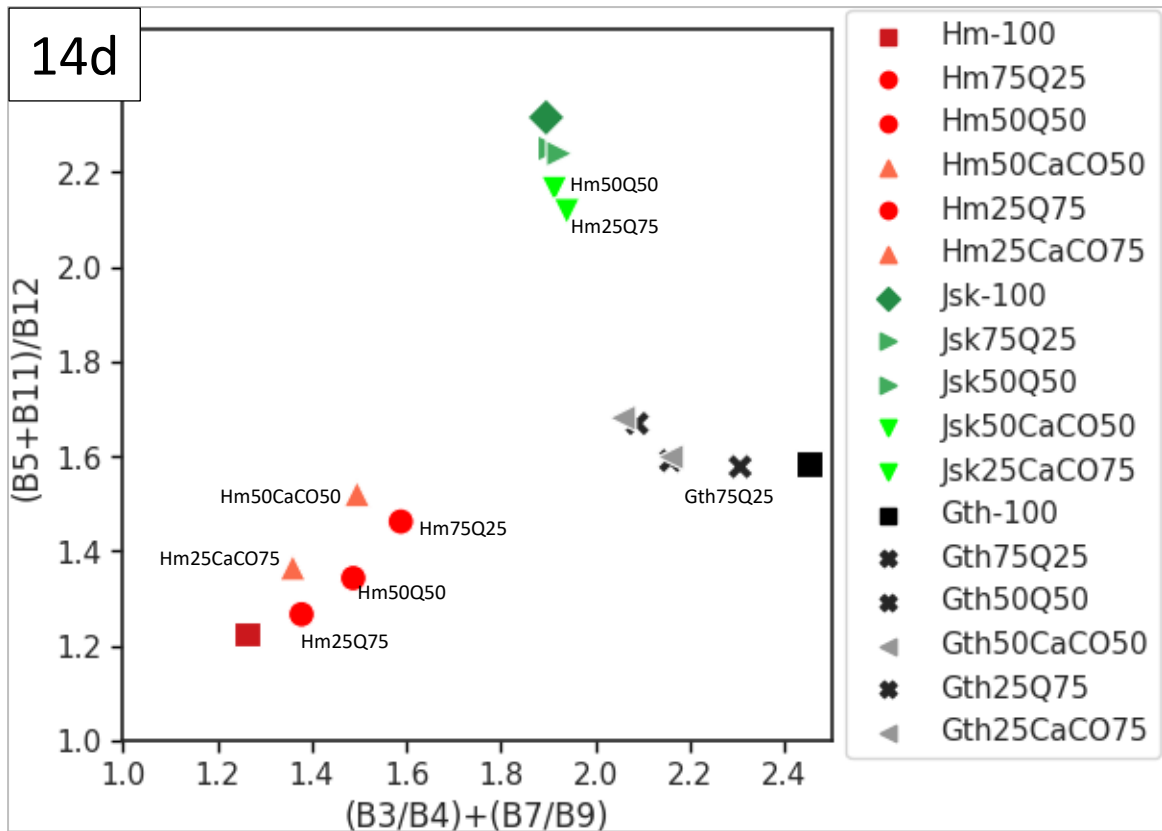


Figure 14d Scatterplot shows the iron minerals assigned distinct scores by $(B3/B4) \times (B7/B9)$ vs $(B5+B11)/B12$. The triangular trend depicts varied composition; however, the points move towards the center.

3.5 Evaluating the Novel Band Ratios

The preceding analyses and experiments within controlled environments have yielded novel band ratios that demonstrate the potential to discriminate between the various iron-bearing minerals. However, the actual applicability and effectiveness of these ratios in real-world settings remain a concern that this section seeks to address. The Cuprite area, known for its mineral diversity and complex geological characteristics, is selected as the reference location for this investigation. Therefore, the evaluation involves a detailed comparison of the novel band ratios with published reference data in a real-world geological context (Cuprite area). The accuracy or lack thereof of matching with reference data, the ability to identify specific minerals, and how applicable it is to real-world geological settings define success or failure. It is crucial to highlight an important distinction between the classifications adopted in this research and the reference data. The hyperspectral map referenced in this study is a “hard classification” approach. This method allocates each pixel in the dataset to a single class, indicating that the pixel belongs entirely to that class and no other. Conversely, this study employs a “soft classification” approach, where each pixel determines the probability or proportion of that pixel belonging to each class. Hence, instead of classifying a pixel into a specific class, a range of possibilities reflecting the mixed nature of real-world environments is given.

Two reference maps of the AVIRIS data from the Cuprite area were utilized. The first map highlights the dominant iron-bearing minerals within the 400 to 1300 nm electronic absorption wavelength range (Figure 3a). The second map showcases the primary clays, micas, sulfates, and carbonates in the 1.3- to 2.5- μm vibrational absorption wavelength range (Figure 3b).

3.5.1 Single-band Gray Image

Figure 15a shows a map in single-band gray created by the existing band ratio ($B4/B3$). The brightest pixel (i.e., highest value) highlighted hematite distribution in the area. This is observed in the central and the east part of the image. On the other hand, Figure 16a shows the map produced by ($B3/B2$), where the highlighted area in the southwestern part of the image was intended to discriminate goethite; however, in the image, the bright pixels highlight mixtures of iron minerals. This is according to the published map, which classified these areas as mixtures of iron minerals, as shown in Figure 16b. Finally, Figure 17a shows the map produced by $(B5+B11)/B12$, where it highlights the distribution of argillic alteration zones in the west and east of the image; however, this ratio was intended to discriminate jarosite.

Discrimination of individual Iron-bearing minerals with the Sentinel-2 Super-Spectral Imager

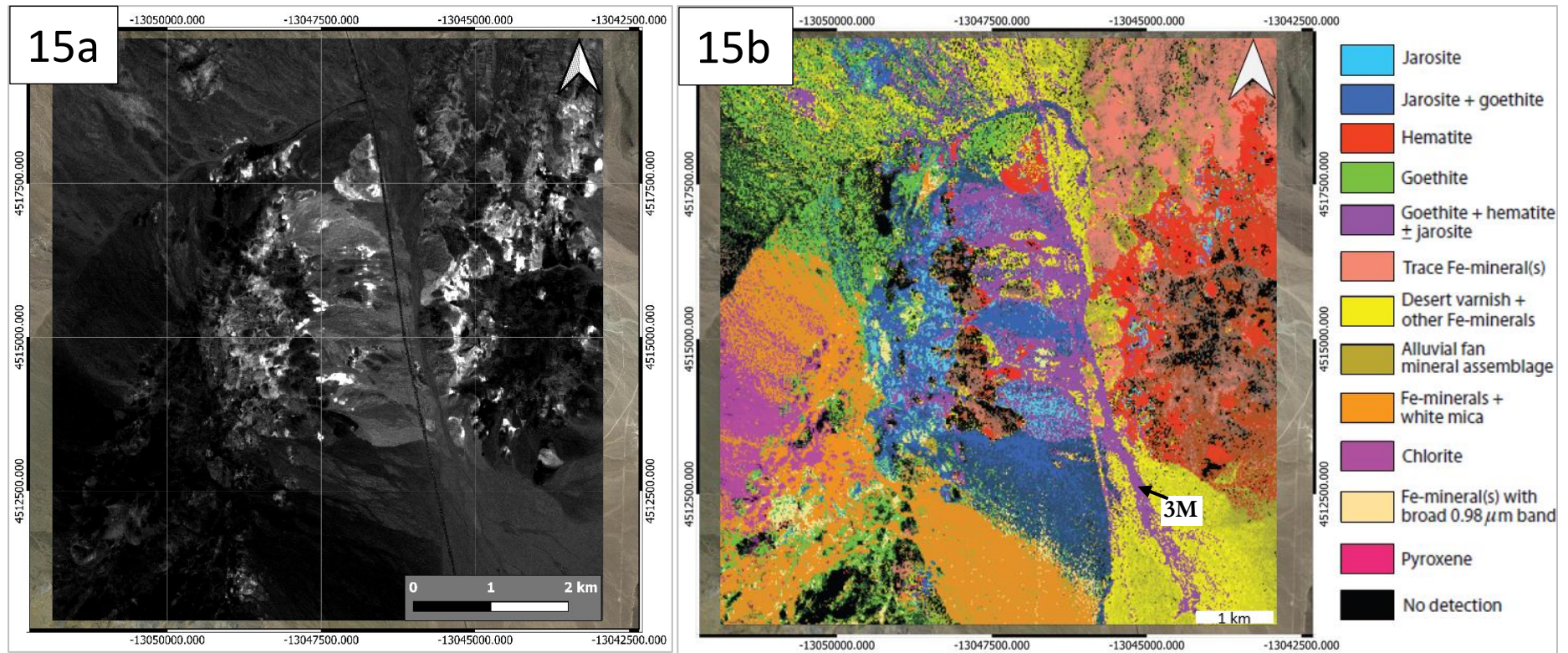


Figure 15a Single-band gray image generated by the band ratio (B4/B3) is shown here, with the highest value indicating the hematite distribution. Notably, hematite is highlighted in the central part of the map and to the east. 15b Mineral map utilizing the 400- 1300 nm electronic absorption band of the AVIRIS data, showing the spectrally dominant Iron-bearing minerals at Cuprite.

Discrimination of individual Iron-bearing minerals with the Sentinel-2 Super-Spectral Imager

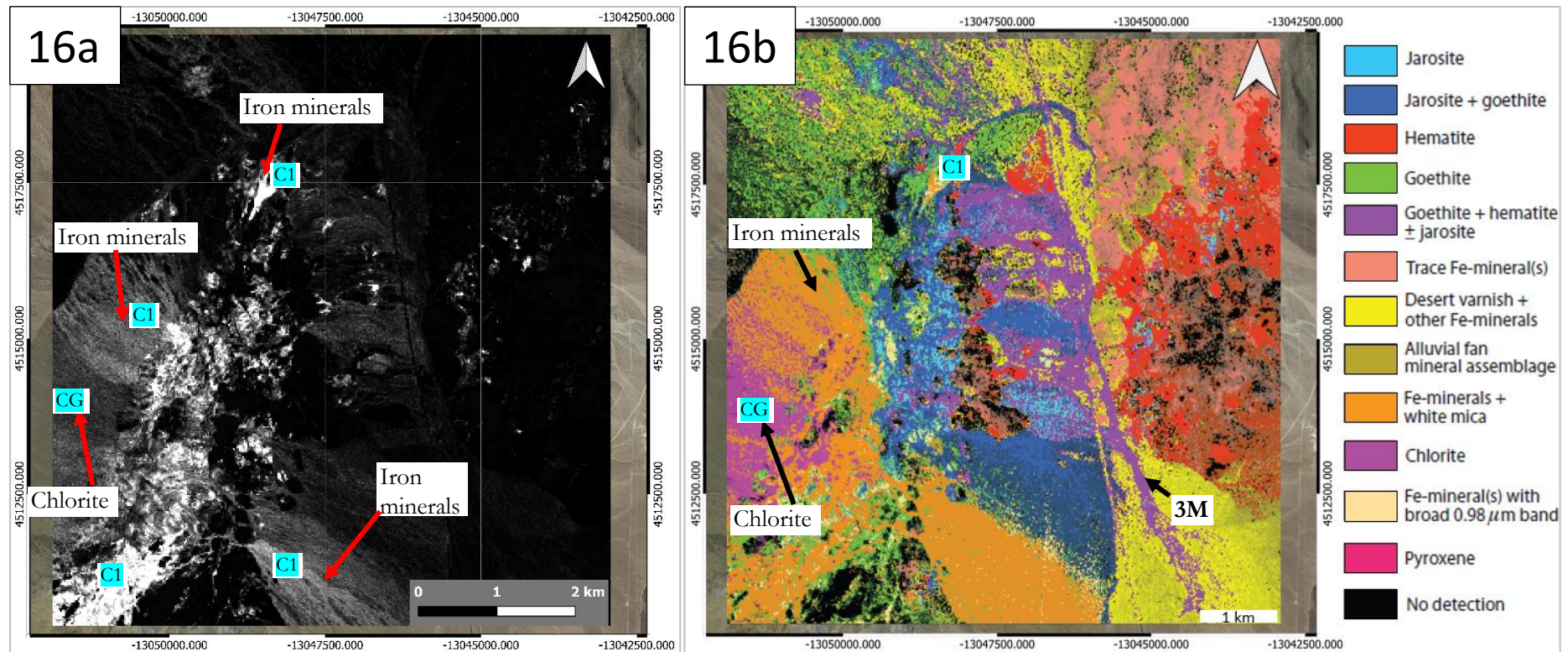


Figure 16a. Single-band gray image generated by the band ratio (B3/B2) highlighted mixtures of iron minerals distribution; however, the ratio discriminates goethite in the laboratory, predominantly in the southwest part of the image and some central part. Figure 16b Mineral map utilizing the 400- 1300 nm electronic absorption band of the AVIRIS data, showing the spectrally dominant Iron-bearing minerals at Cuprite.

Discrimination of individual Iron-bearing minerals with the Sentinel-2 Super-Spectral Imager

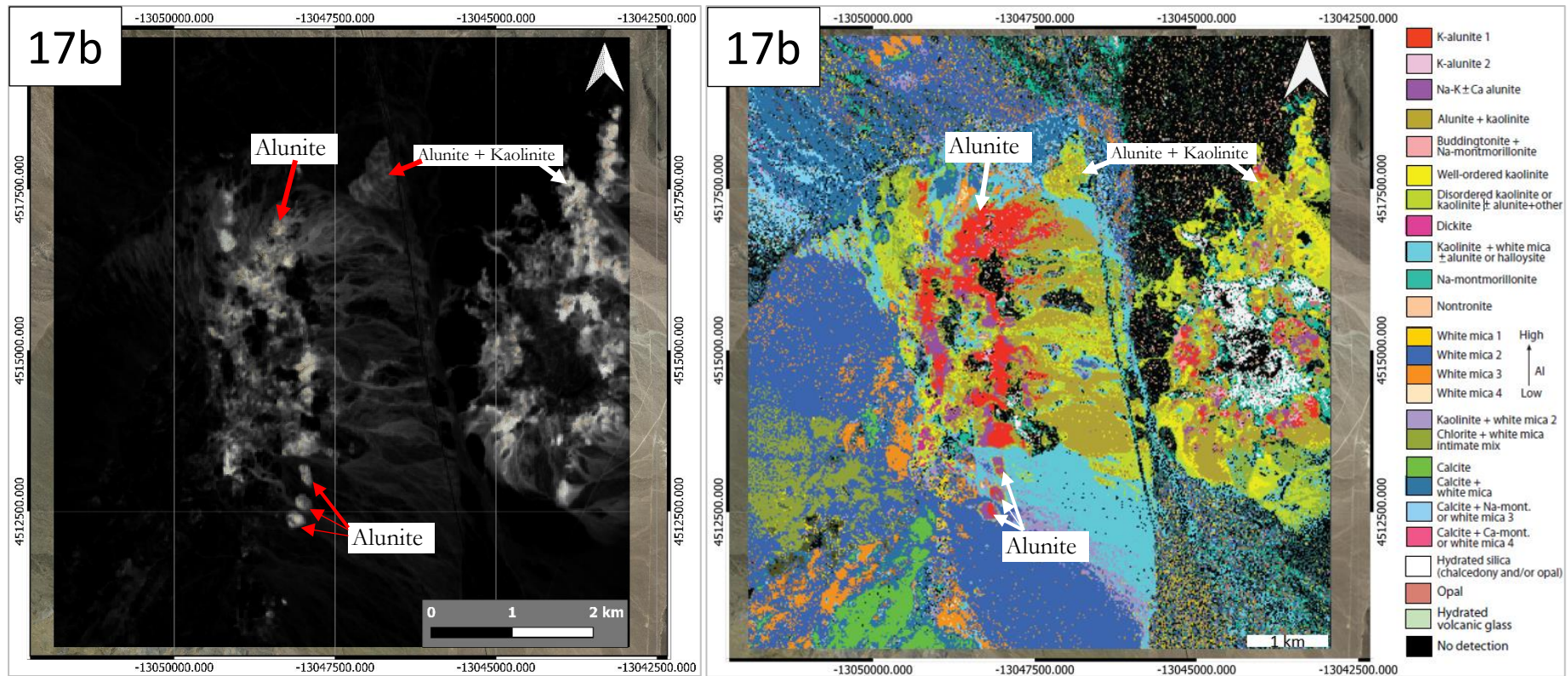


Figure 4Figure 17a Single-band gray image generated by the band ratio $(B5+B11)/B12$ highlights alteration zones, particularly in the west and east of the image. Alunite has the brightest pixels than kaolinite. 17b Mineral map of the 1300 to 2500 nm vibrational absorption wavelength region of the AVIRIS data, showing the spectrally dominant clays, micas, sulfates, and carbonates at Cuprite.

3.5.2 False Color Composite (RGB) map

This section shows a mineral map generated by combining three band ratios in RGB (B4/B3), (B3/B2), and (B5+B11/B12) to display the distribution of the iron-bearing minerals in the area. The Red color denotes Hematite; Green is a mixture of iron minerals with Goethite dominance; Blue is Alunite + Kaolinite + Jarosite. Furthermore, the RGB map is being compared with the published hyperspectral map.

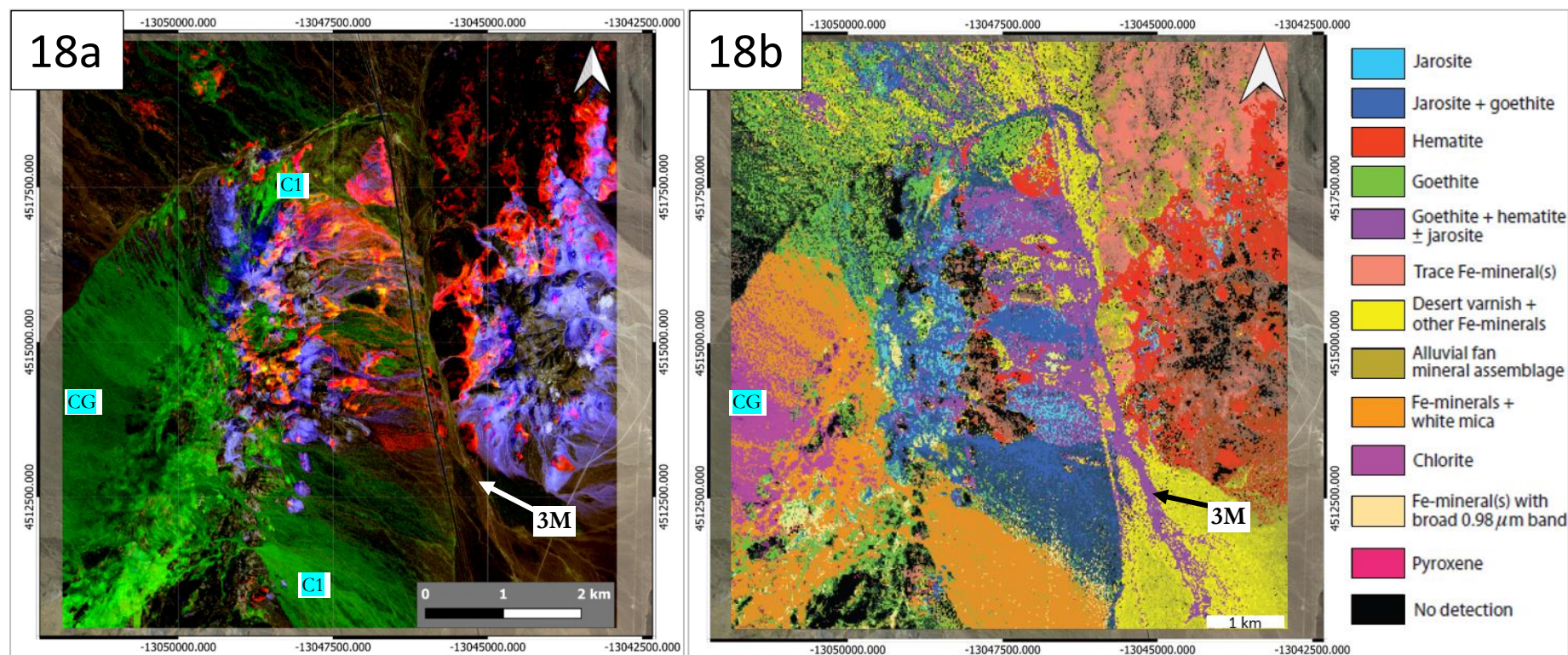


Figure 18 RGB false color composite map generated by combining three band ratios (B4/B3), (B3/B2), and (B5+B11/B12) shows the distribution of the iron-bearing minerals in the area. RGB: Red color denotes Hematite, Green is a mixture of iron minerals with Goethite dominance, and Blue is Alunite + Kaolinite + Jarosite. 18b Mineral map utilizing the 400- 1300 nm electronic absorption band of the AVIRIS data, showing the spectrally dominant Iron-bearing minerals at Cuprite.

Discrimination of individual Iron-bearing minerals with the Sentinel-2 Super-Spectral Imager

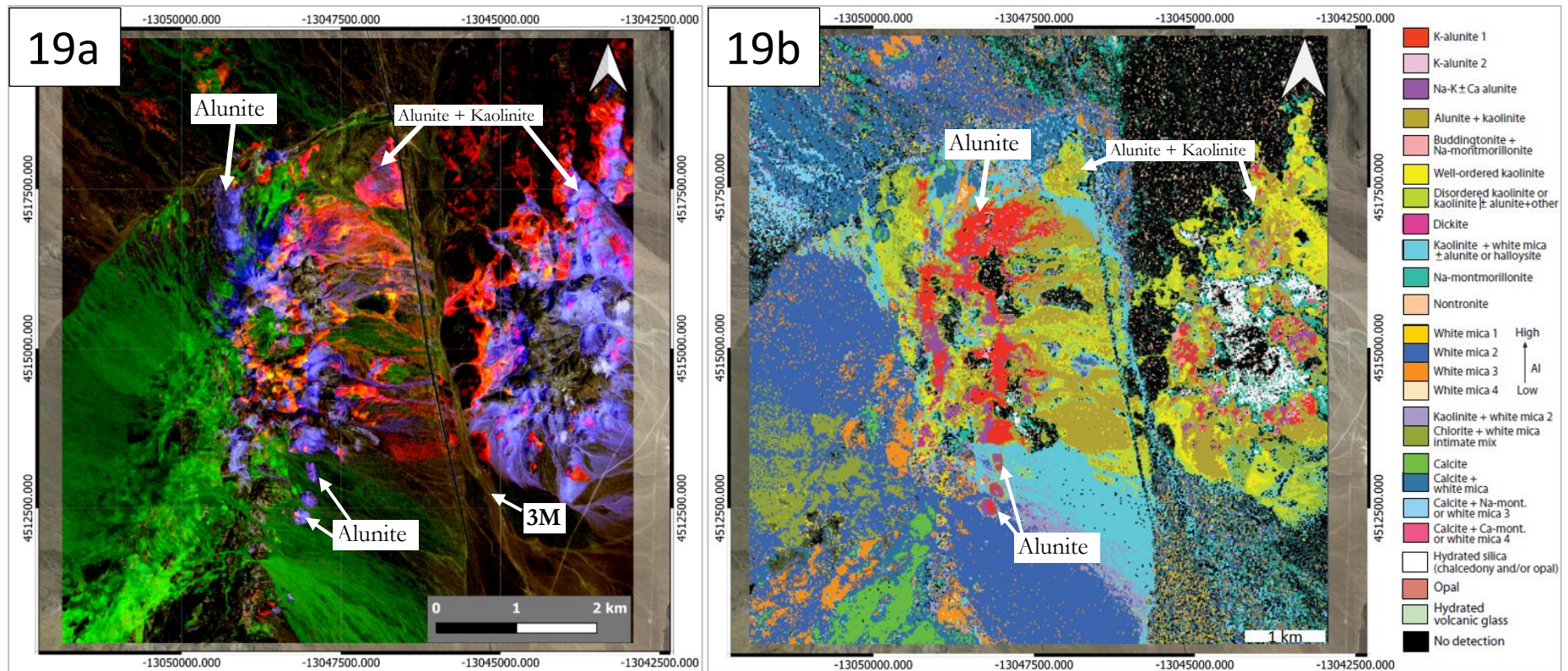


Figure 19a RGB false color composite map generated by combining three band ratios ($B4/B3$), ($B3/B2$), and ($B5+B11/B12$) shows the distribution of the iron-bearing minerals in the area. RGB: The Red color denotes Hematite, Green is a mixture of iron minerals with Goethite dominance, and Blue is Alunite + Kaolinite + Jarosite. 19b Mineral map of the 1300 to 2500 nm vibrational absorption wavelength region of the AVIRIS data, showing the spectrally dominant clays, micas, sulfates, and carbonates at Cuprite.

Discrimination of individual Iron-bearing minerals with the Sentinel-2 Super-Spectral Imager

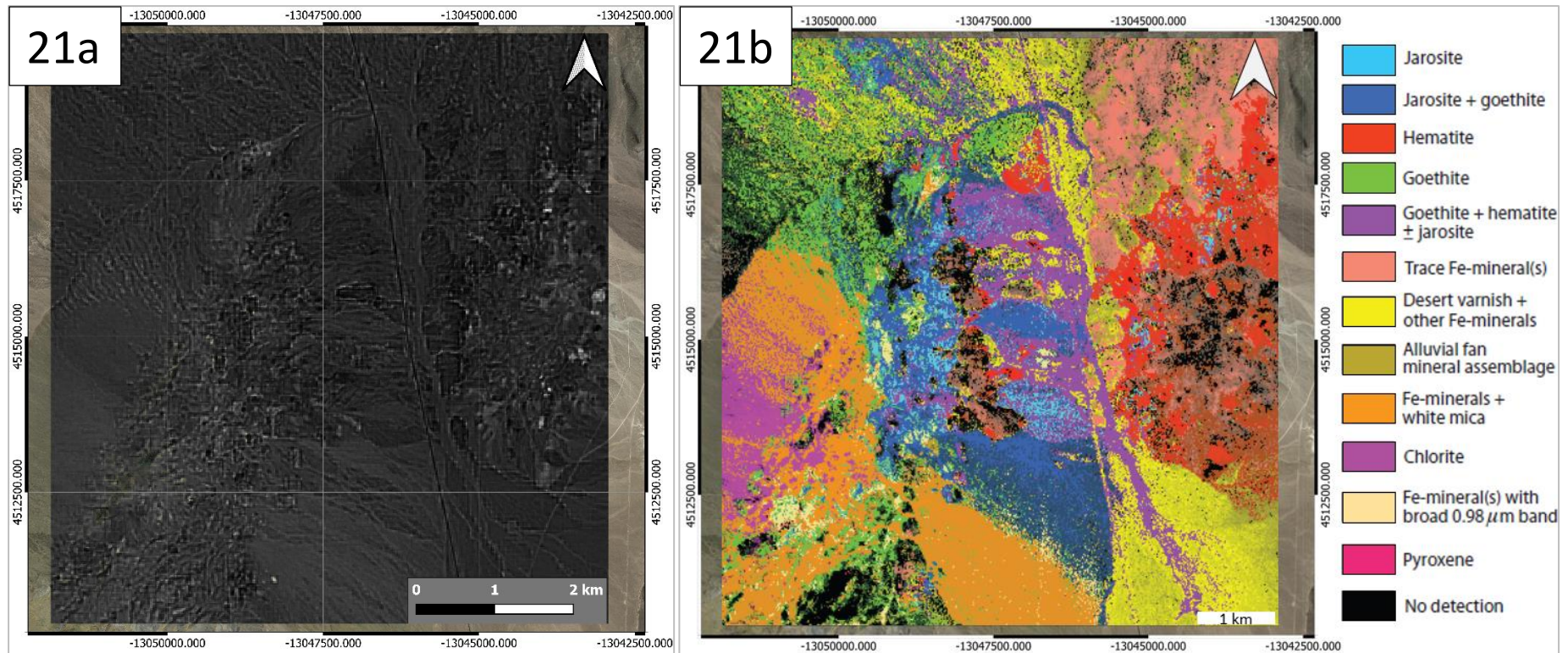


Figure 20a. Single-band gray image generated by the band ratio $(B3/B4)+(B7/B9)$ highlighted mixtures of Goethite with other iron minerals distribution; the ratio discriminates goethite in the laboratory. Here it show it did not show clear distribution. Figure 16b Mineral map utilizing the 400- 1300 nm electronic absorption band of the AVIRIS data, showing the spectrally dominant Iron-bearing minerals at Cuprite.

Discrimination of individual Iron-bearing minerals with the Sentinel-2 Super-Spectral Imager

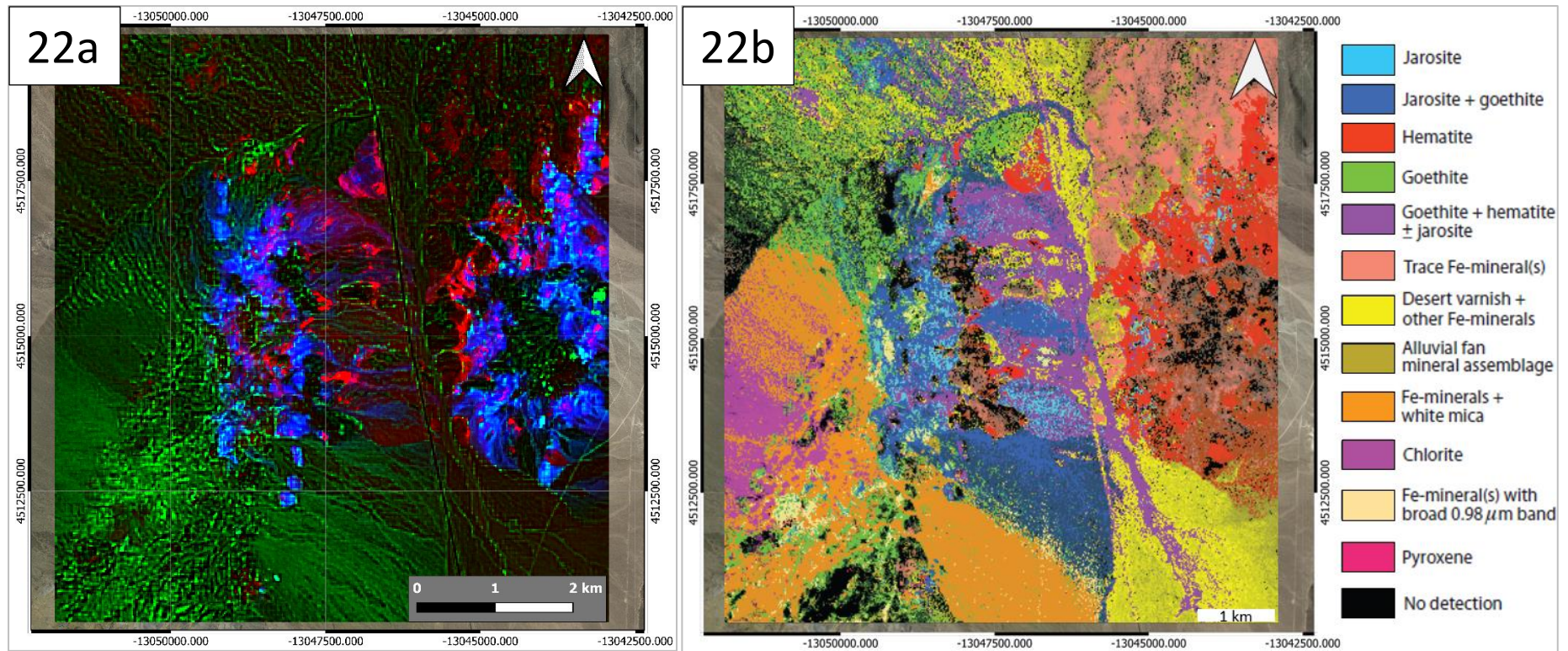


Figure 21 RGB false color composite map generated by combining three band ratios ($B4/B3$), $(B3/B4) + (B7/B9)$, and $(B5+B11/B12)$ shows the distribution of the iron-bearing minerals in the area. RGB: Red color denotes Hematite, Green is from $(B3/B4) + (B7/B9)$ and show a lot of mismatches, and Blue is Alunite + Kaolinite + Jarosite. 18b Mineral map utilizing the 400-1300 nm electronic absorption band of the AVIRIS data, showing the spectrally dominant Iron-bearing minerals at Cuprite.

4 DISCUSSION

This chapter intends to interpret the findings of this study, juxtaposing them against the established knowledge, explaining the methodologies, the significance of the results, and the potential implications for future mineralogical and remote sensing research. The chapter is divided into sections. Firstly, the Spectral features of iron minerals are discussed, where the applicability of the spectra from the USGS library is discussed, followed by a discussion on Pure Iron Minerals and Mixtures and their Influence on spectral features. The section deals with Multispectral Analysis, where Resampling and Comparison of Multispectral Sensors were discussed, followed by Band ratios analysis of existing and novel ratios, and finally, a Comparison of Sentinel-2 and Hyperspectral Output was presented. Firstly, the spectral features of iron minerals, examining the relevance of spectra from the USGS library, was discussed. This is succeeded by an exploration of pure iron minerals and mixtures and their respective implications on spectral features. The section then presents the multispectral analysis, highlighting the resampling and comparison of multispectral sensors. Further, the evaluation of band ratios focuses on both existing and novel ratios. To conclude, a comparative analysis of Sentinel-2 and Hyperspectral output is presented.

4.1 Spectral Features of Iron Minerals

The identification and mapping of minerals depend on understanding their distinctive spectral features and how they behave when interacting with other materials or environments. This section investigates the diagnostic characteristics of iron minerals and their associated mixtures, examining them in both laboratory and natural settings.

Following the analysis and evaluation of the USGS Spectral Library, it was observed that the spectra of specific iron minerals, such as hematite, jarosite, and goethite, are present in varied proportions and compositions (Table 8; Figure 7a-c). This means that the spectrum of hematite could be collected from a sample with impurities different from that of goethite and the same with jarosite, as discussed below. Consequently, it does not provide a leveling ground for comparing the influence of gangue or impurities on the various iron-bearing mineral spectra. For example, comparing the spectra of synthetically produced hematite (depicted in red) with the spectra available from the USGS library, the observation shows a considerable range in composition from the samples. These include mixtures with quartz, mica, and kaolinite, with quantities varying from 2% to unspecified amounts. These varied mineral proportions and compositions are not exactly available in goethite and jarosite. Their spectra, as illustrated in Table 8 and Figures 7 a-c, also have different sets of mineral mixtures in varied proportions.

The preceding discussion addresses the research questions. To provide further clarity, specific answers to these questions are detailed below. For instance, in Figure 7a, the jarosite spectra obtained from the USGS library display the characteristic broad features around 900 nm and 2250 nm, akin to the synthetic mineral samples. However, deviations in the spectral signatures were observed, with some spectra exhibiting shallower depths, weaker shoulders, and additional features. These variations are consistent with the metadata presented in Table 8, indicating differences in composition and spectrometer usage. In addition, the spectrum of Jarosite_GDS98_K_90C_Syn_NIC4a lacks features in the VNIR region due to the limitations of the spectrometer used in its collection. Furthermore, the spectrum of Jarosite_WS368_(Pb)_BECKc exhibits weak iron features, indicative of a distinct mineral composition. Similarly, the spectra of goethite and hematite from the USGS library and synthetic mineral samples display features around the 900 nm wavelength. However, some of these spectra exhibit deeper features that are characteristic of the minerals, while others appear shallower. Also alien features are also observed. This variation in depth of spectral features and introduction of new features highlights the effect of different mineral compositions and illustrates the broad spectral diversity within the same mineral type.

Consequently, these findings serve as a demonstration of the distinct spectral features that are necessary to consider when identifying and discriminating iron minerals using remote sensing techniques. This also highlights the invaluable utility of the USGS Spectral Library as a comparative tool and highlights the need to consult the USGS Library metadata before using spectra. Also, the applicability of the spectra from the USGS library depends on the objective of the study to be conducted.

The applicability of the USGS spectral library should be considered in the context of the specific research objectives and the limitations of the data. Therefore, the extent to which one can depend on this library for comparing pure iron minerals and mixtures depends on several factors. For example, it does not contain the spectra of all minerals that occur naturally and artificially and the variation in proportions and compositions of the samples. It is often beneficial to supplement library data with additional measurements or field observations specific to the study at hand.

4.1.1 Pure Iron Minerals and Mixtures

The XRD analysis results from section 3.1.1 showed distinct and characteristic peaks for each pure iron mineral. For jarosite, peaks were identified at the specific 2θ angles, corresponding to its unique crystalline structure established in the JCPDS database. The XRD pattern of the jarosite shows distinct peaks corresponding to the trigonal crystal system, with the most intense peak often observed around 26-28 degrees 2-theta (Figure 4a). At the same time, the XRD profile of goethite showed a similar match, with sharp and clear peaks corresponding to the documented crystallographic planes of goethite. The profile shows a strong diffraction peak around 21 degrees 2-theta and other smaller peaks at different angles. This profile reflects the orthorhombic crystal system as documented in the JCPDS database (Figure 4b). Moreover, the XRD patterns of hematite displayed characteristic peaks consistent with the established hematite profile in the JCPDS database. The peaks are sharp, signifying a very well-crystallized sample. The most intense peak is observed around 33 degrees 2-theta and several peaks. This profile reflects the rhombohedral crystal system as established in the JCPDS database (Figure 4c). These results confirmed the purity of these iron-bearing minerals, as each mineral's distinct diffraction pattern matched the known structures in the JCPDS database. The ability to match these specific mineral profiles with the established profile validates the synthetic minerals created. Conclusively, the XRD analysis provided a robust method of verifying the crystal structure of the synthesized minerals, thus confirming the reliability of the synthesized minerals used in this study.

The spectral characteristics of the synthetic minerals were determined using the VNIR (380-1000 nm) electromagnetic spectrum, highlighting the absorptions caused by electronic processes such as crystal field and charge transfer absorption. For example, hematite showed characteristic crystal-field absorptions at 520 and 867 nm, goethite at 659 and 929 nm, and jarosite at 906 nm (Figure 5). Hence, the earlier studies affirm the findings of this research as they coincide in demonstrating that each mineral possesses unique absorption features, which are reflective of its crystalline structure and composition.

Furthermore, charge transfer absorptions for the minerals jarosite, goethite, and hematite were observed at 436, 474, and 520 nm, respectively (Figure 5). In addition, jarosite has absorption at 2250 nm attributed to Fe-OH vibrational process (Figure 5). This indicates electron transitions between the different energy levels and hence, influences the spectral features of the minerals, thereby providing a basis for identification and discrimination. This indicates that the potential to employ the VNIR spectral signatures to distinguish between iron minerals in practical situations is highlighted. On the other hand, a hyperspectral sensor is capable of utilizing the SWIR feature, while a regular multispectral sensor, perhaps with the exception of ASTER, cannot do so. This means while a hyperspectral sensor can detect finer details in VNIR and SWIR wavelength regions, a typical multispectral sensor may lack this capacity, limiting its use in distinguishing certain minerals.

Furthermore, in an effort to improve the quality of the spectra that were acquired from spectral analysis using the ASD contact probe, attempts were made to manufacture pellets (Appendix 1-2). These pellets were prepared with 32 mm D/A ATLAS series dies (Specac) by applying 20 tons to compress 2 g of powdered goethite in 25-ton hydraulic pellet pressure (Specac), as shown in Appendix 1-2. This procedure was performed without moisture. However, the fragility and friability of the pellets, as well as the contamination of the binder, render this unachievable. Nevertheless, spectra of high quality were collected, and the aim was achieved.

Moreover, as shown in Figure 6, the physical properties of the synthetic minerals, mainly their different shades of colors, were unique and consistent with the literature discussed in the introduction. These colors directly reflect the type of wavelengths the mineral absorbs, reflects, and transmits, which is closely related to the electronic processes occurring within the mineral's crystal structure. Each mineral exhibits a unique color due to its unique absorption and reflection characteristics across the visible spectrum. For example, jarosite appears pale yellow because it absorbs light in the part of the spectrum associated with blue and violet. On the other hand, goethite is brown because it absorbs light in parts of the spectrum corresponding to blue and green. Hematite exhibits a deep red color due to the absorption of light in the blue-green portion of the spectrum. These color differences arise from the "color centers," which are specific points in a crystal lattice that can absorb and emit light of specific wavelengths. This result is also supported by previous research (Hunt, 2012). Recognizing these unique color-spectra relationships is crucial in the spectral analysis of minerals and their practical applications. However, one must keep in mind that while color can provide an initial clue, it alone cannot confirm the presence of a specific mineral due to factors like impurities, weathering, and variations in light conditions. Hence, it is often used in combination with other spectral features, such as absorption features in the NIR and SWIR wavelength regions, which can provide additional evidence for mineral identification.

4.1.2 Influence of mixtures on iron mineral spectral features

The study further revealed that changes in the concentration of synthetic iron minerals resulted in variations in the spectral intensity and color hue. For example, the mixture of hematite with calcite introduces absorption at 2250 nm and thus causes trouble differentiating the hematite from the jarosite (Figure 8b). Also, as the hematite concentration increased, the spectral features at 900 nm became broader and more intense, and the color deepened to a rich red color (Figure 8b). Similarly, mixtures of goethite and jarosite formed complex spectral signatures, where the two minerals introduce their features to the spectra (Figure 8a). Consequently, this suggests that mineral mixtures complicate the spectral signatures, making identification and discrimination more challenging. Therefore, the diversity in spectral compositions suggests that various proportions and mixtures of other minerals in natural environments can influence iron-bearing minerals' spectral signatures and color manifestation. This is crucial because it may result in incorrect mineral identification, thereby affecting remote sensing and mining exploitation.

The diagnostic spectral features of iron-bearing minerals can be distinguished within mixtures, depending on some conditions. These include the type of the mixture, the proportion of iron-bearing minerals relative to other minerals in the mixture (Figure 8a-b), and the specific sensor employed, as delineated in Table 8. Although the spectral characteristics of the iron minerals might experience subtle intensity variations, their positions, and shapes remain representative. Hence, while some mixtures might influence reflectance levels marginally, they do not introduce any notable spectral features in the region of interest. Even though the spectral features of pure iron-bearing minerals bear a resemblance to those in mixtures, the distinctions are mainly obvious in the depth of the features and potential additional characteristics based on mixture composition (as illustrated in Figure 8a-b). Mixtures with calcite and quartz tend to increase the reflectance levels of iron minerals, yet the diagnostic features persist as representative. For instance, within the VNIR wavelength domains, mixtures comprising quartz might increase reflectance while diminishing absorption

feature intensity; however, they do not introduce any obvious new features to the spectrum (as seen in Figure 8a-b).

4.2 Multispectral Analysis

The comparison of high-resolution spectra of synthetic iron minerals collected using the ASD with Sentinel-2, Landsat 8, and ASTER spectra offers valuable insights, as discussed in section 3.3. As Figure 9 illustrates, ASTER and Landsat 8 possess fewer bands in the VNIR wavelength region; thus, they lack bands at some wavelength positions where iron minerals have diagnostic features (Figure 1). This implies that these sensors may be limited in accurately identifying or discriminating iron-bearing minerals based on their spectral characteristics. In contrast, Sentinel-2 displayed a broader band presence in the VNIR than in ASTER and Landsat 8. This could provide a better spectral match with the high-resolution spectra of iron minerals, thus enhancing its ability to discriminate between minerals. This difference substantiates the choice of Sentinel-2 used in this study.

4.2.1 Existing band ratio analysis

Eight band ratios were evaluated to assess their success in discriminating the iron minerals. The assessment indicated that only one of these ratios ($B4/B3$) assigned a distinguishable score to hematite from jarosite and goethite (as illustrated in Table 11, Figure 10-12). As demonstrated in Figure 10, scatterplot analysis of pure iron minerals revealed a nonlinear distribution. This relationship was consistent when iron minerals mixtures were added and maintained with quartz and calcite mixtures. The scatterplot analysis showed that the band ratio ($B4/B3$) effectively discriminates hematite from goethite and jarosite, while ($B11/B8$) does not offer distinct discrimination between the minerals (Figure 10). Furthermore, scatterplots of band ratios $(B4/B2) \times (B4+B11)/B8$ and $(B12/B8) + (B3/B4)$ also showed that these ratios did not adequately distinguish between the minerals (Figure 12a-f). Hence, this suggests that while one existing band ratio can discriminate specific minerals, others may not distinguish the minerals. And this opens up a need for additional analysis and experimentation to provide more comprehensive mineral discrimination.

4.2.2 Novel band ratios experiment

The insufficiency of the existing band ratios, except for ($B4/B3$), emphasized the need to explore new band ratios that can more effectively discriminate between the minerals. Consequently, an initial analysis of the relationship between resampled Sentinel-2 bands and the spectral features of the iron minerals revealed specific relationships that were explored to discriminate the minerals (jarosite, goethite, and hematite) (Table 11). From the analysis, it can be observed that there are significant variations in the spectral characteristics of jarosite, goethite, and hematite across different Sentinel-2 bands. Consequently, this analysis forms a foundational basis for further experimentation with novel band ratios, as demonstrated in Figures 13 - 15.

Firstly, the analysis starts by testing single-band ratios to determine their success in distinguishing spectral features. The results from these tests, however, proved to be insufficient in providing the desired discrimination, as illustrated in section 3.4. Given the limitations of single-band ratios, the potential of combining multiple ratios was explored. Through the use of scatterplots, these combinations were examined (Figure 13-15). It was this approach that yielded the desired results, as discussed in section 3.4. This development from single to combined ratios highlights the complexities in iron-bearing mineral spectral discrimination and highlights the importance of iterative testing in identifying optimal techniques for specific minerals.

The experiment using the band ratios ($B3/B2$) vs. $(B3/B2) + (B7/B9)$ aimed at discriminating goethite show a linear trend (Figure 13a-c). This is evident with goethite consistently obtaining high scores, which not

only signifies its distinct spectral response but also highlights the utility of the band ratios in identifying the responses. Meanwhile, the allocation of intermediate scores to jarosite and low scores to hematite demonstrates a recognizable trend, which is beneficial for classification (Figure 13). However, the presence of overlapping points of jarosite and hematite when mixtures come into play, highlights the challenge of differentiating closely related or spectrally similar minerals (Figure 13c). While goethite stood out distinctly, jarosite and hematite will be classified together because they share a spectral neighborhood. Consequently, the overlap between jarosite and hematite indicates the complexity of using just one band ratios for differentiation, especially in terrains where mineral mixtures are prevalent. Furthermore, the correlation observed between the band ratios shows that one ratio can be used to validate the other. Since the correlation is strong, using both band ratios is redundant for this application because the aim is to discriminate between the minerals. therefore, one ratio ($B3/B2$) suffices.

Following limitations observed with the initial explored band ratios ($B5/B12$), ($B3/B4$), and ($B7/B9$), further band ratio analysis was conducted. More promising results were obtained by employing the Relative Absorption Band Depth technique and combining band ratios. Consequently, further analysis involving the ($B5/B12$) band ratio was introduced at the discriminate jarosite and the minerals. A deeper analysis considered incorporating band B11 into the formula, utilizing the Relative Absorption Band Depth approach as discussed in section 2.3.4. This method is based on the spectral feature of jarosite having a peak at B5 and B11 and absorption at B12, in contrast to goethite and hematite, both of which show absorption at B5 and peaks at B11 and B12. The results indicate that the band ratio $(B5+B11)/B12$ discriminates the minerals, assigning a high score to jarosite, an intermediate score to goethite, and a low score to hematite (Figure 14b). On the other hand, combining two band ratios ($B3/B4$) and ($B7/B9$) shows improvement in the discrimination of goethite, jarosite, and hematite minerals. Consequently, the new band ratio $(B3/B4)+(B7/B9)$ was introduced, and the results illustrated in Figure 14d demonstrate the discrimination of the minerals.

The $(B5+B11)/B12$ ratio provided discrimination between the iron minerals, with the jarosite obtaining distinct high scores, signifying its unique spectral signature in this ratio (Figure 14d). Goethite and hematite, however, were assigned intermediate and low scores, respectively. This is in contrast to the band ratio $(B3/B4)+(B7/B9)$, where goethite assigned high scores, followed by jarosite and hematite (Figure 14d). Such contrasts reveal the varied spectral features of these minerals and the sensitivity of different band ratios towards them. Furthermore, the scatterplots offer insights into the behavior of these minerals, especially in their pure forms versus their mixtures. The supported triangular trend observed in Figure 14c provides a representation of the variation in mineral composition. This is highlighted by the distinct position of the pure minerals in a nonlinear trend (Figure 14b-d).

This trend highlights the variable spectral behavior of the iron minerals based on their purity and mixture composition. In addition, one of the key observations was the clear correlation between the band ratios. This correlation appears both positive and negative depending on the mixtures, as shown in Figure 14d, and it can be an instrumental tool for the iron mineral classification. This is illustrated in the mixtures of iron minerals, as shown in Figure 14d; the positive correlation observed in the hematite+jarosite and hematite+goethite mixtures by the band ratios indicates a consistent and predictable behavior between these minerals. This is juxtaposed by the mixtures of goethite+jarosite, where a negative correlation is observed (Figure 14d). Such relationships suggest a counteractive behavior between these minerals when viewed through $(B3/B4) \times (B7/B9)$ vs $(B5+B11)/B12$ band ratios.

In addition, Figure 14b-d further highlights the behavior of the mineral mixtures by suggesting that as the iron mineral composition in these mixtures decreases, the data points tend to converge towards a central point, as illustrated in Figure 14d. This means that as the purity of the mineral decreases or as the mixture's proportion increases, the plots trend linearly toward the center. This is illustrated in Figure 14d by the

mixtures of iron minerals with quartz and calcite. The band ratios show a positive correlation for hematite mixtures with quartz and calcite and a negative correlation for goethite mixtures with quartz and calcite. Similarly, the ratios show a negative correlation for jarosite mixtures with quartz and calcite. Lastly, the triangular trend highlights the varied composition of the minerals; as mixtures become complex, the trend indicates a combining behavior of the data points, moving towards the center and mixing. It is essential to highlight, as depicted in Figure 8b that employing band 12 can be challenging in natural environments where calcite minerals dominate. It reveals that when mixed with calcite, both goethite and hematite display absorption around 2250 nm. Such an overlap makes distinguishing goethite and hematite from jarosite and other carbonate minerals challenging. This scenario highlights a practical challenge, given that iron minerals in nature do not occur in a pure state

4.2.3 Comparison of Sentinel-2 and Hyperspectral Output

The eastern area of the single-band gray image (Figure 15a) generated by (B4/B3) show bright pixel in the areas characterized as hematite by the published map (Figure 15b). These locations and the central part of the image have bright pixels, which coincide with hematite distribution in the published map. Interestingly, this ratio captures small areas in the central area, as shown in Figure 15a.

On the other hand, the single-band gray image (Figure 16a) generated by (B3/B2) shows the distribution of mixtures of iron minerals around the western part of the image; however, the ratio, when tested in the laboratory, discriminated goethite. This does not coincide completely with the published map, keeping in mind that this study employed a soft classification, unlike the hard classification of the published map (Figure 16b). In addition, the area marked as **CG** is characterized as chlorite in the published map is also highlighted. Although, the western area received intermediate brightness than the central, with a very bright pixel. This can be attributed to two factors or both. Firstly, this area has been documented by Swayze et al. (2014) to be a propylitic alteration zones, where the rocks have experienced low to moderate temperature hydrothermal alteration caused by iron and magnesium-bearing hydrothermal fluids forming chlorite and magnetite, and both subsequent weather to form goethite, when there is a presence of oxygen and moisture, leading to the oxidation of the iron(II) in chlorite to form iron(III) in goethite. The brightness may come from the goethite or their mixture. Secondly, the coexistence of both chlorite and goethite is possible, both being products of hydrothermal alteration processes, and both can capture features in the VNIR when chlorite has iron.

In addition, surrounding the chlorite area (**CG**) in the published map, which is denoted by **C1**, is also highlighted by the image of the (B3/B2) band ratio (Figure 16a). This area is classified as iron minerals, as shown in Figure 16b. Other bright pixels in the image are classified as iron minerals with a broad 980 nm band with white mica by the published hyperspectral map. However, white mica has no significant electronic absorptions but exhibited prominent features in the vibrational spectral region SWIR and hence did not interfere with the identification of the coexisting iron minerals in the VNIR, with a broad feature closer to 980 nm. Consequently, the brightness is due to iron minerals in the VNIR, and this ratio may have worked here because goethite is dominant. In addition, mica has been mapped at the location by a map generated by SWIR wavelength, as shown in Figure 17b. Therefore, **C1** is characterized as a mixture of goethite and iron minerals, with goethite being the dominant iron mineral.

The central area shown in Figure 17, the single-band gray image generated by the (B5+B11)/B12 ratio, intended to discriminate jarosite, shows very bright pixels in areas documented as no detection in the VNIR range published map as shown in Figure 16b. These are the alteration zones documented in the SWIR published map (Figure 17b). Consequently, this can be attributed to the influence of much stronger absorptions of kaolinite and alunite at 2265 nm (Figure 17b) corresponding to band 12, thereby overwhelming the vibrational absorption feature of Jarosite at 2265 nm, as shown in the image by (B5+B11)/B12 (Figure 17a). Similarly, the three blobs in the south are known as Alunite Hills (Swayze et

al., 2014) and are highlighted by $(B5+B11)/B12$. This is from the influence of the deep alunite feature around B12, with a very low reflectance value that makes the ratio show a very bright pixel, thereby overwhelming the jarosite feature. Depending on the geological condition, for instance, in an area where there is an absence of aluminum-rich rocks and jarosite is high in abundance, this ratio may work in identifying jarosite.

Furthermore, the central area, between the two alteration zones, often shows varied brightness ranging from low to intermediate to low. The variation may be attributed to variation in the composition. This area has been reported as an intercalation of propylitic alteration zones with advanced argillic zones. Therefore, the variation is attributed to mixtures of jarosite, goethite, and hematite intercalating with advanced argillic minerals (Figure 15b and 17b). In addition, the hyperspectral map also classified these areas as mixtures, as shown in Figures 15b and 17b.

Beyond single-band analysis, this study combines the selected band ratios to produce a map in RGB false color composite; this is because the ratios did not work individually but did when put together, thereby illustrating the distribution of the iron-bearing minerals collectively. Further, this map is compared with the published hyperspectral map to validate the similarities and ensure the accuracy of the observations.

A notable observation shows an area, denoted as **3M**, that a single ratio did not highlight (discussed in section 3.5.2), where the composition is a mixture of the three minerals as documented by the published map (Figure 15b). This area was not visible in the individual images generated through the different band ratios, as shown in Figures 15a-17a. However, it was observed in the RGB image developed by combining these band ratios. This observation highlights the improved accuracy in mineral identification when combining the band ratios, as opposed to utilizing them individually. The combined band ratio map shows similarities with the published hyperspectral map except for the distribution of jarosite. The observations suggest that hematite predominantly occupies some parts of the central and eastern parts of the map, with dominance in around the eastern region coinciding with the published map, while goethite is concentrated mainly in the southwest and some parts of the central regions. This also coincides with the published map. In contrast, jarosite does not appear to be discriminated by any of the novel band ratios. Therefore, the success of the novel band ratios is validated by their coinciding with the goethite and hematite distributions observed in the published maps.

5 CONCLUSION

The spectral analysis of iron minerals offers information that is important for various applications. However, understanding the complexities and variations associated with spectral signatures is crucial for accurate mineral identification and discrimination. This research bridges some of the existing knowledge gaps and emphasizes the importance of a comprehensive approach that takes into account the composition and sensor when interpreting mineral spectra.

Among the eight evaluated existing band ratios, only $(B4/B3)$ conclusively discriminates hematite from both jarosite and goethite. Other band ratios either group some minerals together or do not distinguish between them effectively. Although some existing band ratios may be utilized for Sentinel-2, their applicability is not comprehensive. Notably, existing band ratios struggle to differentiate goethite and hematite distinctly. The shortcomings of existing band ratios led to the development of novel band ratios. The complexity of discriminating iron-bearing minerals spectra means that a combination of band ratios is necessary. For instance, the band ratios $(B3/B2)$ vs. $(B3/B2)+(B7/B9)$ discriminated goethite in the laboratory, while in the real world is. Meanwhile, the band ratio $(B5+B11)/B12$ successfully differentiated jarosite from both goethite and hematite. However, this ratio worked in the laboratory, but it was not successful in the real world because of the influence of alunite on band 12. Further, the ratio $(B3/B4)+(B7/B9)$ discriminated goethite in the laboratory and but it did not work in real-world settings.

Furthermore, the spectral behavior of iron minerals varies, particularly when they are in pure form versus when they are in mixtures. The correlation between band ratios is influenced by the minerals' composition in the mixtures. This suggests that mineral mixtures can introduce challenges in discrimination, especially when using a singular band ratio. Iron minerals, when combined with quartz and calcite, display specific trends based on their composition and mixture ratios, revealing the complexity of mineral behavior. Similarly, in natural environments, the presence of other minerals, especially carbonate minerals like calcite, can introduce complications in the discrimination of iron-bearing minerals. For instance, the overlap observed in the 2250 nm range when goethite and hematite mix with calcite signifies potential error when using certain band ratios in calcite-dominant terrains.

In the real-world setting of the Cuprite area, hematite distribution was successfully identified with bright pixel patterns signifying hematite distribution in the eastern and central parts of the image generated by the ratio $(B4/B3)$. This observation was consistent with the published map. Similarly, the $(B3/B2)$ band ratio mainly displayed goethite's distribution, specifically towards the western region. Notably, there were inconsistencies compared with the published map, which may be attributed to various factors: the coexistence of chlorite and goethite and differences in classification methods between the soft classification of this study and the hard classification of the published map. Furthermore, the combined band ratio in the RGB false color composite has proved beneficial, especially when the individual band ratios were insufficient in mineral identification. The generated RGB image revealed areas that the single ratios did not highlight, where the composition is a mixture of the three minerals, as shown in section 3.5.2. Therefore, this shows the advantage of using combined band ratios over single band ratios. In addition, discrepancies were observed in the identification of jarosite using the $(B5+B11)/B12$ band ratio. This could be attributed to the overwhelming vibrational absorption features of minerals like kaolinite and alunite, potentially masking the weaker absorption feature of jarosite.

Finally, the study has successfully identified specific iron minerals, particularly hematite and goethite, in the real-world setting that display consistency with the reference map, utilizing novel band ratios produced using Sentinel-2 bands. The band ratios $(B4/B3)$ identified hematite, whereas $(B3/B2)$ highlighted mixtures predominantly consisting of goethite and other iron minerals, and $(B5+B11)/B12$ identified mixtures of jarosite, alunite, and kaolinite. Moreover, $(B3/B4)+(B7/B9)$ worked in the laboratory but did not in the

Discrimination of individual Iron-bearing minerals with the Sentinel-2 Super-Spectral Imager

real-world. In addition, this research has successfully produced high-quality spectra of iron minerals, thereby adding to the existing spectral libraries, and can be used as a reference for future studies. Also, the study revealed the challenges related to the interaction of iron minerals with minerals in the real world, which may pose discrimination difficult.

5.1 Research questions

1. How much can be depended on the USGS spectral library for comparing pure iron minerals and mixtures?

Although the USGS spectral library is a fundamental tool, its coverage of iron minerals has notable gaps that impact its reliability for band ratio tests and comparison. The laboratory tests have demonstrated the behaviour of iron minerals in mixtures and the variations in their spectra that result from mixtures that are not fully represented in the library.

2. Can the diagnostic spectral features of iron-bearing minerals be distinguished in mixtures?

The diagnostic spectral features of iron-bearing minerals can be distinguished within mixtures, depending on some conditions. These include the type of the mixture, the proportion of iron-bearing minerals relative to other minerals in the mixture (Figure 7a-c), and the specific sensor employed, as delineated in Table 8. Although the spectral characteristics of the iron minerals might experience subtle intensity variations, their positions, and shapes remain representative. Hence, while some mixtures might influence reflectance levels marginally, they do not introduce any notable spectral features in the region of interest.

3. How do the spectral features of pure iron-bearing minerals and their mixtures compare?

While the spectral features of pure iron-bearing minerals bear a resemblance to those in mixtures, the distinctions are mainly obvious in the depth of the features and potential additional characteristics based on mixture composition (as illustrated in Figure 7a-c). Mixtures with calcite and quartz tend to increase the reflectance levels of iron minerals, yet the diagnostic features persist as representative. For instance, within the VNIR wavelength domains, mixtures comprising quartz might increase reflectance while diminishing absorption feature intensity; however, they do not introduce any obvious new features to the spectrum (as seen in Figure 7a-c).

4. Can the band ratios suggested for other sensors be used in Sentinel-2?

Many of the existing band ratios were originally proposed for different sensors, as highlighted in Table 3. This suggests that Sentinel-2 possesses bands equivalent to those of the other sensors, as depicted in Figure 9. Consequently, these ratios are applicable to Sentinel-2.

5. Which iron-bearing minerals can be identified using the existing Sentinel-2 band ratio methods?

The outcome of the result section shows that hematite can be identified and discriminated from other minerals using an existing band ratio (B4/B3), while others can be identified as a group of iron minerals.

6. Which iron-bearing minerals have not been discriminated against using the existing Sentinel-2 band ratios from the published literature?

Goethite and hematite have not been individually discriminated using the existing band ratios as discussed in section 3.3.1.

7. Which iron-bearing minerals are discriminated against using high-resolution methods, such as hyperspectral data, and which ones were found with multispectral data?

Hyperspectral data, with its high-resolution bands, effectively discriminates among a variety of iron minerals, notably jarosite, goethite, and hematite, as illustrated in section 3.5. On the other hand, multispectral data, due to its limited spectral resolution, primarily discriminates between goethite and hematite, as shown in Figure. This limitation using multispectral data arises from its broader bands, which capture less spectral detail compared to hyperspectral data.

8. How does Sentinel-2's output compare to the hyperspectral output that has been published?

Sentinel-2 output may show a more generalized representation or mineral distribution when mapping spectrally closely related minerals. For instance, when mapping jarosite in a real-world setting that has alunite or kaolinite associated with it, it may lead to overlapping spectral signatures and, subsequently, difficulty in discriminating between the minerals. This is demonstrated in section 3.5. Figures 18-19.

5.3 Recommendations

1. For accurate interpretation of spectral data, it is recommended to check the type of mixture, the proportion of iron-bearing minerals in relation to other components, and the specific sensor used.
2. It is recommended that in mineral exploration, especially in regions known for iron ore deposits, prioritize the use of the band ratio (B4/B3) due to its proven success in distinguishing hematite.
3. The limitations of existing band ratios emphasize the need to continue developing and testing novel band ratios, especially those that show promise in laboratory settings but not in real-world applications.
4. It is important to investigate how goethite interacts spectrally with common minerals like chlorite because of their association in some geological contexts where they coexist, like the cuprite area. Future studies should explore further the implications of mixtures and aim for advanced techniques that can handle the challenges posed by spectral variability.
5. It is recommended to employ a data fusion approach that merges spatial information from sentinel-2 data with subsurface information from geochemical and geophysical data, such as magnetic data, to explore the magnetic properties of the subsurface and radiometric data to detect radioelement concentrations.

REFERENCES

- Abrams, M. (2000). The Advanced Spaceborne Thermal Emission and Reflection Radiometer (ASTER): Data products for the high spatial resolution imager on NASA's Terra platform. *International Journal of Remote Sensing*, 21(5), 847–859. <https://doi.org/10.1080/014311600210326>
- Abrams, M., & Hook, S. J. (1995). Simulated Aster Data for Geologic Studies. *IEEE Transactions on Geoscience and Remote Sensing*, 33(3), 692–699. <https://doi.org/10.1109/36.387584>
- Andrews Deller, M. E. (2006). Facies discrimination in laterites using Landsat Thematic Mapper, ASTER and ALI data-examples from Eritrea and Arabia. *International Journal of Remote Sensing*, 27(12), 2389–2409. <https://doi.org/10.1080/01431160600586050>
- Bigham, J. M., Fitzpatrick, R. W., & Schulze, D. G. (2018). Iron oxides. In *Soil Mineralogy with Environmental Applications* (Vol. 7, pp. 323–366). Wiley Blackwell. <https://doi.org/10.2136/sssabookser7.c10>
- Bullock, L. A., James, R. H., Matter, J., Renforth, P., & Teagle, D. A. H. (2021). Global Carbon Dioxide Removal Potential of Waste Materials From Metal and Diamond Mining. *Frontiers in Climate*, 3. <https://doi.org/10.3389/fclim.2021.694175>
- Butt, C. R. M., & Zeegers, H. (1992). Regolith exploration geochemistry in tropical and subtropical terrains. *Regolith Exploration Geochemistry in Tropical and Subtropical Terrains*. [https://doi.org/10.1016/0375-6742\(93\)90050-v](https://doi.org/10.1016/0375-6742(93)90050-v)
- Clark, R. N., Swayze, G. A., Gallagher, A. J., King, T. V. V., & Calvin, W. M. (1993). The U.S. Geological Survey, Digital Spectral Library: Version 1 : 0.2 to 3.0 μm . *U.S. Geological Survey Open File Report 93-592*, 1, 1326.
- Cogram, P. (2018). Jarosite. In *Reference Module in Earth Systems and Environmental Sciences*. Elsevier. <https://doi.org/10.1016/b978-0-12-409548-9.10960-1>
- Cooper, B. L., Salisbury, J. W., Killen, R. M., & Potter, A. E. (2002). Midinfrared spectral features of rocks and their powders. *Journal of Geophysical Research: Planets*, 107(4). <https://doi.org/10.1029/2000je001462>
- Crowley, J. K., Brickey, D. W., & Rowan, L. C. (1989). Airborne imaging spectrometer data of the Ruby Mountains, Montana: Mineral discrimination using relative absorption band-depth images. *Remote Sensing of Environment*, 29(2), 121–134. [https://doi.org/10.1016/0034-4257\(89\)90021-7](https://doi.org/10.1016/0034-4257(89)90021-7)
- Crowley, J. K., Williams, D. E., Hammarstrom, J. M., Piatak, N., Chou, I. M., & Mars, J. C. (2003). Spectral reflectance properties (0.4–2.5 μm) of secondary Fe-oxide, Fe-hydroxide, and Fe-sulphate-hydrate minerals associated with sulphide-bearing mine wastes. *Geochemistry: Exploration, Environment, Analysis*, 3(3), 219–228. <https://doi.org/10.1144/1467-7873/03-001>
- Cudahy, T. J., & Ramanaidou, E. R. (1997). Measurement of the hematite: Goethite ratio using field visible and near-infrared reflectance spectrometry in channel iron deposits, Western Australia. *Australian Journal of Earth Sciences*, 44(4), 411–420. <https://doi.org/10.1080/08120099708728322>
- Dahm, K. D., & Dahm, D. J. (2020). Theoretical Models of Light Scattering and Absorption. In *Near-Infrared Spectroscopy: Theory, Spectral Analysis, Instrumentation, and Applications* (pp. 37–60). Springer Singapore. https://doi.org/10.1007/978-981-15-8648-4_3
- Driscoll, R. L., & Leinz, R. W. (2005). *Methods for Synthesis of Some Jarosites: U.S. Geological Survey Techniques and Methods 5-D1*. 5.
- Drusch, M., Del Bello, U., Carlier, S., Colin, O., Fernandez, V., Gascon, F., Hoersch, B., Isola, C., Laberinti, P., Martimort, P., Meygret, A., Spoto, F., Sy, O., Marchese, F., & Bargellini, P. (2012). Sentinel-2: ESA's Optical High-Resolution Mission for GMES Operational Services. *Remote Sensing of Environment*, 120, 25–36. <https://doi.org/10.1016/j.rse.2011.11.026>

Discrimination of individual Iron-bearing minerals with the Sentinel-2 Super-Spectral Imager

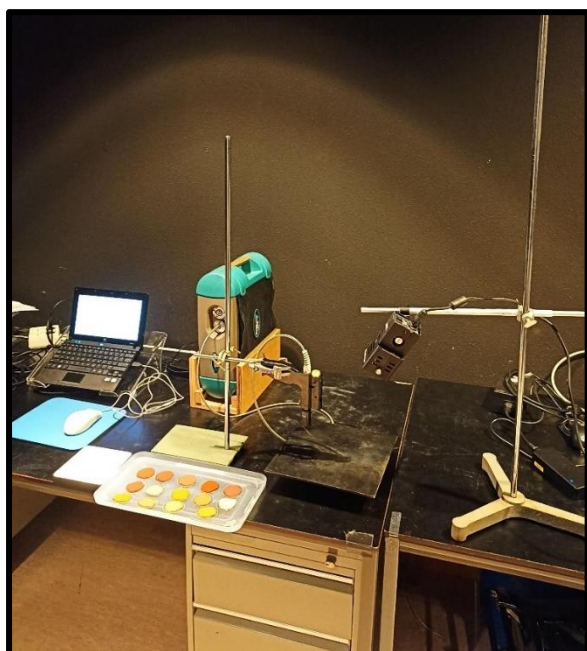
- Ducart, D. F., Silva, A. M., Toledo, C. L. B., & De Assis, L. M. (2016). Mapping iron oxides with Landsat-8/OLI and EO-1/Hyperion imagery from the Serra Norte iron deposits in the Carajás Mineral Province, Brazil. *Brazilian Journal of Geology*, 46(3), 331–349. <https://doi.org/10.1590/2317-4889201620160023>
- Edwards, R., & Atkinson, K. (1986). Ore deposits formed by weathering. In *Ore Deposit Geology and its Influence on Mineral Exploration* (pp. 274–313). Springer Netherlands. https://doi.org/10.1007/978-94-011-8056-6_7
- Farrand, W. H., Glotch, T. D., Rice, J. W., Hurowitz, J. A., & Swayze, G. A. (2009). Discovery of jarosite within the Mawrth Vallis region of Mars: Implications for the geologic history of the region. *Icarus*, 204(2), 478–488. <https://doi.org/10.1016/J.ICARUS.2009.07.014>
- Goetz, A. F. H., & Rowan, L. C. (1981). Geologic remote sensing. *Science*, 211(4484), 780–791. <https://doi.org/10.1126/science.211.4484.781>
- Hewson, R. D., Cudahy, T. J., & Huntington, J. F. (2001). Geologic and alteration mapping at Mt fitton, South Australia, using ASTER satellite-borne data. *International Geoscience and Remote Sensing Symposium (IGARSS)*, 2, 724–726. <https://doi.org/10.1109/igarss.2001.976615>
- Hunt, G. R. (2012). SPECTRAL SIGNATURES OF PARTICULATE MINERALS IN THE VISIBLE AND NEAR INFRARED. <https://doi.org/10.1190/1.1440721>, 42(3), 501–513. <https://doi.org/10.1190/1.1440721>
- Jaiswal, A., Banerjee, S., Mani, R., & Chattopadhyaya, M. C. (2013). Synthesis, characterization and application of goethite mineral as an adsorbent. *Journal of Environmental Chemical Engineering*, 1(3), 281–289. <https://doi.org/10.1016/j.jece.2013.05.007>
- Kalinowski, A., & Oliver, S. (2004). ASTER processing manual. *Geoscience Australia*, 37(October), 1–40.
- Kokaly, R. F., Clark, R. N., Swayze, G. A., Livo, K. E., Hoefen, T. M., Pearson, N. C., Wise, R. A., Benzel, W. M., Lowers, H. A., Driscoll, R. L., & Klein, A. J. (2017). *USGS Spectral Library Version 7: U.S. Geological Survey Data Series 1035*. U.S. Geological Survey. <http://pubs.er.usgs.gov/publication/ds1035>
- Koski, R. A. (2010). Supergene Ore and Gangue Characteristics. In *Usgs*.
- Mars, J. C., & Rowan, L. C. (2010). Spectral assessment of new ASTER SWIR surface reflectance data products for spectroscopic mapping of rocks and minerals. *Remote Sensing of Environment*, 114(9), 2011–2025. <https://doi.org/10.1016/j.rse.2010.04.008>
- Mielke, C., Boesche, N. K., Rogass, C., Kaufmann, H., Gauert, C., & de Wit, M. (2014). Spaceborne mine waste mineralogy monitoring in South Africa, applications for modern push-broom missions: Hyperion/OLI and EnMAP/Sentinel-2. *Remote Sensing*, 6(8), 6790–6816. <https://doi.org/10.3390/rs6086790>
- Rockwell, B. W. (2013). Automated Mapping of Mineral Groups and Green Vegetation from Landsat Thematic Mapper Imagery with an Example from the San Juan Mountains, Colorado. *U.S. Geological Survey Scientific Investigations Map 3252*, 25. <http://pubs.usgs.gov/sim/3252/>
- Rowan, L. C., Hook, S. J., Abrams, M. J., & Mars, J. C. (2003). Mapping hydrothermally altered rocks at Cuprite, Nevada, using the advanced spaceborne thermal emission and reflection radiometer (Aster), a new satellite-imaging system. *Economic Geology*, 98(5), 1019–1027. <https://doi.org/10.2113/gsecongeo.98.5.1019>
- Sabins, F. F. (1999). Remote sensing for mineral exploration. *Ore Geology Reviews*, 14(3–4), 157–183. [https://doi.org/10.1016/S0169-1368\(99\)00007-4](https://doi.org/10.1016/S0169-1368(99)00007-4)
- Salisbury, J. W., Walter, L. S., & Vergo, N. (1989). Availability of a library of infrared (2.1–25.0 μm) mineral spectra. *American Mineralogist*, 74(7–8), 938–939.

Discrimination of individual Iron-bearing minerals with the Sentinel-2 Super-Spectral Imager

- Sankadiya, S., Oswal, N., Jain, P., & Gupta, N. (2016). Synthesis and characterization of Fe₂O₃ nanoparticles by simple precipitation method. *AIP Conference Proceedings*, 1724. <https://doi.org/10.1063/1.4945184>
- Schetselaar, E. M., Tiainen, M., & Woldai, T. (2008). Integrated geological interpretation of remotely sensed data to support geological mapping in Mozambique. *Special Paper of the Geological Survey of Finland*, 2008(48), 35–63.
- Schwertmann, U. (1958). *The Effect of Pedogenic Environments on Iron Oxide Minerals* (pp. 171–200). https://doi.org/10.1007/978-1-4612-5046-3_5
- Swayze, G. A., Clark, R. N., Goetz, A. F. H., Livo, K. E., Breit, G. N., Kruse, F. A., Sutley, S. J., Snee, L. W., Lowers, H. A., Post, J. L., Stoffregen, R. E., & Ashley, R. P. (2014). Mapping advanced argillic alteration at Cuprite, Nevada, using imaging spectroscopy. *Economic Geology*, 109(5), 1179–1221. <https://doi.org/10.2113/econgeo.109.5.1179>
- Transon, J., d'Andrimont, R., Maignard, A., & Defourny, P. (2018). Survey of hyperspectral Earth Observation applications from space in the Sentinel-2 context. In *Remote Sensing* (Vol. 10, Issue 2). MDPI AG. <https://doi.org/10.3390/rs10020157>
- Van der Meer, F. D., van der Werff, H. M. A., & van Ruitenbeek, F. J. A. (2014). Potential of ESA's Sentinel-2 for geological applications. *Remote Sensing of Environment*, 148, 124–133. <https://doi.org/10.1016/j.rse.2014.03.022>
- van der Meer, F. D., van der Werff, H. M. A., van Ruitenbeek, F. J. A., Hecker, C. A., Bakker, W. H., Noomen, M. F., van der Meijde, M., Carranza, E. J. M., de Smeth, J. B., & Woldai, T. (2012). Multi- and hyperspectral geologic remote sensing: A review. In *International Journal of Applied Earth Observation and Geoinformation* (Vol. 14, Issue 1, pp. 112–128). Elsevier B.V. <https://doi.org/10.1016/j.jag.2011.08.002>
- van der Werff, H., & van der Meer, F. (2015). Sentinel-2 for mapping iron absorption feature parameters. *Remote Sensing*, 7(10), 12635–12653. <https://doi.org/10.3390/rs71012635>
- van der Werff, H., & van der Meer, F. (2016). Sentinel-2A MSI and Landsat 8 OLI provide data continuity for geological remote sensing. *Remote Sensing*, 8(11). <https://doi.org/10.3390/rs8110883>
- Yamaguchi, Y., Kahle, A. B., Tsu, H., Kawakami, T., & Pniel, M. (1998). Overview of advanced spaceborne thermal emission and reflection radiometer (ASTER). *IEEE Transactions on Geoscience and Remote Sensing*, 36(4), 1062–1071. <https://doi.org/10.1109/36.700991>
- Zhou, S., Jiang, K., Chen, H., & Wang, Z. (2017). Correlation effects and hidden spin-orbit entangled electronic order in parent and electron-doped iridates Sr₂IrO₄. *Physical Review X*, 7(4). <https://doi.org/10.1103/PhysRevX.7.041018>

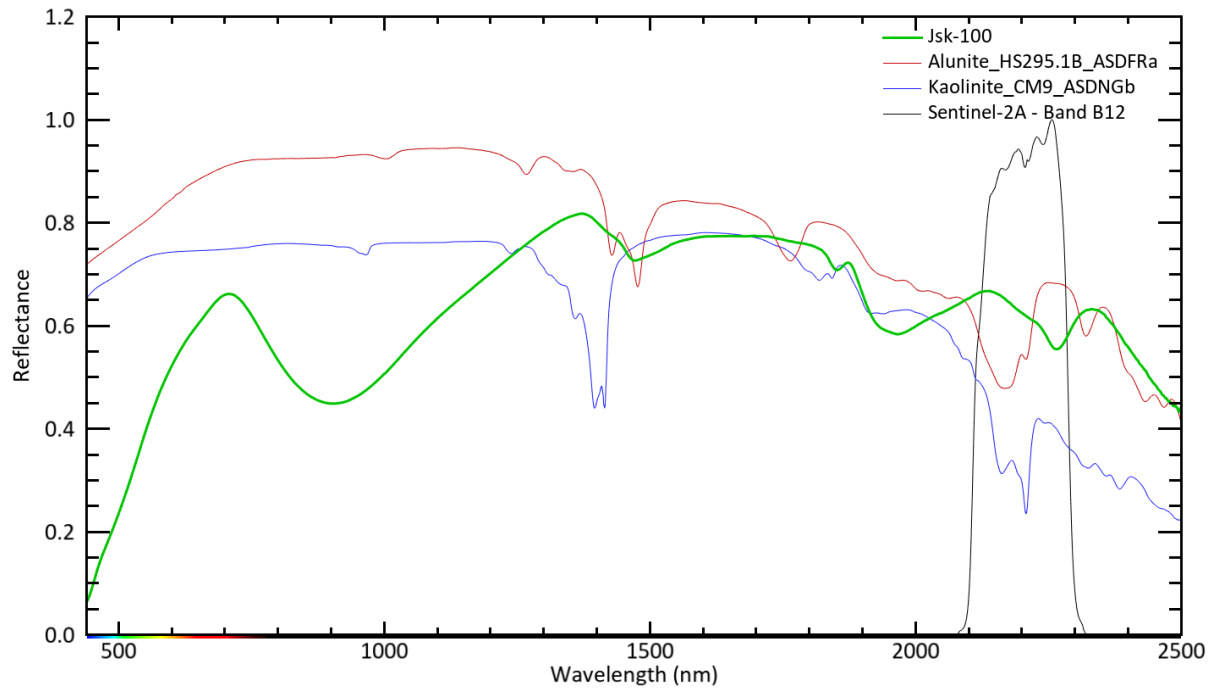
APPENDICES

Appendix 1: Mineral synthesis and analytical techniques

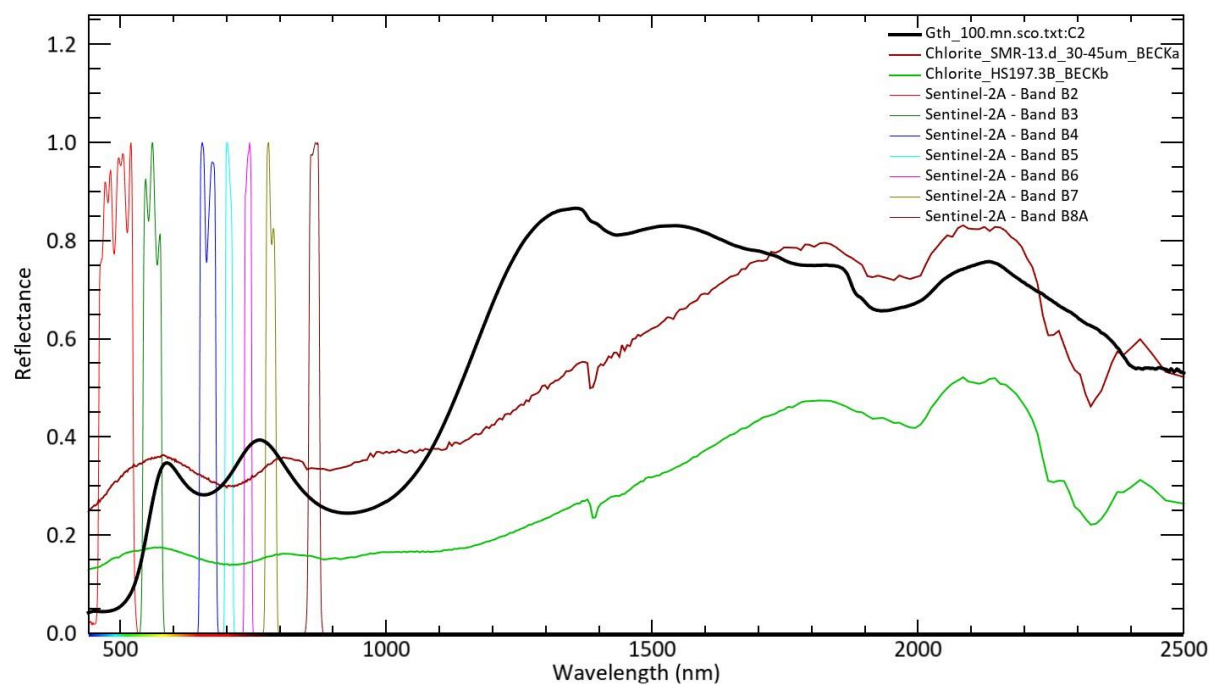


Discrimination of individual Iron-bearing minerals with the Sentinel-2 Super-Spectral Imager

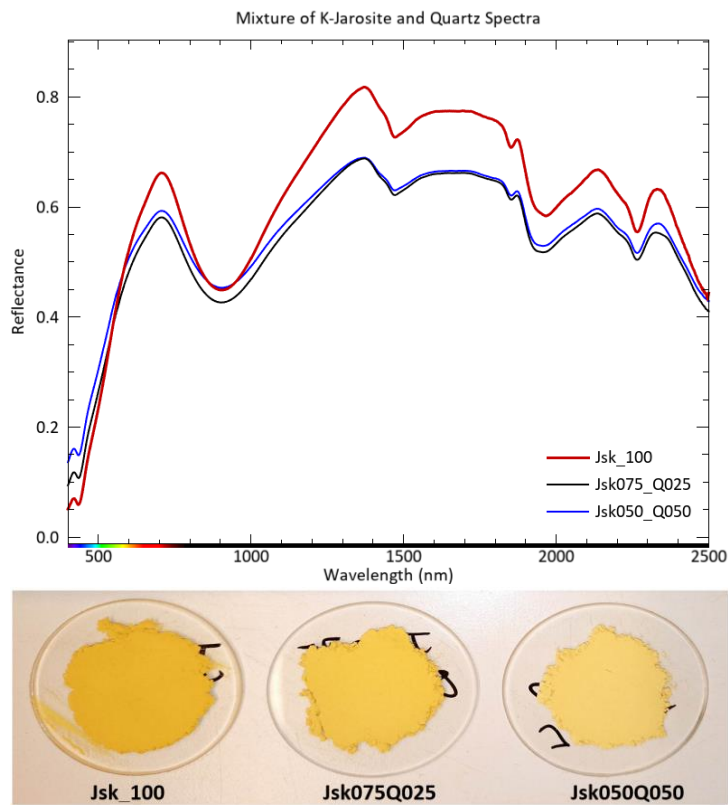
Appendix 3: Spectra of jarosite against alunite, kaolinite and band 12



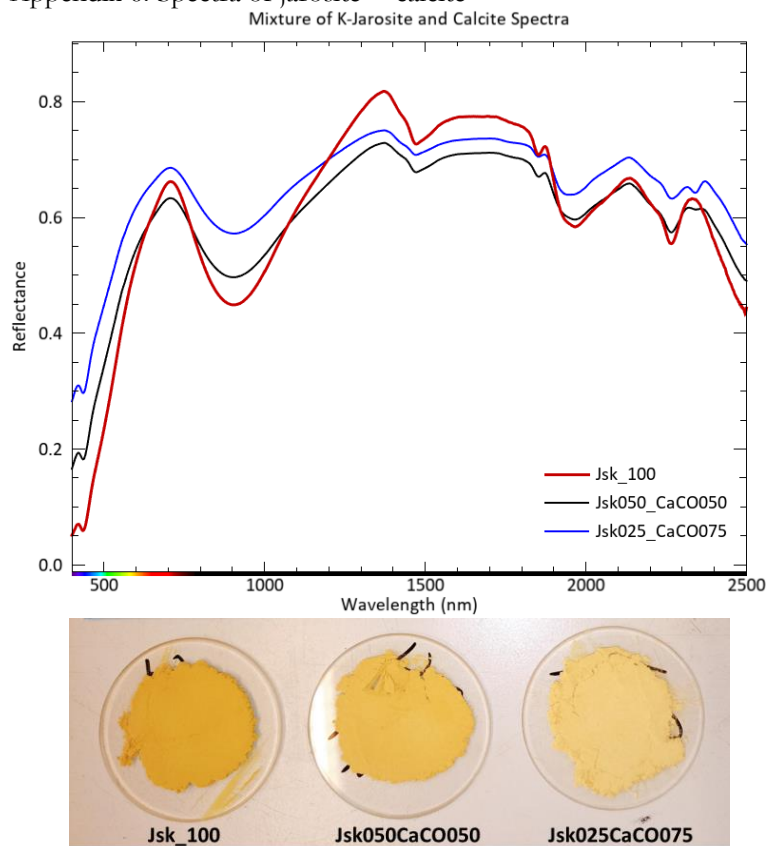
Appendix 4: Spectra of goethite against chlorite and Sentinel-2 bands



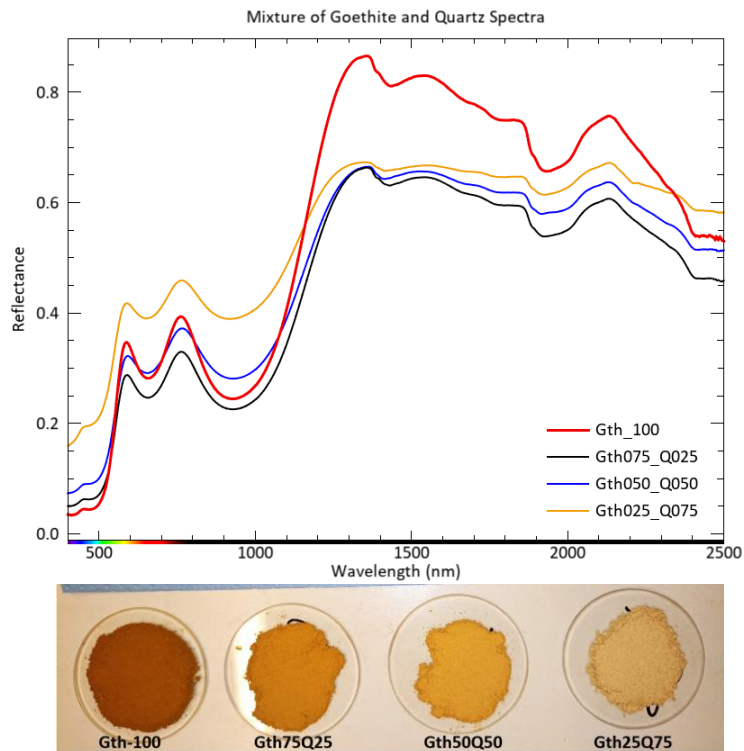
Appendix 5: Spectra of jarosite + quartz



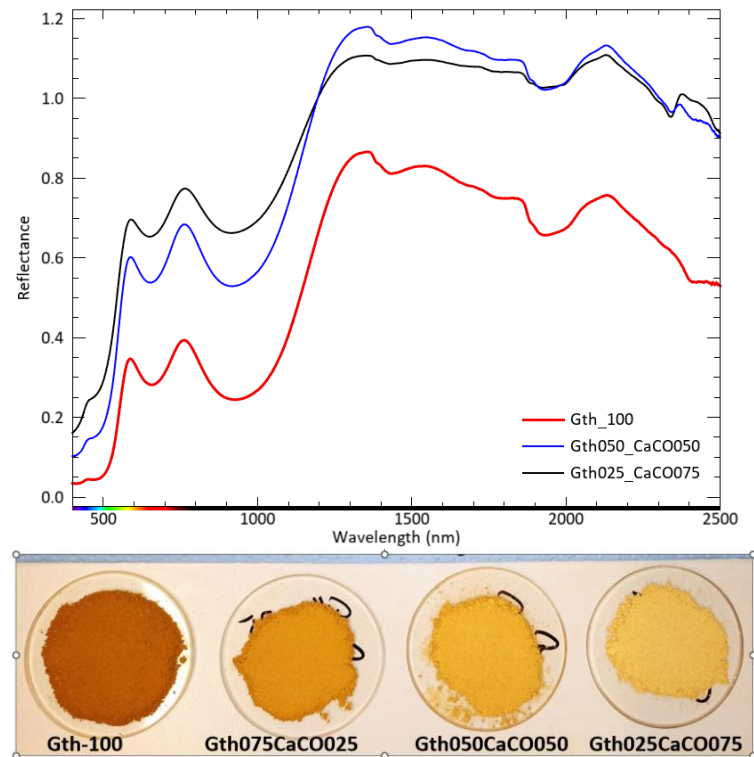
Appendix 6: Spectra of jarosite + calcite



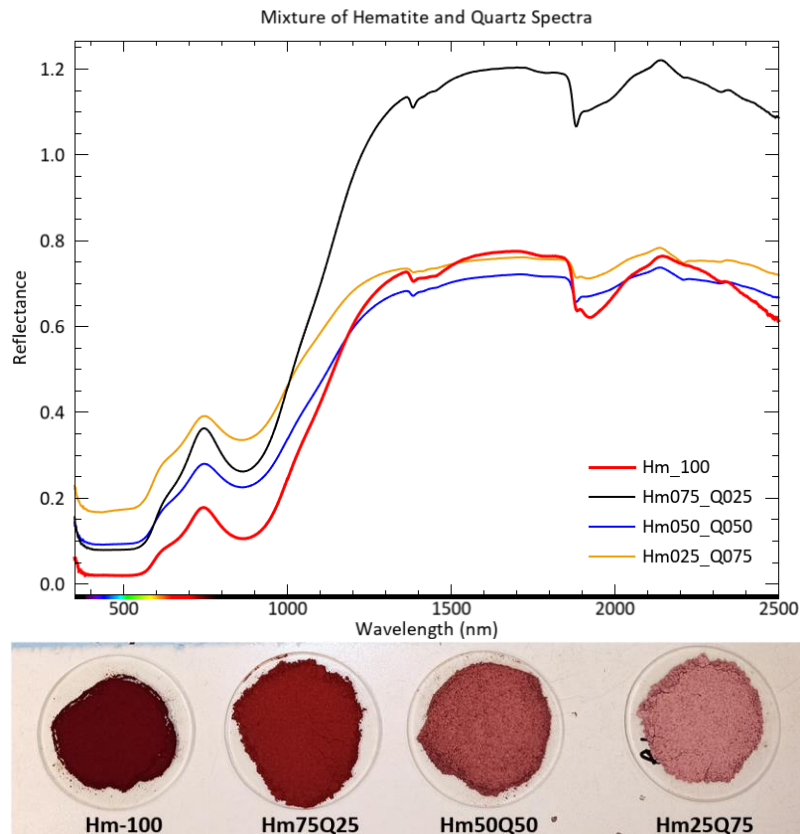
Appendix 7: Spectra of goethite + quartz



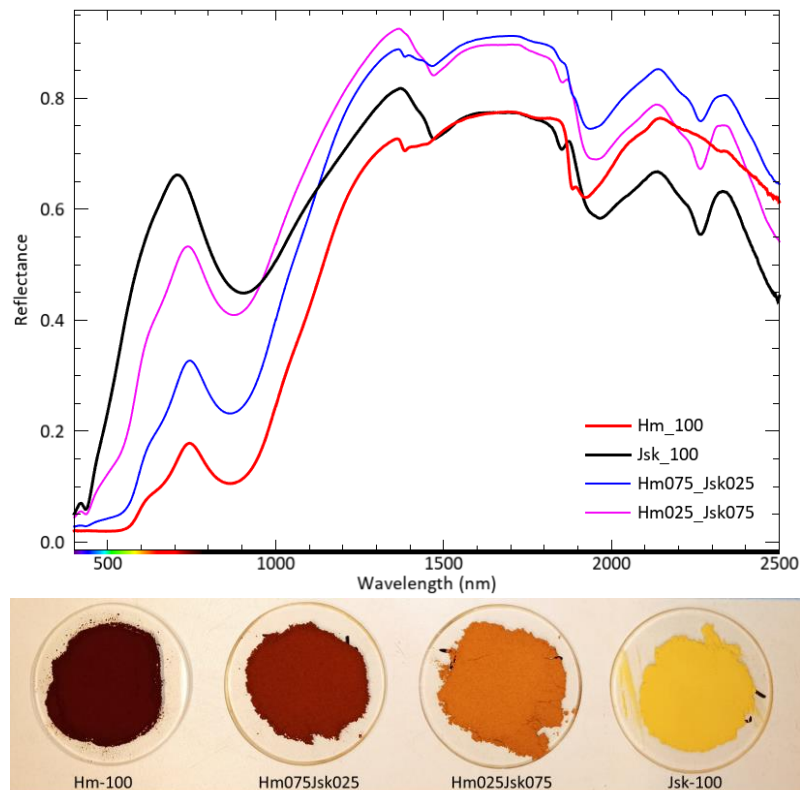
Appendix 8: Spectra of goethite + calcite



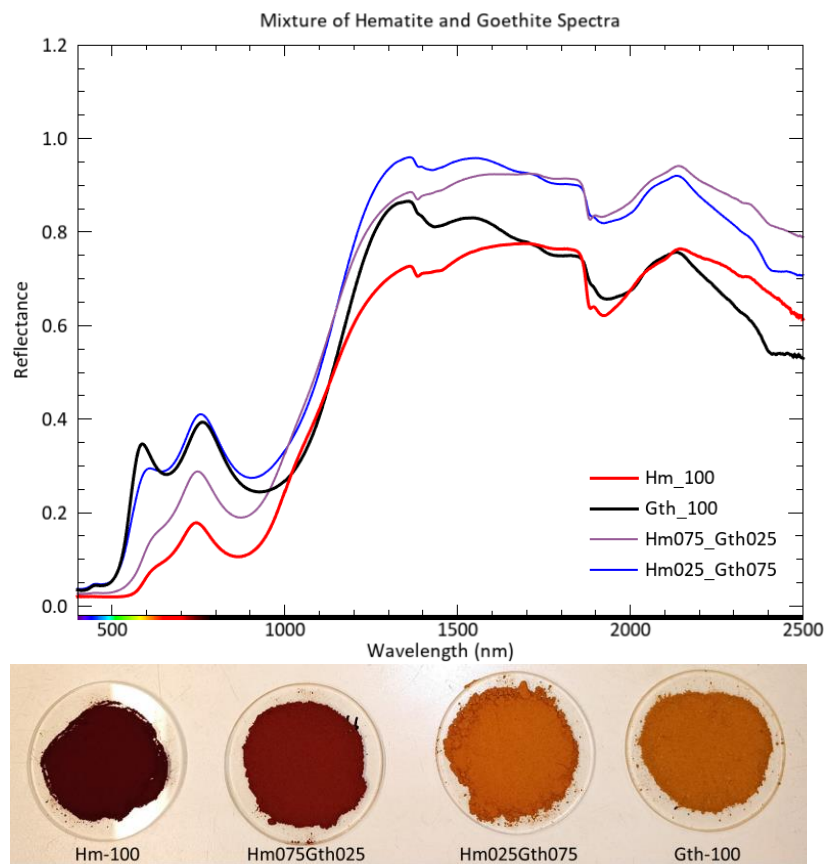
Appendix 9: Spectra of hematite + quartz



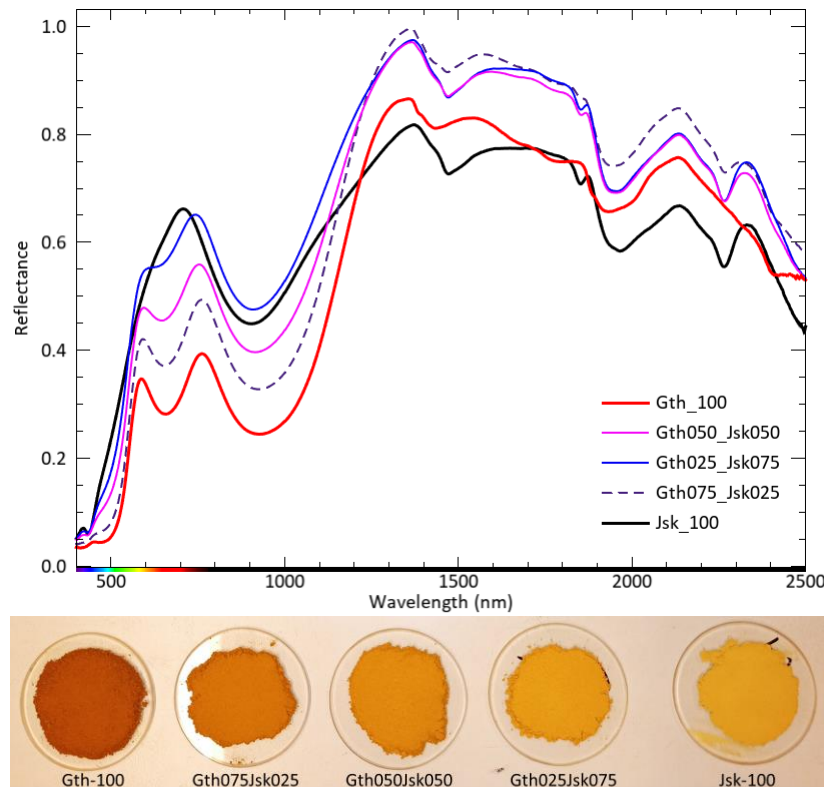
Appendix 10: Spectra of goethite + quartz



Appendix 11: Spectra of hematite + goethite

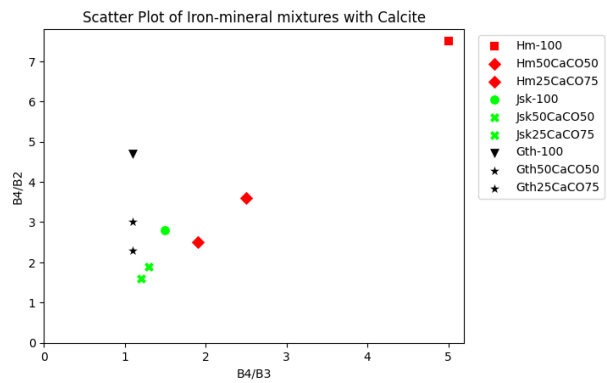
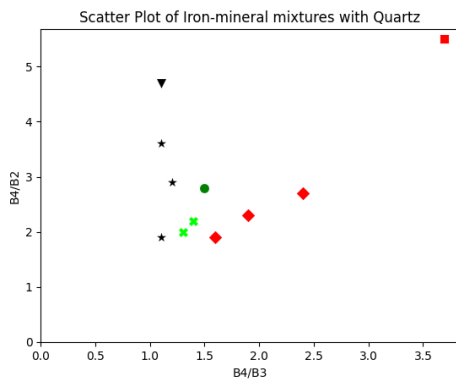
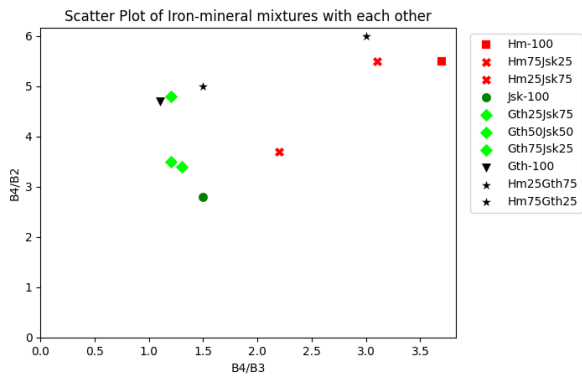


Appendix 12: Spectra of goethite + jarosite

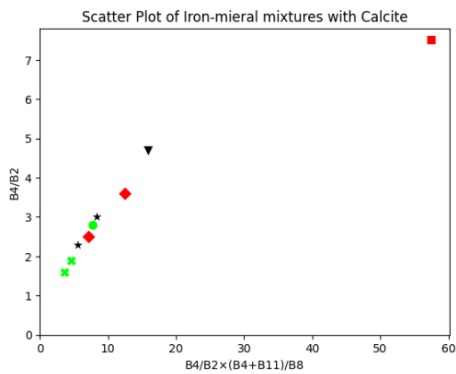
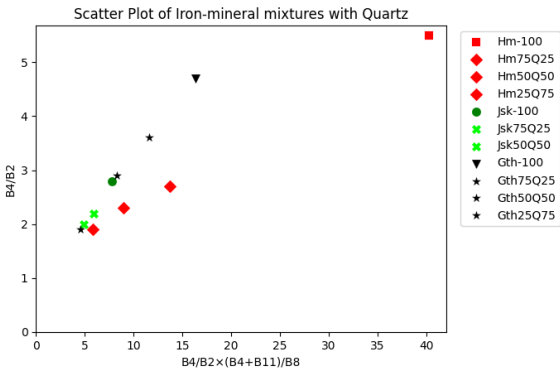
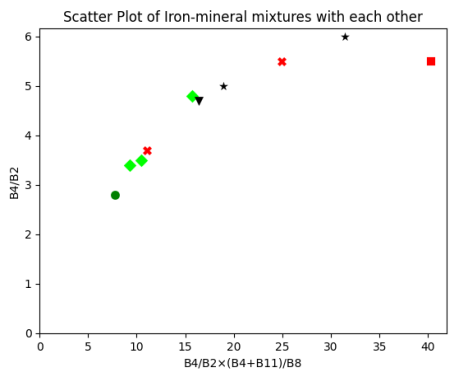


Discrimination of individual Iron-bearing minerals with the Sentinel-2 Super-Spectral Imager

Appendix 13: Scatter plots B4/B3 vs B4/B2

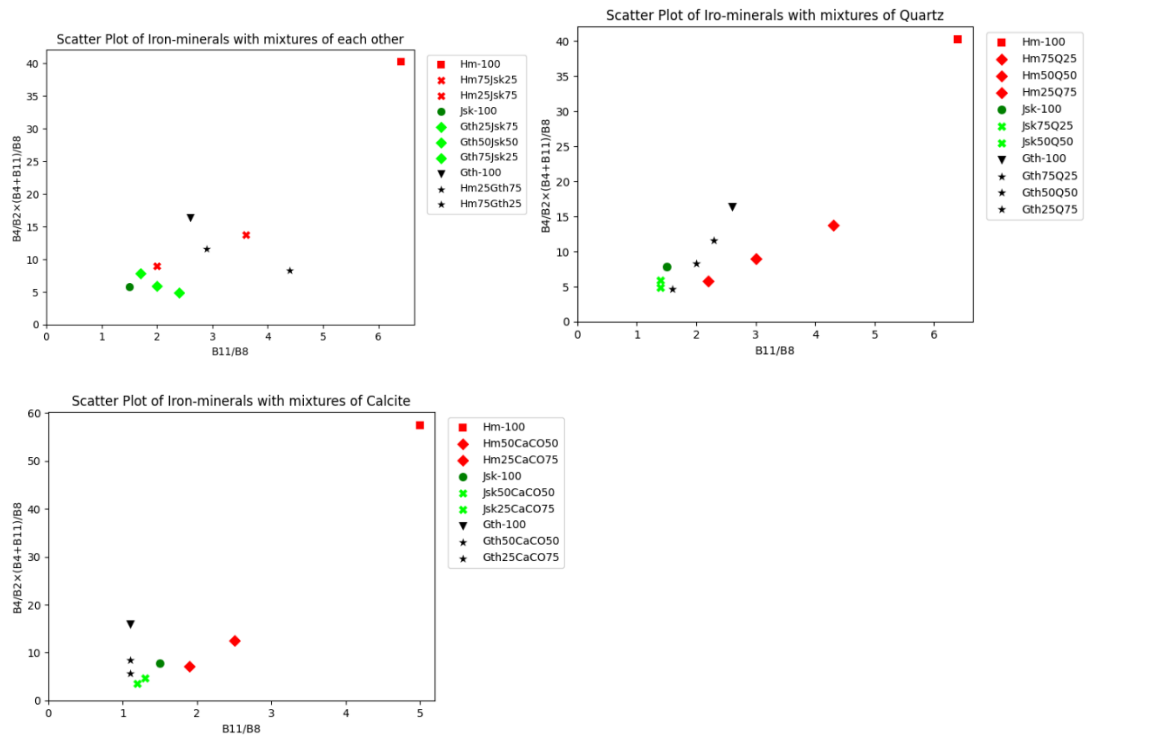


Appendix 14: Scatter plots $B4/B2 \times (B4+B11)/B8$ vs $B4/B2$

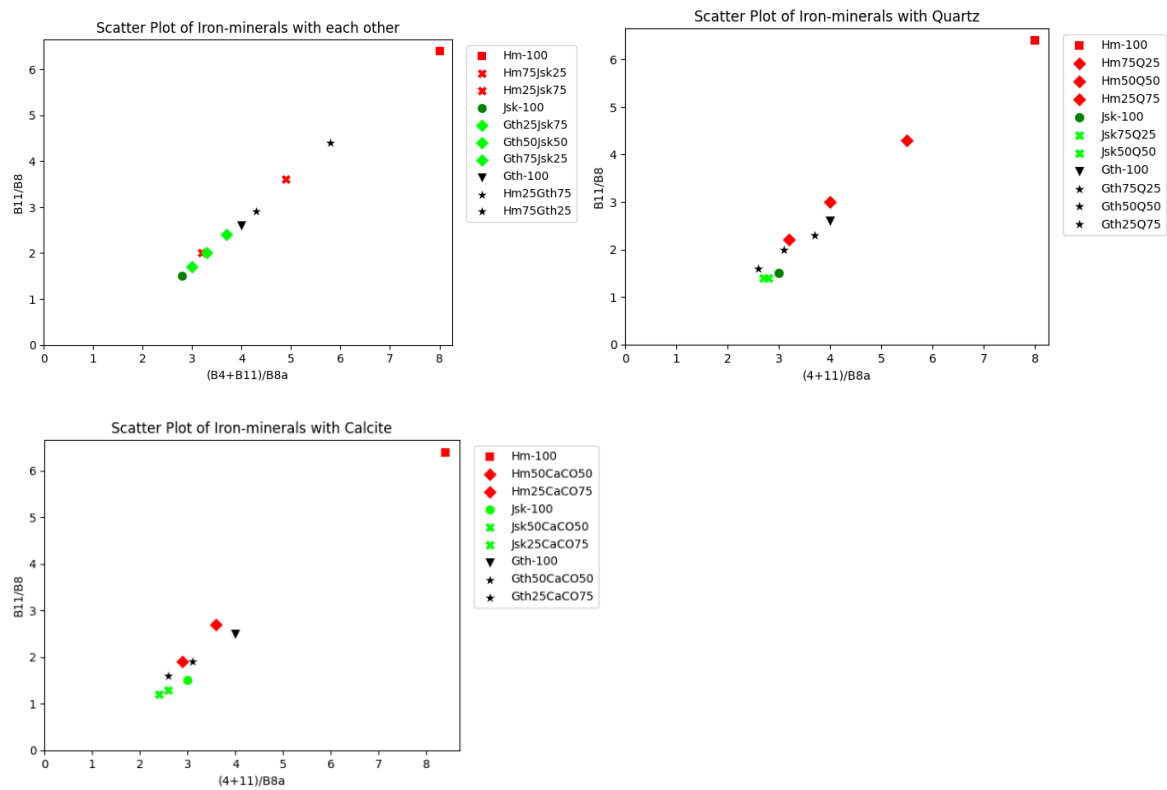


Discrimination of individual Iron-bearing minerals with the Sentinel-2 Super-Spectral Imager

Appendix 15: Scatter plots $B4/B2 \times (B4+B11)/B8$ vs $B11/B8$

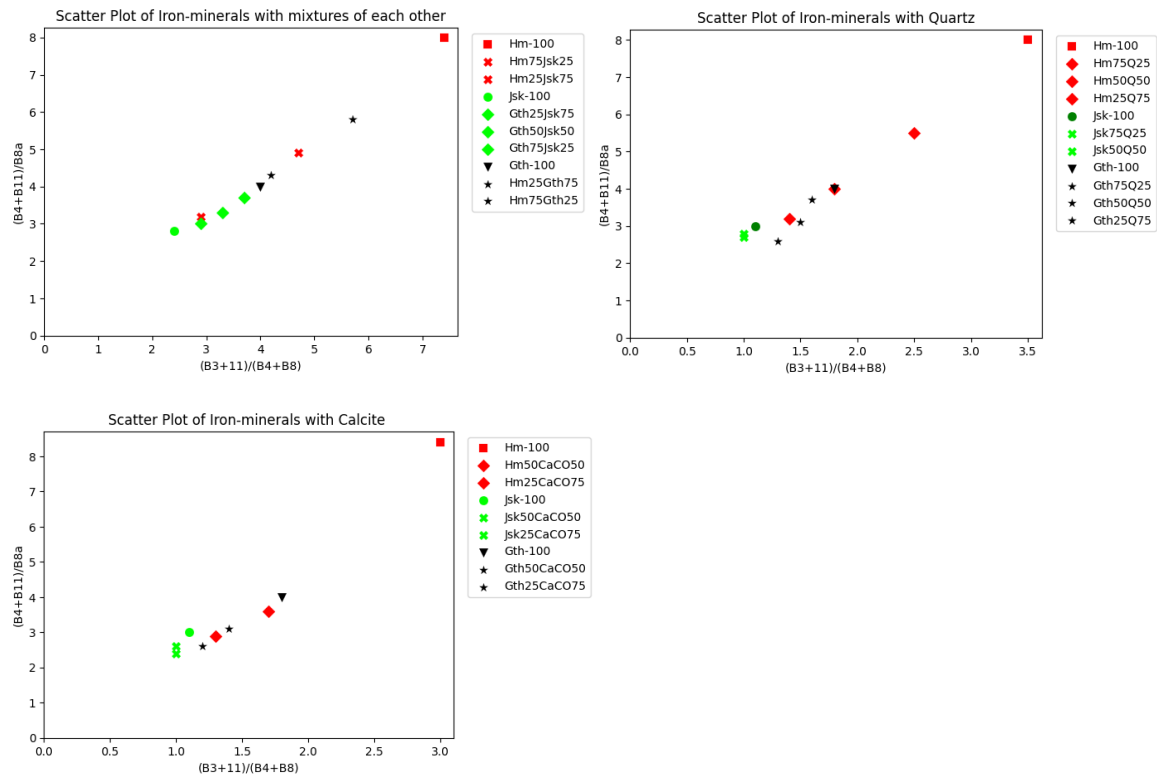


Appendix 16: Scatter plots $(B4+B11)/B8a$ vs $B11/B8$

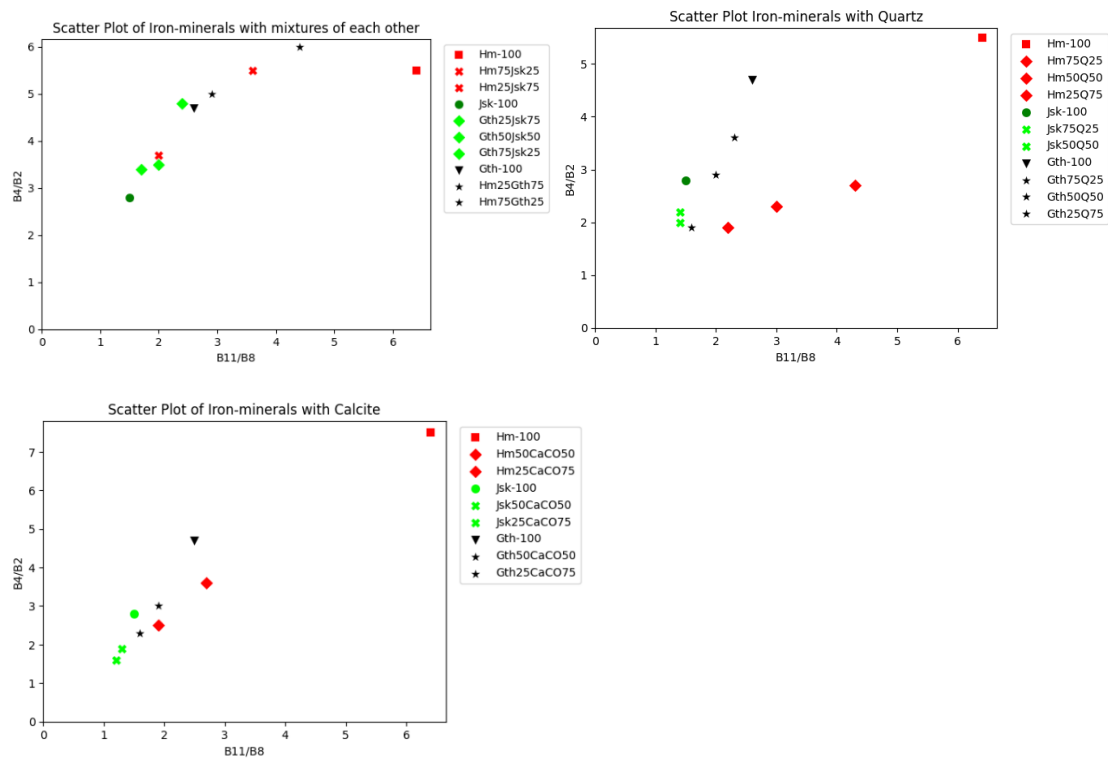


Discrimination of individual Iron-bearing minerals with the Sentinel-2 Super-Spectral Imager

Appendix 17: Scatter plots $(B3+11)/(B4+B8)$ vs $(B4+B11)/B8a$

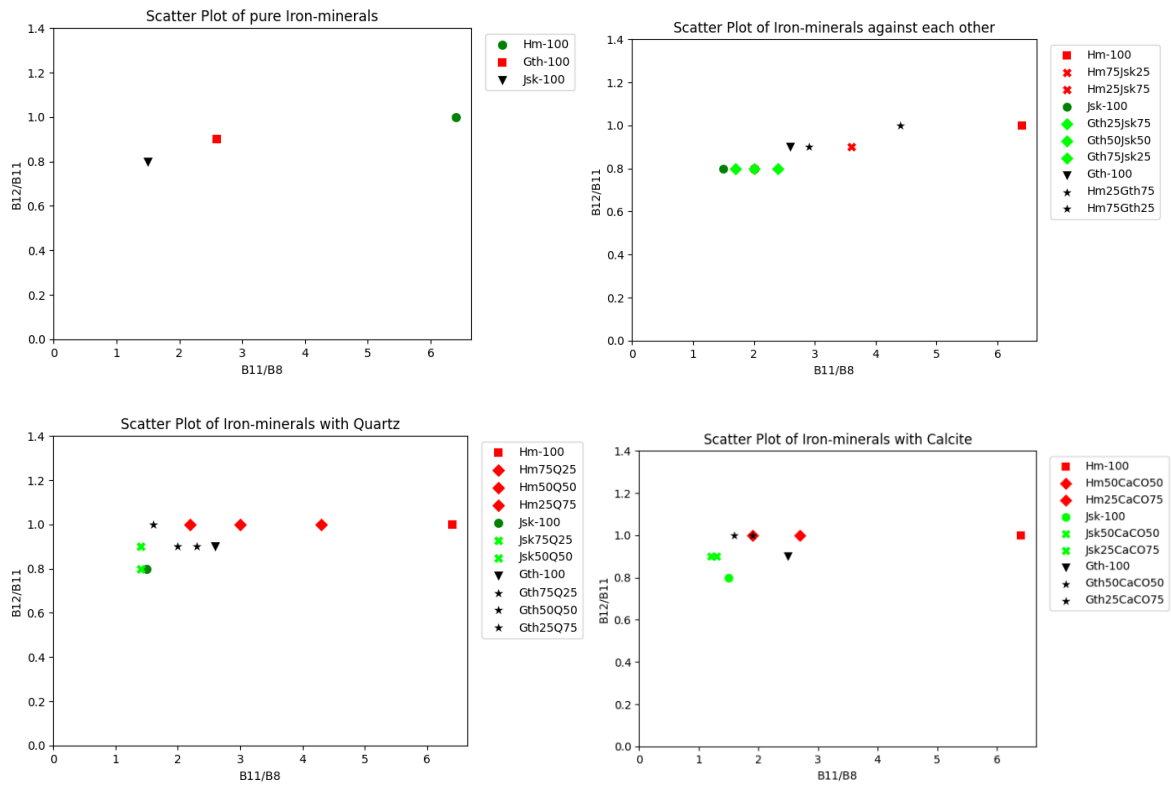


Appendix 18: Scatter plots $(B11/B8)$ vs $(B4/B2)$



Discrimination of individual Iron-bearing minerals with the Sentinel-2 Super-Spectral Imager

Appendix 19: Scatter plots (B11/B8) vs (B12/B11)



Appendix 20: Scatter plots (B12/B8)+(B3/B4) vs (B4+B11)/B8a

